

SEPARATION OF MIXED RADIOMETRIC LAND COVER TEMPERATURES
IN TIME-DELAYED BI-ANGULAR VIEWS USING ESTIMATED
FRACTIONAL DIFFERENTIAL COEFFICIENTS

BY

Scott Lawrence Williams, B.A., B.A., B.Sc., M.Sc.

A dissertation submitted to the Graduate School

in partial fulfillment of the requirements

for the degree of

Doctor of Philosophy

Major Subject: Plant and Environmental Sciences

Minor Subject: Electrical Engineering

New Mexico State University

Las Cruces, New Mexico

May 2014

Copyright © 2014 by Scott Lawrence Williams

UMI Number: 3582404

All rights reserved

INFORMATION TO ALL USERS

The quality of this reproduction is dependent upon the quality of the copy submitted.

In the unlikely event that the author did not send a complete manuscript and there are missing pages, these will be noted. Also, if material had to be removed, a note will indicate the deletion.

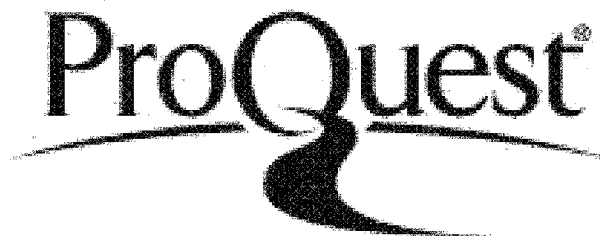


UMI 3582404

Published by ProQuest LLC 2015. Copyright in the Dissertation held by the Author.

Microform Edition © ProQuest LLC.

All rights reserved. This work is protected against unauthorized copying under Title 17, United States Code.



ProQuest LLC
789 East Eisenhower Parkway
P.O. Box 1346
Ann Arbor, MI 48106-1346

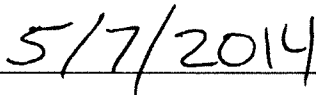
“Separation of Mixed Radiometric Land Cover Temperatures in Time-delayed Bi-angular Views using Estimated Fractional Differential Coefficients,” a dissertation prepared by Scott Lawrence Williams in partial fulfillment of the requirements for the degree, Doctor of Philosophy, has been approved and accepted by the following:



Loui Reyes
Interim Dean of the Graduate School



David DuBois
Chair of the Examining Committee



Date

Committee in charge:

Dr. David DuBois, Chair

Mr. Max Bleiweiss, M.Sc. (Physics)

Dr. Jay Jordan

Dr. Curtis Monger

DEDICATION

Dedications are a delicate process, for there is limited space to give recognition to so many deserving illumination. In general, I dedicate this work to those whom have taught me that the love of life and the pursuit of excellence, however imperfect in practice, transcends our earthly bounds and for this I am truly grateful.

Growing up, I was blessed with a loving, inquisitive, encouraging, and adventurous family and so I dedicate this work specifically to my family, past, present, and future. At the center of this scope are my parents, Pat and Lou, from whom radiated practically all of the influences of my life, and for this I am also grateful. In addition, this work is dedicated to my spouse and sweetheart Kathie, children Erin, Than, Matt, and Alex, godson JuanCar, grandchild Andriana, and to my brothers Daryl and Greg, and their families.

I would also like to extend a heart-felt thanks to all my friends, for their encouragement and good times.

ACKNOWLEDGEMENT

I would like to acknowledge my committee members for their help and effort. Special mention to Max Bleiweiss and Dean Lowell Catlett for their extraordinary support and encouragement in letting me set up the satellite ground station that served as my base throughout this process. Also, special mention to Vince Gutschick for his active participation and interest.

Most importantly, I would like to acknowledge the support I received from my sweetheart, Kathie Redmond, who was there for me in all ways, even though I was just a part-time spouse during this phase of our life.

VITA

Born: July 12, 1955, San Francisco, California, USA
Raised: Puerto Rico, Colombia, California, Venezuela, México
Education:

- 1975 B.A., Estudios Latinoamericanos (Antropología e Historia)
Universidad de las Américas, Cholula, Puebla, México
- 1978 B.A., Philosophy (Rationalism and Empiricism)
University of Guelph, Guelph, Ontario, Canada
- 1981 B.Sc., Agricultural Engineering (Power and Machinery)
New Mexico State University, Las Cruces, New Mexico, USA
- 1985 M.Sc., Mathematics (Numerical Analysis)
New Mexico State University, Las Cruces, New Mexico, USA

Professional Experience:

Instructor, Engineer, Analyst, or Contractor at:

New Mexico State University: Agricultural Engineering Department
Mathematics Department
Computing Research Laboratory
CARSAME Satellite Ground Station

Los Alamos National Laboratory: Theoretical Division

Cold Spring Harbor Laboratory: Computational Biology Laboratory

Cell Robotics, Inc.: Research and Development

Sandia National Laboratory: Materials Division

Visioneering Research Lab, Inc.: Founder, Semiconductor Inspection R&D

University of Arizona: Lunar and Planetary Lab, PIRL

Rice University: Electrical Engineering Department

PUBLICATIONS [or Papers Presented]

- Buican, T., Williams, S.L., et al. Ft-1000: A fluorescence spectra imaging microscope. *Presented at the International Society for Analytical Cytology, ISAC XVI, Colorado Springs, Colorado (1993).*
- Buican, T., Williams, S.L., et al. The optical trapping workstation: Complementary technologies. *Presented at the International Society for Analytical Cytology, ISAC XVI, Colorado Springs, Colorado (1993).*
- Lansford, R.R., Williams, S.L., et al. Irrigated Agricultural Decision Strategies for Variable Weather Conditions. *New Mexico Water Resources Research Institute (1983).*
- Marr, T.G, Williams, S.L., et al. Coping with Data from Large-Scale Mapping Efforts: Automating the Lab Notebook. *Presented at the Genome Mapping and Sequencing Meeting, Cold Spring Harbor Laboratory, Cold Spring Harbor, New York (1989).*
- Phillips, K., Williams, S.L., et al. Edge Analysis and Algorithms for Computer Vision. *Battelle Columbus Laboratories Technical Report Series (1984).*
- Sammis, T., Riley, W., and Williams, S.L.: Pecan Nut Yield and Tree Growth as Influenced by Irrigation. *New Mexico Water Resources Research Institute (1985).*
- Sammis, T., Williams, S.L., et al. Effects of Soil Moisture Stress on Leaf Area Index, Evaporation and Modeled Soil Evaporation and Transpiration. *American Society of Agricultural Engineers Journal 29(4), 956-961 (1986).*
- Sammis, T., Smeal, D., and Williams, S.L. Predicting Corn Yield Under Limited Irrigation using Plant Height. *American Society of Agricultural Engineers Journal 31(3), 830-838 (1987).*
- Sammis, T., Williams, S.L., and Jernigan, D. Development of a Drip Irrigation Scheduling Model. *New Mexico Water Resources Research Institute (1987).*
- Williams, S.L., and Freeburg, R.S. Solar Flux on Irregular Surfaces. *Presented at the Rocky Mountain Regional Meeting of the American Society of Agricultural Engineers, Fort Collins, Colorado (1982).*

- Williams, S.L., and Freeburg, R.S. Computer Representation of Radiation Loads on Plants. *Presented at the National Meeting of the American Society of Agricultural Engineers, Bozeman, Montana* (1983).
- Williams, S.L. Microcomputers in Agricultural Engineering. *Presented at the New Mexico State Meeting of the American Society of Agricultural Engineers, Albuquerque, New Mexico* (1983).
- Williams, S.L.: Fractals: An Introduction. *Presented at the Computing Research Laboratory Mathematics Seminar on Fractals, New Mexico State University, Las Cruces, New Mexico* (1987).
- Williams, S.L., Dunning, T.E., and Harris, J. Streamed Image Transformation Editor. *Memorandum in Computer and Cognitive Science MCCS-89-170, Computing Research Laboratory, New Mexico State University*, (1987).
- Williams, S.L. Streamed Image Transformation Editor. *Presented at the American Mathematics Society 100th Anniversary Meeting, New Mexico State University, Las Cruces, New Mexico* (1988).
- Williams, S.L., and Bertini, A. A Graphical Interface for Genomic Sequencing. *Memorandum in Computer and Cognitive Science MCCS-89-170, Computing Research Laboratory, New Mexico State University* (1989).
- Williams, S.L., et al. The Human Genome Information Resource. *Presented at the U.S. Department of Energy Human Genome Contractors Workshop, Santa Fe, New Mexico* (1989).
- Williams, S.L.: Imaging for the Human Genome Project. *Advanced Imaging* 5(7) (1990).
- Williams, S.L.: Image Analysis of Gel Patterns. *Presented at the Banbury Center Meeting on Electrophoresis of Large DNA Molecules: Theory, Practice and Future, Cold Spring Harbor Laboratory* (1990).
- Williams, S.L.: Probe Mark Analyzer. *Presented at the IEEE Southwest Test Conference, San Diego, California* (1995).

ABSTRACT

SEPARATION OF MIXED RADIOMETRIC LAND COVER TEMPERATURES

IN TIME-DELAYED BI-ANGULAR VIEWS USING ESTIMATED

FRACTIONAL DIFFERENTIAL COEFFICIENTS

BY

Scott Lawrence Williams, B.A., B.A., B.Sc., M.Sc.

Doctor of Philosophy

New Mexico State University

Las Cruces, New Mexico, 2014

Dr. David DuBois, Chair

A dissertation is presented concerning the separation of radiometric temperatures of sparse land covers from two views of mixed thermal and NDVI samples with a time delay between the views. The research scope is limited to a simple binary land cover of vegetation canopy and bare soil. Previous methods have been developed using simultaneous views but little work has been done on time-delayed sampling, which is the focus of this study.

The dissertation hypothesis is based on the observation that the rate of change of a mixed radiometric temperature with respect to actual fractional vegetation cover, $\frac{dT_m}{df_a}$, originally constructed using spatially varying vegetation covers, can also be constructed using bi-angular views of the same land parcel but with a different interpretation; that bi-angular samples provide a *perceived* fractional cover differential, $\frac{dT_m}{df_\theta}$. The hypothesis is that $\frac{dT_m}{df_\theta}$ can be used for sub-pixel temperature discrimination of binary land covers and, moreover, that the separate soil and vegetation total differential coefficients $\frac{dT_s}{df_\theta}$ and $\frac{dT_v}{df_\theta}$, required in the algebraic system, can be characterized to sufficiently capture environmental influences between samples in time. To test the hypothesis, this study heuristically derives a first-order estimation of the differential coefficients, required to decompose land cover temperatures from mixed data points, for any time-delayed sampling spanning the day. Applying the estimated values on similar target days gives a high success rate for a local time span of at least a week.

This approach, once scaled up, could be used by platforms with inherent time delays, such as tandem weather satellites, to provide separate land cover temperature estimates from low-resolution sensors.

Contents

LIST OF TABLES	xx
LIST OF FIGURES	xxiii
1 INTRODUCTION	1
1.1 Motivation.	1
1.2 Preamble.	2
1.3 Focus of study.	10
1.4 Background.	11
1.5 Outline of Study.	14
2 THEORY	16
2.1 Vegetation fractional cover.	16
2.2 Using NDVI as a fractional vegetation index.	19
2.3 Mixed thermal pixel.	21
2.4 Prior work using radiative transfer mixing.	24
2.5 Extending the radiative transfer system to include differential coefficients.	27
2.5.1 Reinterpreting the mixed temperature differential coefficient, $\frac{dT_m}{df_a}$ as $\frac{dT_m}{df_e}$	29
2.5.2 Factoring for view effects.	30
2.6 Parametrization of the temperature function and coefficients.	32

2.6.1	Environmental effects over time.	32
2.6.2	Identification of components.	34
2.7	Theory chapter summary.	35
2.7.1	Overview	35
2.7.2	A practical interpretation of $\frac{dT_o}{df_\theta}$	36
2.8	Hypothesis.	37
3	METHODS and RESULTS (Part I)	39
3.1	Data pre-processing.	39
3.2	Processing platforms used.	41
3.3	Algorithmic development.	43
3.3.1	Synthetic data.	44
3.3.2	Synthetic data and linearized radiative transfer.	45
3.3.3	Synthetic data and quartic radiative transfer.	49
3.3.4	Comparison of linearized and quartic radiative transfer models using synthetic data.	53
3.4	Methods and results for laboratory modeling.	54
3.4.1	Overhead implementation.	55
3.4.2	View angle implementation.	57
4	METHODS and RESULTS (Part II)	60
4.1	Field setup.	60
4.1.1	Variable parameter clamping.	61

4.1.2	Signal acquisition equipment.	63
4.1.3	Sampling issues.	64
4.1.4	Sampling times.	65
4.1.5	Sampling views.	67
4.2	Image segmentation of land covers.	68
4.3	Differential coefficients characterization.	70
4.3.1	Special case of view effects.	71
4.3.2	Generalizing by correlating differential coefficients to weather.	76
4.3.3	Principal component analysis.	90
4.4	Estimating perceived vegetation cover fraction.	94
4.4.1	Using averaged perceived fractional cover.	94
4.4.2	Using NDVI to estimate perceived fractional cover.	95
5	CONCLUSIONS and RECOMMENDATIONS for FUTURE STUD- IES.	98
5.1	Summary of approach.	98
5.2	Observations.	101
5.3	Conclusions.	103
5.4	Potential improvements and recommendations.	104
	REFERENCES	107
A	Variable Lists.	111
B	Acronym List.	114

C	Differential Calculations.	115
C.1	Linear radiative transfer differentiation.	115
C.2	Quartic radiative transfer differentiation.	116
D	Energy balance equations.	118
E	Geometric effects.	121
E.1	Camera angle and view area.	121
E.2	Generated data.	125
F	Tabulated results for 12cm bed.	127
F.1	Near instantaneous sampling results and metrics used.	127
F.2	Combined and averaged surface fits with known cover fractions.	130
F.3	Individual day surface fits with known land cover fractions.	134
F.4	Results using averaged land cover fractions.	135
F.5	Results using NDVI land cover fractions.	137
F.6	NDVI and thermal registered images.	139
G	Tabulated results for 24 cm bed.	140
G.1	Near instantaneous sampling results and metrics used.	140
G.2	Combined and averaged surface fits with known cover fractions.	143
G.3	Individual day surface fits with known land cover fractions.	147
G.4	Results using averaged land cover fractions.	148
H	Environmental correlation graphs of $\frac{dT_o}{df_\theta}$ for 12cm bed.	151
I	Environmental correlation graphs of $\frac{dT_o}{df_\theta}$ for 24cm bed.	156

J	Correlation graphs for relative humidity and air temperature differences.	162
K	Bi-variate correlation graphs of $\frac{dT_a}{dT_e}$ for 12cm bed.	164
L	Principal component analysis graphs for 12cm bed.	166
M	Principal component analysis graphs for 24cm bed.	171
N	Differential coefficients observed over time periods.	177

List of Tables

1	Residual results, δT , of using Systems (20) and (23) and quartic radiative mixing on the data depicted in Figure 5(b).	54
2	Residual results, δT , for the quartic radiative transfer System (23) using data depicted in Figure 7(a).	56
3	Residual results, δT , for the quartic System (23) using data depicted in Figure 7(b).	57
4	Residual results, δT , for the quartic Systems (23) using data depicted in Figure 8(a) and (b).	59
5	Near-instantaneous results using averaged $\frac{dT_s}{df_\theta}$ and $\frac{dT_v}{df_\theta}$	74
6	Near-instantaneous results using $\frac{dT_s}{df_\theta} = 0$ and $\frac{dT_v}{df_\theta} = 0$	74
7	Differential coefficient correlation R^2 values as environmental variables are progressively included.	80
8	Unmixing results using estimated differential coefficients, $\frac{dT_s}{df_\theta}$ and $\frac{dT_v}{df_\theta}$, from daily weather fit for 12cm bed.	82
9	Unmixing results using estimated differential coefficients, $\frac{dT_s}{df_\theta}$ and $\frac{dT_v}{df_\theta}$, from daily weather fit for 24cm bed.	82
10	Unmixing results using estimated differential coefficients, $\frac{dT_s}{df_\theta}$ and $\frac{dT_v}{df_\theta}$, from combined and averaged surface fits of all days for 12cm bed.	84

11	Unmixing results using estimated differential coefficients from combined and averaged surface fits of all days for 24cm bed.	84
12	Surface intercept, C_0 , and view effect, $\frac{\partial T_0}{\partial f_\theta}$, comparison.	88
13	Averaged environmental partial differentials for 12cm vegetation cover.	89
14	Greek Variable List	111
15	Modern Variable List	112
16	Modern Variable List (con't)	113
17	Acronym List	114
18	Vegetation cover results for “instantaneous” samples with averaged $\frac{dT_v}{df_\theta}$ and $\frac{dT_s}{df_\theta}$ for 12cm bed.	128
19	Soil cover results for near instantaneous samples with averaged $\frac{dT_v}{df_\theta}$ and $\frac{dT_s}{df_\theta}$ for 12cm bed.	129
20	Unmixing results using estimated differential coefficients, $\frac{dT_v}{df_\theta}$ and $\frac{dT_s}{df_\theta}$, derived from combined and averaged surface fits for dates 12/08/08 and 12/08/09 as predictor for 12cm bed. Known cover fractions were used.	130
21	Unmixing results using estimated differential coefficients, $\frac{dT_v}{df_\theta}$ and $\frac{dT_s}{df_\theta}$, derived from combined and averaged surface fits for dates 12/08/08 and 12/08/10 as predictor for 12cm bed. Known cover fractions were used.	131

22	Unmixing results using estimated differential coefficients, $\frac{dT_v}{df_\theta}$ and $\frac{dT_s}{df_\theta}$, derived from combined and averaged surface fits for dates 12/08/08 and 12/08/16 as predictor for 12cm bed. Known cover fractions were used.	131
23	Unmixing results using estimated differential coefficients, $\frac{dT_v}{df_\theta}$ and $\frac{dT_s}{df_\theta}$, derived from combined and averaged surface fits for dates 12/08/09 and 12/08/10 as predictor for 12cm bed. Known cover fractions were used.	132
24	Unmixing results using estimated differential coefficients, $\frac{dT_v}{df_\theta}$ and $\frac{dT_s}{df_\theta}$, derived from combined and averaged surface fits for dates 12/08/09 and 12/08/16 as predictor for 12cm bed. Known cover fractions were used.	132
25	Unmixing results using estimated differential coefficients using combined and averaged dates 12/08/10 and 12/08/16 with known cover fractions as predictor for 12cm.	133
26	Unmixing results using estimated differential coefficients, $\frac{dT_v}{df_\theta}$ and $\frac{dT_s}{df_\theta}$, derived from individual day surface fits as predictors on other dates for 12cm bed. Used with known cover fractions.	134
27	Unmixing results using estimated differential coefficients, $\frac{dT_v}{df_\theta}$ and $\frac{dT_s}{df_\theta}$, from individual day surface fits on the remainder days with averaged fractions.	135

28	Unmixing results using estimated differential coefficients, $\frac{dT_v}{df_\theta}$ and $\frac{dT_s}{df_\theta}$, from two combined day surface fits as predictors, on the remainder day with averaged fractions.	136
29	Unmixing results using estimated differential coefficients, $\frac{dT_v}{df_\theta}$ and $\frac{dT_s}{df_\theta}$, from individual day surface fits on the remainder days with NDVI fractions.	138
30	Unmixing results using estimated differential coefficients, $\frac{dT_v}{df_\theta}$ and $\frac{dT_s}{df_\theta}$, from two combined day surface fits as predictors, on the remainder day with NDVI fractions.	138
31	Vegetation cover results for near instantaneous samples with averaged $\frac{dT_v}{df_\theta}$ and $\frac{dT_s}{df_\theta}$ for the 24cm bed.	141
32	Soil cover results for near instantaneous samples with averaged $\frac{dT_v}{df_\theta}$ and $\frac{dT_s}{df_\theta}$ for the 24cm bed.	142
33	Unmixing results using estimated differential coefficients, $\frac{dT_v}{df_\theta}$ and $\frac{dT_s}{df_\theta}$, derived from combined and averaged surface fits for dates 12/08/11 and 12/08/12 as predictor. Known cover fractions were used.	143
34	Unmixing results using estimated differential coefficients, $\frac{dT_v}{df_\theta}$ and $\frac{dT_s}{df_\theta}$, derived from combined and averaged surface fits for dates 12/08/12 and 12/08/13 as predictor. Known cover fractions were used.	144

35	Unmixing results using estimated differential coefficients, $\frac{dT_v}{df_\theta}$ and $\frac{dT_s}{df_\theta}$, derived from combined and averaged surface fits for dates 12/08/13 and 12/08/14 as predictor. Known cover fractions were used.	144
36	Unmixing results using estimated differential coefficients, $\frac{dT_v}{df_\theta}$ and $\frac{dT_s}{df_\theta}$, from combined and averaged surface fits for dates 12/08/14 and 12/08/15 as predictor. Known cover fractions were used. . . .	145
37	Unmixing results using estimated differential coefficients, $\frac{dT_v}{df_\theta}$ and $\frac{dT_s}{df_\theta}$, from an averaged fit of three other days as predictor on the remainder days. Used with known cover fractions.	146
38	Unmixing results using estimated differential coefficients, $\frac{dT_v}{df_\theta}$ and $\frac{dT_s}{df_\theta}$, from an averaged fit of four other days as predictor. Used with known cover fractions.	146
39	Unmixing results using estimated differential coefficients, $\frac{dT_v}{df_\theta}$ and $\frac{dT_s}{df_\theta}$, from individual day surface fits as predictors on other dates. Used with known cover fractions.	147
40	Unmixing results using estimated differential coefficients, $\frac{dT_v}{df_\theta}$ and $\frac{dT_s}{df_\theta}$, from individual day surface fits as predictors on other dates. Used with averaged cover fractions.	149

41	Unmixing results using estimated differential coefficients, $\frac{dT_v}{df_\theta}$ and $\frac{dT_s}{df_\theta}$, from an averaged fit of three other days as predictor on the remainder days. Used with averaged cover fractions.	150
42	Unmixing results using estimated differential coefficients, $\frac{dT_v}{df_\theta}$ and $\frac{dT_s}{df_\theta}$, from an averaged fit of four other days as predictor. Used with averaged cover fractions.	150
43	Calculated differential coefficients from sensed covers over time.	177

List of Figures

1	Typical graphs for sampled fractional vegetation cover as a function of view angle, $f_\theta = G(\theta)$, for marigold field plots.	17
2	Thermal images of marigolds and corresponding mixed pixel.	24
3	Theoretical position of lines in (T_m, f_a) space: 1, absolute dry line; 2, actual dry line; 3, actual wet line; 4, absolute wet line; 5, vegetation fraction isoline; 6, scatter plot envelope of mixed pixel temperatures in (T_m, f_a) space; 7, isolines of $\frac{dT_m}{df_a}$ with constant water availability. From Zhang, et al., [35, 37].	28
4	POLI image processing of thermal nadir and oblique views.	43
5	Synthetic images used for emulating fractional cover changes for different samples. The smaller rectangles represent vegetative cover. The resulting “mixed” temperature varies with fractional cover.	44
6	Temperature residuals using System (19) with data depicted in Figure 5(b).	48
7	Thermal infrared images emulating view cover changes by increasing canopy over dry sand for a series of samples.	56
8	Two sets of thermal infrared images at different view angles, using <i>Viola Wittrockiana</i>	58
9	Marigold beds and acquisition station.	61

10	Sunlit and shaded and cover temperature samples.	65
11	Power decibel representation of closeness to sensed soil temperature.	75
12	Scatter plot of various soil moistures and NDVI.	137
13	Four images make one sample. Green buffer represents near-infrared band.	139
14	Environmental correlation graphs for 12/08/08 and 12cm bed. . .	151
15	Environmental correlation graphs for 12/08/09 and 12cm bed. . .	152
16	Environmental correlation graphs for 12/08/10 and 12cm bed. . .	153
17	Environmental correlation graphs for 12/08/16 and 12cm bed. . .	154
18	Environmental correlation graphs for all sample days and 12cm bed.	155
19	Environmental correlation graphs for 12/08/11 and 24cm bed. . .	156
20	Environmental correlation graphs for 12/08/12 and 24cm bed. . .	157
21	Environmental correlation graphs for 12/08/13 and 24cm bed. . .	158
22	Environmental correlation graphs for 12/08/14 and 24cm bed. . .	159
23	Environmental correlation graphs for 12/08/15 and 24cm bed. . .	160
24	Environmental correlation graphs for all sample days and 24cm bed.	161
25	Relative humidity difference and air temperature difference corre- lation graphs for dates used 12cm bed.	162
26	Relative humidity difference and air temperature difference corre- lation graphs for dates used for 24cm bed.	163
27	Delayed sampling correlations of $\frac{dT_s}{df_\theta}$	164

28	Delayed sampling correlations of $\frac{dT_v}{df_\theta}$	165
29	$\frac{dT_v}{df_\theta}, \frac{dT_s}{df_\theta}$ principal component graphs for 12/08/08 and 12cm bed. .	166
30	$\frac{dT_v}{df_\theta}, \frac{dT_s}{df_\theta}$ principal component graphs for 12/08/09 and 12cm bed. .	167
31	$\frac{dT_v}{df_\theta}, \frac{dT_s}{df_\theta}$ principal component graphs for 12/08/10 and 12cm bed. .	168
32	$\frac{dT_v}{df_\theta}, \frac{dT_s}{df_\theta}$ principal component graphs for 12/08/16 and 12cm bed. .	169
33	$\frac{dT_v}{df_\theta}, \frac{dT_s}{df_\theta}$ principal component graphs for all and 12 cm bed.	170
34	$\frac{dT_v}{df_\theta}, \frac{dT_s}{df_\theta}$ principal component graphs for 12/08/11 and 24cm bed. .	171
35	$\frac{dT_v}{df_\theta}, \frac{dT_s}{df_\theta}$ principal component graphs for 12/08/12 and 24cm bed. .	172
36	$\frac{dT_v}{df_\theta}, \frac{dT_s}{df_\theta}$ principal component graphs for 12/08/13 and 24cm bed. .	173
37	$\frac{dT_v}{df_\theta}, \frac{dT_s}{df_\theta}$ principal component graphs for 12/08/14 and 24cm bed. .	174
38	$\frac{dT_v}{df_\theta}, \frac{dT_s}{df_\theta}$ principal component graphs for 12/08/15 and 24cm bed. .	175
39	$\frac{dT_v}{df_\theta}, \frac{dT_s}{df_\theta}$ principal component graphs for all and 24cm bed.	176

1 INTRODUCTION

1.1 Motivation.

The broader goal of this dissertation is to contribute, in some incremental way, to the scientific modeling of water evaporation from the surfaces of soil and vegetation, specifically over large sparse areas. Evaporation is a key component in the hydrological process and is of keen interest to agronomists, climatologists, and other earth scientists. For the agronomist, water usage in crops is tied to evaporation and so knowing evaporation rates directly translates to managing irrigation more efficiently. For climatologists and meteorologists, evaporation rates influence regional effects (such as drought, cloud formations, humidity, dust storms, etc.) and so better quantification of evaporation over large areas improves climate and weather modeling. Because of modern concerns regarding water availability and management, the need for accurate values of evaporation over large areas is becoming more prominent in these, and other hydrological, studies and therefore serves as the motivation for this study.

Increasing the accuracy of evaporation estimates can be accomplished through better land cover temperature determinations. However, low-resolution sensors used on modern satellites mix the land cover temperatures, which, if discriminated, could be applied separately to the surface energy balance models for better results in estimating water usage. Separating the land cover temperatures using

low-resolution, time-delayed, data is the focus of this study.

1.2 Preamble.

From the start of agricultural practices, and probably before, humans have had a rudimentary understanding of the relationships between soil, water, sun, and plants through simple observation: plants need the right amount of heat, light and water to grow in fertile soil. Thousands of years of experience led to tried and true agricultural practices but, with little understanding of these relationships until the twentieth century when scientists, armed with functional theories and sensors, started to peer into the associated, and very complicated, physical and chemical processes involved.

Nevertheless, some great thinkers in ancient times did attempt to explain these relationships though lacking the scientific tools of modern times. In his seminal treatise, *Meteorology*, the Greek philosopher Aristotle [2] weighs in on the subject of evaporation:

The sun both checks the formation of winds and stimulates it. When the evaporation is small in amount and faint the sun wastes it and dissipates by its greater heat the *lesser heat contained in the evaporation*. It also dries up the earth, the source of the evaporation, before the latter has appeared in bulk: just as, when you throw a little fuel into a great fire, it is often burnt up before giving off any smoke. In these ways the sun checks winds and prevents them from rising at all: it checks them by wasting the evaporation, and prevents their rising by drying up the earth quickly...

Aristotle, *Meteorology* Book II, Scroll 5, 350 BCE

Aristotle is saying that water vapor contains a “lesser heat” and in this

context he probably means a lesser sensible¹ heat than to that felt from the sun. However, the ancients knew that it takes heat to melt ice, to boil water and that a wet cloth will cool the body as the cloth dries, so some association between heat and water state, or phase, was evident to them. It is tantalizing to consider that Aristotle might have been referring to a different form of heat captured in the vapor, a heat necessary to change liquid water to water vapor but that is not expressed as sensible.

The partitioning of heat into sensible and non-sensible components during the water phase transition of evaporation was not evident until the late eighteenth century when the Scottish physician, Joseph Black, noticed that adding more heat to boiling water did not raise the water temperature, but instead produced more steam. He theorized that the applied extra heat was “contained” in the transition and called it “latent” or hidden heat [29]. This realization laid the foundation for thermodynamic theory and later, his student, James Watt, used it to launch the industrial revolution with the steam engine.

By the early twentieth century, science had advanced sufficiently in the fields of fluid mechanics, chemistry and physics to address surface evaporation as one component, of many, in energy and mass exchanges, or transfers. Light and radiative heat were now unified as radiative energy phenomena. Potential diffusive equations became widely used to describe energy fluxes² and were analogous to

¹Capable of being perceived by the senses or sensors.

²Flux is defined as the flow rate of *something* (eg. charge, energy, particles, water) through

each other, so that gravity, heat, electricity, magnetism, and even water flow in liquid or vapor form could be described with similar equations.

The ability to abstractly reduce environmental influences to a currency of energy allowed the formulation of a simplified energy flux balance equation for a surface, such as soil or vegetation, where the energy fluxes to and from a surface add up to zero. This is expressed in terms of energy fluxes (with positive values going into the surface and negative values going out) as,

$$R_n + G + H + LE = 0 \quad (1)$$

with a description given below. Joseph Black's realization that energy directly translates to evaporation, and by extension to water usage, allows for the estimation of water usage in terms of energy.

Rearranging the balance equation as $R_n = -G - H - LE$ shows that the driver energy flux, R_n (net radiation) is distributed among G (ground heat conduction flux), H (atmospheric sensible heat transfer flux), LE (atmospheric latent heat transfer flux)³. The surface is considered infinitesimally thin, so ground heat storage is implicit in the calculation of ground conductive flux, G . If a plant surface is being considered then G is negligible. The difference between R_n and G is considered to be the available energy and the terms H and LE are called

a unit surface area.

³See Appendix D for calculations used in surface flux models.

turbulent fluxes. It is the latent heat flux, LE , that evaporates water. If water is not available then there is no evaporation ($LE = 0$) and H gets all the available energy. The latent heat flux captured in water evaporation is now modeled as part of a bigger partitioning of available energy fluxes and can be used to estimate the amount of water evaporated from either soil or vegetation surfaces.

Several methods for estimating latent heat, LE , use the above balance equation as their foundation. In 1948, Howard Penman derived an explicit equation which combined the energy balance and aerodynamic values of air temperature, wind speed, and relative humidity to calculate the evaporation from an open pan [28]. He then indexed, using a fractional coefficient, the evaporation of wet, bare soil and grass to the open pan evaporation. In 1965, John Montieth extended the Penman equation to include aerodynamic resistances to heat and vapor fluxes on a more general level [23]. Later work showed that many crops and their stages of growth could also be indexed to a reference crop with a full canopy and available water [1].

While the Penman-Montieth formulation can be applied to either soil or vegetation surfaces separately, the practice of indexing to a full canopy crop through various stages of crop growth roughly mixes both soil and vegetation surface evaporations as one⁴ and does not discriminate between the land covers which have different shortwave albedo, thermal emissivities, aerodynamic resis-

⁴Also known as “evapotranspiration”, a portmanteau combining soil evaporation and plant transpiration.

tances, and surface temperatures. Nevertheless, the Penman-Montieth approach has been successful and is probably the most widely used method to calculate evaporations worldwide⁵. In addition, sensors used in the field (flux towers) to verify calculations can only give mixed evaporation results so this is a compatible approach.

Another approach is to consider latent heat flux, LE , as a residual from the energy flux balance equation, so that $LE = -R_n - G - H$. Given that values for R_n and G can be obtained accurately, the result relies on calculating the sensible heat value, H , expressed aerodynamically for soils and vegetation as

$$H = \rho C_p \frac{(T_{ao} - T_a)}{r_a} \quad (2)$$

where H is the heat flux, ρC_p is the volumetric heat capacity of the air, T_a is the air temperature at some reference height, r_a is the surface-to-atmospheric resistance to heat transport, and is a complicated function of wind friction velocity, displacement height, roughness coefficients based on shape, and other factors⁶. Interestingly, the aerodynamic surface temperature, T_{ao} , is not measurable, but instead must be calculated by measuring H using sophisticated flux sensors. In the current literature, it is speculated that aerodynamic and radiometric values are the same however, many papers have been written on the divergence of the two [5].

⁵In 1990, the United Nation's Food and Agricultural Organization recommended the Penman-Montieth combination method as standard for reference evapotranspiration[1].

⁶See Appendix (D) for more details.

The residual approach became popular with environmental scientists when artificial satellites, equipped with spectral sensors, began reporting land surface temperatures (LST). Surface energy flux models began using the LST values as surrogates for the aerodynamic T_{ao} , which gives H if the other parameters are known, and therefore latent heat, LE , by using the balance equation.

LST values from low-resolution⁷ satellite sensors give a “mixed” soil and vegetation radiometric temperature value. Using this value as a surrogate for T_{ao} is a reasonable approach for dense vegetation cover, where canopy and soil temperatures do not differ greatly [7]. Moreover, for dense covers, the radiometric temperature remains fairly constant when viewed from different angles⁸. Due to the homogeneous presentation of dense cover to a satellite thermal sensor, views do not have to be at nadir to get reliable data for surface flux models [12, 20, 27]. This increases overall pixel usage in the sensor and, by extension, increases temporal sampling frequency of a terrestrial site⁹.

In contrast to a dense vegetation cover, a sparse cover behaves differently due to the large differences in temperature between bare soil and vegetation and to the gaps in the canopy. When sampling the co-centered areas at different view

⁷Current satellite sensor platforms have a thermal pixel resolution of $\sim 1.1km^2$ at nadir (looking down perpendicularly). This is a function of sensor resolution, optical distortions, and field of view.

⁸Studies indicate that canopies with varying emissivities depending on view can be characterized and adjusted for [20, 7, 31].

⁹Satellite sampling frequencies are a function of orbital periods and the optical field of view (FOV). For polar orbiting satellites, the wider the FOV the more frequent a land site will be sampled, but at different view angles. Increasing the number of acceptable sensor pixels (a subset of the optical FOV) therefore increases the sample frequency.

angles, large radiometric temperature differences are evident due to the perceived vegetation fraction presentation of land covers [14, 20]. To illustrate this, consider viewing a parcel of land (with sparse vegetation) from an oblique angle and then looking at the same parcel from a nadir angle. The oblique view angle has more vegetation contribution than does the nadir view. Since the thermal vegetation contribution is typically cooler, due to wind exposure and transpiration¹⁰, an oblique radiometric reading of one pixel (a pixel that averages, or mixes, the field of view¹¹) will be cooler than an overhead one. For example, a thermal sensor can give a mixed pixel's LST value in a sparse cover a value of $54^{\circ}C$ from one view angle (overhead angle) and $46^{\circ}C$ from another view angle (oblique angle); but within that pixel the soil cover has an average temperature of $63^{\circ}C$ while the average vegetation cover temperature is at $37^{\circ}C$. Substituting a mixed pixel value ($54^{\circ}C$ or $46^{\circ}C$) instead of the component cover temperatures ($63^{\circ}C$, $37^{\circ}C$) will produce large inaccuracies in surface flux calculations.

Operational success of surface flux models using satellite mixed pixel radiometric temperatures in place of aerodynamically derived temperatures has been reported for dense, homogeneous, vegetation covers, but there has been less success reported using this substitution for sparse vegetation covers [15]. In mixed

¹⁰And, by extension, photosynthesis. A more precise description of land covers might be photosynthetic active (healthy plants) and non-active (dead biomass and bare soil) covers. This distinction also allows for a vegetation index for the estimation of a fractional cover and is due to the photosynthesis process absorbing more red light than near infra-red light[32].

¹¹A mathematical description of a mixed pixel is given in Section 2.3.

pixel residual models, the mixed aerodynamic temperature is replaced by the LST, but when compared to measured H (Equation (2)) this often showed large disparities for sparse vegetation covers. Attempts were made to reconcile the difference by adjusting the atmospheric heat transfer resistance value, r_a , through changing the roughness length and other factors. This proved to be operational only on a case-by-case basis, with extensive *a priori* knowledge on soil and vegetation characteristics required.

The variability of temperatures for sparse covers at different views was considered by some researchers to be an impediment for mixed pixel radiometric implementation in flux models [10], while others [11] have used this behavior to infer separate soil and vegetation temperatures, which can then be used in two-source modeling of the covers. Knowing separate land cover temperatures allows for the decoupled calculations of the residual latent heat, LE , for soil and vegetation surfaces individually, and therefore gives two sources to the overall usage of water. Studies have shown that two-source energy balance flux models are better suited for modeling sparse vegetation covers than single-source, mixed models [21, 26, 16, 33, 17, 18]. This binary separation of sources is a refinement which addresses the rough mixture of land covers both in the Penman-Montieth method and the radiometrically mixed residual energy flux balance method described above.

Using the two-source model with mixed thermal pixels requires separating

out the land cover temperature contributions in the mixed pixel. Remote sensing scientists have developed algebraic methods to “unmix”, or disaggregate, pixels into component parts and is referred to as “sub-pixel analysis.” To accomplish this, radiative transfer models are used with two views at different angles, and with known cover emissivities and perceived fractional cover of vegetation¹². So far, this line of research has been limited to near simultaneous sampling and to a specific satellite platform¹³. For this reason, the intent of this dissertation is to broaden the investigation of radiative transfer separation of cover temperatures in a mixed pixel to include time-delayed sampling, possibly allowing the use of other aerial and orbital platforms.

1.3 Focus of study.

This study considers the estimation of factors used in a novel non-linear algebraic system for separating land cover temperatures, with samples derived from time-delayed, bi-angular mixed cover brightness temperature views¹⁴. The proposed system extends the linear Stefan-Boltzmann formulation of two (near) simultaneous data samples by using the total derivative of mixed temperatures with respect to fractional vegetation cover, as the second equation required for discriminating average soil and vegetation temperatures.

¹²Perceived fractional cover refers to the fractional vegetation cover as seen by the sensor. Actual and perceived fractional covers are equivalent at nadir but diverge as view angle increases.

¹³The Along Track Scanning Radiometer (ATSR) platform from the European Space Agency (ESA).

¹⁴A “brightness temperature” is what the radiometer sensor “sees”. Adjustments are made with emissivity values to get true surface temperatures for gray-body radiators.

This non-linear system was cast with tandem weather satellites in mind since their orbits can provide reasonably different view angles. However, this approach is saddled with the penalty of having to account for meteorological variances influencing the sample sites between views. Including the total derivative equation in the algebraic system addresses these influences when considering time-delayed sampling and is a feature lacking in current remote sensing models. This study focuses on the soil and vegetation temperature differential factors, which cannot be observed directly in the mixed pixel, but must be inferred for the non-linear system to deliver accurate estimates.

It is important to note that the binary cover approach is a simplified version of sunlit and shaded land covers, or a quaternary¹⁵ cover, and that the binary approach is used in most studies. The scope in this study is limited to the binary version of soil and vegetation covers and serves as a constructive step toward a quaternary implementation.

1.4 Background.

Modern satellite spatial resolutions in the thermal image bands are too coarse for addressing individual ground covers and their associated water dynamics. Algebraic methods using bi-angular views have been developed by others, and expanded on by this researcher, to overcome this resolution limitation, so that land cover temperature values can be resolved without spatial segmentation

¹⁵Quaternary means to consist of four.

of covers, hence a *sub-pixel* analysis¹⁶.

As the current literature suggests, these models can be used for water usage purposes, but are practical only on *large* farm fields and range lands using currently available weather satellite data¹⁷, since the spatial resolution and land registration accuracy of $\pm 2 km$ (for AVHRR) limits applications to large homogeneous expanses. However, as thermal resolutions become finer on future platforms, the techniques developed from this, and other works, could be applied to nominal crop fields¹⁸.

Bi-angular view methods have been developed which make use of visible and thermal bands to separate component cover temperatures and have been tested using ESA's ATSR platform. Li, *et al.* [22], uses algebraic inversion techniques with geometric knowledge¹⁹ of the target canopy, much like Kimes [13] and others have used. Jia, *et al.* [11], applies a simpler approach by using sensed cover fractions together with the sensed brightness temperature, after atmospheric correction, in Planck's equation. Results from this method were considered good since non-stressed canopy temperatures were tracking air temperatures, generally considered as a good baseline [6].

Unfortunately, at the time of this writing, the ATSR platform and its

¹⁶Put another way: what is in the pixel can be determined but not where in the pixel.

¹⁷Such as data from the Advanced Very High Resolution Radiometer (AVHRR) and the Moderate Resolution Imaging Spectroradiometer (MODIS) sensor platforms .

¹⁸By the same token, as thermal spatial resolutions approach decimeter levels, these techniques will not be required since direct individual segmentation will be achievable.

¹⁹Such as plant structure, height and spacing.

more advanced version, AATSR, have been decommissioned. Relatively few land products were developed using the ATSR data because the ATSR's focus was on sea, and not land, temperatures. The main use of ATSR bi-angular views was to correct for atmosphere effects on sea surface temperatures, which are relatively more homogeneous when compared to land diversity in covers and topography. The ATSR platform had two radiometric sensors, one looking forward at about fifty-two degrees and the other looking straight down, or at nadir. From the time the forward view takes a sample it takes about two minutes for the nadir sensor to re-sample the area. This difference in time was considered negligible and so the samples are considered to be near simultaneous.

Sensor platforms other than the ATSR might be usable. Synoptic, coordinated aerial views could give simultaneous views at different angles, or even an aerial emulation of the ATSR could be employed. Another approach might be to use existing polar orbiting weather satellites. These nadir and side viewing sensor platforms, when in tandem, could be usable if they are close in time and in orbital tracks. For example, if a twenty to forty minute separation is required, a satellite and its backup might be usable, such as NOAA-19 and NOAA-18, since the satellites fly close together in a slightly different orbital track, possibly providing practical view angle differences, depending on orbital track difference. If a three or four hour time delay is required, then morning and afternoon passes, such as METOP-A and NOAA-19, might be used depending on the orbital tracks.

MODIS platforms could also be combined with the above for intermediate time requirements.

Nevertheless, the time delay in using different satellites was considered problematic and little work has been done to address this potential use of bi-angular views from different satellites to determine land component temperatures [22, 35, 34]. The main objections are based on the requirement of many, and often unobtainable, meteorological values used in highly deterministic models. This dissertation addresses these objections with basic research in two ways. First, by reinterpreting a previously developed algebraic system, and as a result, implementing unused differential coefficients of that system which can encapsulate changes in surface temperatures due to changes in meteorological influences, over time. Secondly, by investigating if these coefficients are correlated to difference values of readily available weather data, such as air temperature and relative humidity. A reasonable correlation, or trending, would allow a simplified approach for estimating these coefficients.

1.5 Outline of Study.

Chapter 2 lays the theoretical foundation for the non-linear algebraic system used in this study and gives the hypothesis. Previously developed linear algebraic systems are described and a reinterpretation is developed and enhanced. Geometric and area issues are described when sampling from two views. A discus-

sion is presented on the parametrization of the differential coefficients and their estimation becomes the basis of this dissertation's hypothesis.

Chapter 3 explains the methods used in the computational implementation of the algebraic systems. Results using synthetic and laboratory data are given and discussed. Chapter 4 expands the methodology used in the field applications. Results are analyzed and discussed. Chapter 5 summarize, offers conclusions and recommendations for future work.

2 THEORY

This chapter presents the theory used in separating binary land cover temperatures, using two time-delayed radiometric samples with different views. The theory is first developed as a linear algebraic system but later enhanced into a non-linear system as components are introduced by this researcher in order to address view effects and time-delayed meteorological influences. Estimating the differential coefficients associated with these components becomes the focus of study and is addressed in the subsequent chapters after the theoretical foundation is given below.

In this chapter, practical interpretations of vegetation fractional cover are discussed within the contexts of instantaneous and time-delayed sampling. Radiative mixed pixel transfers (linear and non-linear) are also discussed along with the algebraic methods used to unmix cover temperatures with two radiometric views. Components introduced into the enhanced algebraic system are identified as describable through empirical means for land parcels. The dissertation hypothesis is given thereafter.

2.1 Vegetation fractional cover.

A key point in this study is to distinguish between two interpretations of vegetation fractional cover and their usage. The actual fractional cover over soil is defined as the perpendicular projection of vegetation to the ground, so that the

ratio of vegetation cover area to soil cover area is given as a fraction, f_a , with the subscript “a” denoting actual coverage. Studies on cover temperature behavior typically use actual vegetation fractional cover values [25].

A sensor’s view of a parcel of land introduces a second and different interpretation of fractional cover: that the vegetation cover is now a function of view angle, θ , from the surface perpendicular,

$$f_\theta = G(\theta) \tag{3}$$

with the subscript “ θ ” denoting a sensor perceived value at some angle. At a nadir view, where $\theta = 0$, we have $f_\theta = f_a$. For other view angles we have different fractional values, depending on vegetation canopy geometries.

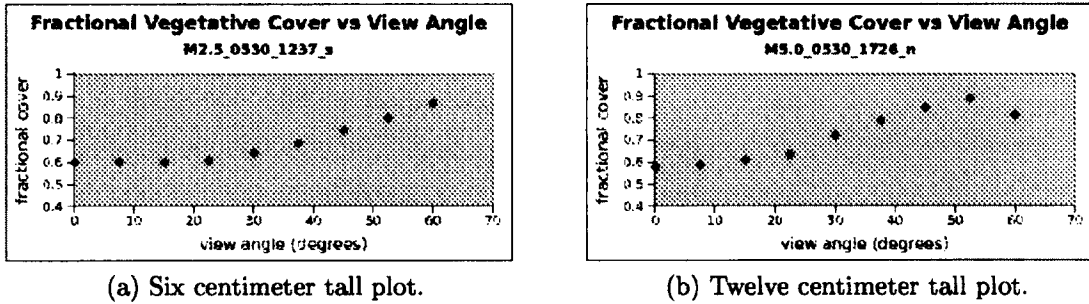


Figure 1: Typical graphs for sampled fractional vegetation cover as a function of view angle, $f_\theta = G(\theta)$, for marigold field plots.

Figure (1) shows typical values for two field plots of marigolds sampled with view angles separated by intervals of approximately seven and a half degrees²⁰. One field plot had plants six centimeters tall while the other had plants twelve

²⁰Sampling details are given in the Methods chapter.

centimeters tall, depicted by Figures (1)a and (1)b respectively. The graphs show that as the view angle increases so does the vegetation contribution to the sensor. This is due to the three dimensional structure of the vegetation canopy since the angle is providing more of a side view of the canopy. Side views also obscure soil cover; so as the angle increases, the soil contribution to the sensor diminishes. Another data sampling attribute is, that as the view angle increases so does the area sampled, so for an oblique angle of about fifty-two degrees the area sampled is twice as large as from nadir²¹.

The graphs in Figure (1)a show the sampling response for the six centimeters tall plot indicating that, at degree values less than twenty-two, fractional values do not vary much. Beyond twenty-two degrees we see a monotonically increasing function up to sixty degrees. Similar responses can be seen for the twelve centimeter tall field plot (shown in Figure (1)b), except for the last sample at sixty degrees, where soil contributions re-enter, due to looking underneath the canopy. In general, view angles greater than fifty-two degrees are problematic due to the exponential increase in area sampled, described in Appendix (E). Limiting the view angle values from about twenty-two to fifty-two degrees allows for the use of the inverse function of Equation (3),

$$\theta = G^{-1}(f_{\theta}) \quad (4)$$

²¹Refer to Appendix E for an analysis.

because of the monotonically increasing behavior in this range. This will be used later for parametrization purposes, put forth in context of time-delayed sampling and is presented in Section (2.6).

2.2 Using NDVI as a fractional vegetation index.

Determining the vegetation fraction, f_{θ} , as seen by the sensor, is problematic using current weather satellite sensors. This is due to the lack of spatial resolution, in the visible bands, to discriminate between the land covers and is similar to the lack of resolution in the thermal bands required to discriminate between land cover temperatures. For example, the MODIS sensors vary in spatial resolutions through the spectral bands so that infrared, near-infrared and visible bands have resolutions of about one kilometer, half kilometer, and quarter kilometer, respectively. The older AVHRR sensors have the same spatial resolution in all thermal and visible bands, at about one kilometer.

In 1979, a series of experiments [32] popularized a method known as the Normalized Difference Vegetation Index (NDVI) which gives a reasonable measure of healthy vegetation in low resolution data by normalizing the ratio of two bands, *red* and near-infrared (*nir*). This method is based on the ability for vegetation to greatly absorb the red band (due to photosynthesis) and to reflect the near-infrared band. So, for pixels with mostly a vegetation cover contribution, we can expect $\frac{nir}{red} > 1$. Soil reflects both bands about equally, so for pixels with mostly

soil we can expect $\frac{nir}{red} \approx 1$. Also, water absorbs more *nir* than *red*, so for pixels with mostly water we can expect $\frac{nir}{red} < 1$. This simple ratio gives a range of $[0, \infty)$, while the normalized version,

$$NDVI = \frac{nir - red}{nir + red}$$

gives an inclusive range of $[-1, 1]$ which removes the computational hazard of dividing by zero. However, the real value of the normalized rearrangement is that it reduces solar angle effects.

Many methods have been proposed to derive an actual fractional cover, f_a , from the NDVI ratio [9]. A frequently used method [37] is to observe minimum and maximum NDVI values throughout the growing season and then use the sensed NDVI as an index between the two extremes,

$$f_a = \frac{NDVI - NDVI_{min}}{NDVI_{max} - NDVI_{min}}$$

but this approach requires *a priori* extreme values with seasonal repeatability. It is also based on nadir views and does not consider oblique views.

The approach for this study is more pragmatic and follows the method described in Section (2.1) describing f_θ as a function of view angle, θ . That is, for each view angle sample, vegetation and soil covers were segmented in order to derive f_θ and a NDVI value was calculated by averaging *red* and *nir* values

in the scene (to emulate a low resolution pixel). This is a local approach, in both time and area, to characterize the $(NDVI, f_{\theta})$ relationship by using higher resolution sensors to segment out covers and can be used operationally for periodic calibrations *in situ*. Scatter plots in Appendix (F.5) of $NDVI$ and f_{θ} show high correlation of determination values, R^2 , (~ 0.94) for experimental field values and the trend function developed was used as a surrogate for f_{θ} . Section (4.4.2) discusses the results using this method.

2.3 Mixed thermal pixel.

The concept of a mixed thermal pixel is presented in this section. A radiometric sensor quantifies the radiant thermal energy that falls on it, over time, as an intensity value. When sensors are arranged together as a two-dimensional array they can render an image of thermal emissions. Each of the array sensors can be considered as a “pixel”, or picture element, of the image. This is similar to the output pixel of a computer monitor, but is an input pixel on the sensor.

A pixel with intensity contributions from different sources is called a “mixed pixel”, as opposed to a “pure” pixel with just one source. These sub-pixel source components are called end-members and their contributions to the pixel’s intensity, I_p , can be defined linearly as:

$$I_p = \sum_{i=0}^{N-1} f_i a_i$$

where N is the number of end-members, a_i is the areal intensity contribution from

end-member i , f_i is the fractional cover of the end-member over the total source area, with the constraints of $\sum_0^{N-1} f_i = 1$ and $0 \leq f_i \leq 1$.

For a thermal sensor pixel, the areal intensity, a_i , is based on the Stefan-Boltzmann gray-body energy equation $F = \varepsilon\sigma T^4$, where F is the radiant energy flux, ε is the emissivity of the surface, σ is the Stefan-Boltzmann constant, and T is the surface temperature of the source. Therefore, exposing the sensor pixel to thermal radiation over time yields an energy intensity value that is directly proportional to surface temperature.

For a binary cover with two flux end-members, we can construct the radiative component transfer equation as:

$$F_m = f_0 F_0 + f_1 F_1$$

where m denotes a “mixed” value. Substituting $F = \varepsilon\sigma T^4$ into the above equation gives,

$$\varepsilon_m \sigma T_m^4 = f_0 \varepsilon_0 \sigma T_0^4 + f_1 \varepsilon_1 \sigma T_1^4$$

and, for a binary land cover of vegetation and soil end-members, we can write

$$\varepsilon_m \sigma T_m^4 = f_\theta \varepsilon_v \sigma T_v^4 + (1 - f_\theta) \varepsilon_s \sigma T_s^4$$

where f_θ is the sensor perceived vegetation fraction and ε_m , ε_v and ε_s are the

mixed, vegetation and soil emissivity values respectively. The cover temperatures, T_v and T_s , are the average temperature for each cover. Since the Stefan-Boltzmann constant, σ , appears on both sides of this equation it can be omitted, so that,

$$\varepsilon_m T_m^4 = f_\theta \varepsilon_v T_v^4 + (1 - f_\theta) \varepsilon_s T_s^4. \quad (5)$$

To illustrate the radiative transfer process from cover components to mixed thermal values, consider the images given in Figure (2). On the left of Figure (2)a is a thermal image of a twelve centimeters tall marigold field plot taken at nadir. The thermal camera (a radiometer matrix) has a resolution of 320 x 240 pixels, with each pixel reporting a brightness temperature value. On the right of Figure (2)a is the one pixel rendering of the left image as a mixed temperature value, T_m . The rendering was done by segmenting canopy from soil, assigning known emissivities to each cover, and calculating true temperatures for each cover. The averaged cover temperatures are used on the right-hand side of Equation (5) along with the perceived fractional vegetation cover, f_θ , that was obtained during the cover segmentation. Defining the mixed emissivity as $\varepsilon_m = f_\theta \varepsilon_v + (1 - f_\theta) \varepsilon_s$ allows the mixed value, T_m , to be calculated.

Similarly, the thermal image on the left of Figure 2b is an oblique view of the field plot and the image on the right is the mixed pixel temperature value. Since there is more canopy presented to the sensor in this view the mixed pixel is brighter.



(a) Nadir view (left) and mixed pixel (right).



(b) Oblique view (left) and mixed pixel (right).

Figure 2: Thermal images of marigolds and corresponding mixed pixel.

To reiterate, our task is to separate out land cover temperatures using mixed pixel samples, like those found in low-resolution satellite radiometers. The approach taken is to characterize the process with a high resolution radiometer and then to emulate the mixed pixel. This process is explained in more detail in the Methods chapter.

2.4 Prior work using radiative transfer mixing.

Separation of soil and vegetation temperatures is a key component in two-source surface flux models and accurate discrimination is essential to the models, as discussed in the introduction. Algebraic methods have been developed which make use of bi-angular views, and most require aerodynamic contributions to separate out the radiation loads in low-resolution mixed pixels [26, 16, 19]. Another

approach requires canopy gap and atmospheric radiation values [22]. Some of these methods have been implemented using the ATSR satellite platform, where an area of interest is sampled twice at different angles along the same orbital track, with a time lag of about two minutes.

In particular, Jia, *et al.* [11], developed an ATSR application that ignores aerodynamic and radiation effects between samples and assumes Lambertian surfaces²². An algebraic system of equations is constructed based on Planck's equation for a black body,

$$B_{\lambda}(T) = \frac{2hc^2/\lambda^5}{e^{hc/\lambda k_b T} - 1}$$

where $B_{\lambda}(T)$ is the radiance²³ at some wavelength, λ , and temperature T . The constants h , k_b and c are Planck's, Boltzmann's and speed of light values, respectively. So, for some wavelength λ and two (near) simultaneous views, the system of equations can be expressed as,

$$B_{\lambda}(T_{m0}) = f_{\theta 0} \varepsilon_{\lambda v} B_{\lambda}(T_{v0}) + (1 - f_{\theta 0}) \varepsilon_{\lambda s} B_{\lambda}(T_{s0}) \quad (6)$$

$$B_{\lambda}(T_{m1}) = f_{\theta 1} \varepsilon_{\lambda v} B_{\lambda}(T_{v1}) + (1 - f_{\theta 1}) \varepsilon_{\lambda s} B_{\lambda}(T_{s1})$$

where $f_{\theta n}$ is the perceived (sensed) fractional vegetation cover for a sample n , T_{vn}, T_{sn} are the real averaged temperatures for vegetation and bare soil covers,

²²A Lambertian surface emits radiation equally in all directions.

²³Defined as the energy per second per surface area per steradian, $J s^{-1} m^{-2} sr^{-1}$.

and $\varepsilon_{\lambda v}$, $\varepsilon_{\lambda s}$ are the surface emissivity factors for the covers. Near simultaneous sampling allows the assumption that cover temperatures do not change significantly, so $T_{v0} \approx T_{v1} \approx T_v$ and $T_{s0} \approx T_{s1} \approx T_s$. T_{mn} is the brightness temperature as seen by a radiometer and is defined as $T_{mn} = B_{\lambda}^{-1}(\varepsilon_{\lambda m} B(T_{mr}))$, where $\varepsilon_{\lambda m} = f_n \varepsilon_{\lambda v} + (1 - f_n) \varepsilon_{\lambda s}$ and T_{mr} is the real mixed temperature. This system can be solved for averaged T_s and T_v by a Newton-Raphson iteration using the approximation $B_{\lambda}(T_m) \cong \sigma T_m^4$ as the initial value [11].

A simplified, analogous, version of System(6)²⁴ can be rendered, as described above in Section (2.3), by using the Stefan-Boltzmann formulation of a mixed pixel with two end-members (soil and vegetation) where the partitions have negligible energy and water exchange. This implies separate water availability for surface soil and vegetation, which is reasonable for rooted plants with respect to soil skin²⁵ surface [26]. To recap, the linear temperature mixing function to the sensor is defined as,

$$\varepsilon_m T_m^4 = f_{\theta} \varepsilon_v T_v^4 + (1 - f_{\theta}) \varepsilon_s T_s^4 \quad (7)$$

where T_m is the mixed real surface temperature²⁶. Assuming the emissivities can be determined or estimated, the equation can be used twice in the system, as above, with different values from separate views,

²⁴Henceforth, a system of equations will be referred to as a "System."

²⁵A term used to indicate infinitesimally thin.

²⁶Satellite products provide this value with atmospheric corrections.

$$\varepsilon_{m0}T_{m0}^4 = f_{\theta0}\varepsilon_vT_{v0}^4 + (1 - f_{\theta0})\varepsilon_sT_{s0}^4 \quad (8)$$

$$\varepsilon_{m1}T_{m1}^4 = f_{\theta1}\varepsilon_vT_{v1}^4 + (1 - f_{\theta1})\varepsilon_sT_{s1}^4.$$

Both samples are close in time for the ATSR (<2 minutes), so again, the assumption for System (8) is that $T_{v0} \approx T_{v1} \approx T_v$ and $T_{s0} \approx T_{s1} \approx T_s$. System (8) can be expressed in matrix notation as,

$$\begin{bmatrix} f_{\theta0}\varepsilon_v & (1 - f_{\theta0})\varepsilon_s \\ f_{v1}\varepsilon_v & (1 - f_{\theta1})\varepsilon_s \end{bmatrix} \begin{bmatrix} T_v^4 \\ T_s^4 \end{bmatrix} = \begin{bmatrix} \varepsilon_{m0}T_{m0}^4 \\ \varepsilon_{m1}T_{m1}^4 \end{bmatrix}. \quad (9)$$

2.5 Extending the radiative transfer system to include differential coefficients.

Zhang, *et al.* [35, 36, 37], extends System (8) for use with a single satellite pass, using a differential equation as the second equation. Zhang's hypothesis is that within a sampled region of land there exist pixels with same water availability, and given similar surface characteristics and radiation loads, the separate soil and vegetation temperatures are expected to remain constant as the vegetation cover varies. This allows for a differential equation to be used in a linear system.

Studies have shown that mixed temperature values of land covers for different fractional covers fall within a trapezoid distribution constructed over (T_m, f_a) space [24, 4, 8], as shown in Figure(3). Zhang's approach makes use of this (T_m, f_a) space from a single satellite pass in that theoretical wet-cool and dry-warm bound-

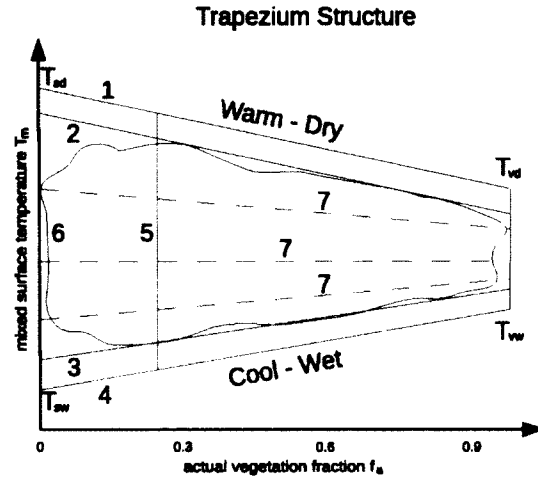


Figure 3: Theoretical position of lines in (T_m, f_a) space: 1, absolute dry line; 2, actual dry line; 3, actual wet line; 4, absolute wet line; 5, vegetation fraction isoline; 6, scatter plot envelope of mixed pixel temperatures in (T_m, f_a) space; 7, isolines of $\frac{dT_m}{df_a}$ with constant water availability. From Zhang, et al., [35, 37].

aries of the trapezium distribution can be estimated by sample points if a sufficient spread in data values exists. However, Zhang also explains that more accurate boundaries can be calculated by using extreme wet and dry sample points, on both bare soil and full vegetation cover values, at the corners of the trapezium. A sample point between these boundaries is used to determine an isoline of constant soil and vegetation temperatures with varying coverage (by virtue of ratios obtained from the equal vegetation fraction isoline), with the assumption of constant water availability. Maintaining constant soil and vegetation temperatures over varying fractional cover then constrains the measured mixed temperature value as an isoline in (T_m, f_a) space. Calculating the slope of the constant water availability and constant cover temperature isoline, $\frac{dT_m}{df_a}$, gives a coefficient necessary in a system

of equations for solving the cover temperatures, as described below.

An algebraic linear system is constructed with the first equation based on the Stefan-Boltzmann formulation of a mixed pixel, Equation (7). Taking the total derivative of Equation (7) with respect to actual fractional vegetation cover, f_a , gives the second equation for the new algebraic system,

$$\begin{aligned}\epsilon_m T_m^4 &= f_a \epsilon_v T_v^4 + (1 - f_a) \epsilon_s T_s^4 \quad (10) \\ 4\epsilon_m T_m^3 \frac{dT_m}{df_a} + T_m^4 \frac{d\epsilon_m}{df_a} &= \epsilon_v T_v^4 - \epsilon_s T_s^4.\end{aligned}$$

Here, the rate of change of the mixed emissivity is defined as $\frac{d\epsilon_m}{df_a} = \epsilon_v - \epsilon_s$ ²⁷.

Assuming the cover temperatures do not change with respect to actual vegetation fraction then $\frac{dT_s}{df_a} = 0$ and $\frac{dT_v}{df_a} = 0$, and are not part of the second equation²⁸, allowing for system closure.

2.5.1 Reinterpreting the mixed temperature differential coefficient, $\frac{dT_m}{df_a}$ as $\frac{dT_m}{df_\theta}$.

This study addresses issues concerning time-delayed sampling, in addition to the *sensor-perceived* changes from two views. However, this section addresses only the sensor-perceived changes and does so by this researcher's reinterpretation of $\frac{dT_m}{df_a}$ as $\frac{dT_m}{df_\theta}$, the change in mixed temperature with respect to perceived fractional vegetation cover from different view angles, and leaves consideration

²⁷See Equation (29) in Appendix (C)

²⁸Refer to Appendix C for full calculations.

for the changes between samples over time, due to energy loads and aerodynamic differences, for Section 2.6. These perceived changes are generated by geometric effects, and possible non-Lambertian surface attributes, and are henceforth called “view effects”.

Consider, for the moment, that soil and vegetation temperatures remain constant for simultaneous different views on a Lambertian surface so that, as above, the cover temperatures do not change with respect to perceived fraction, so that $\frac{dT_s}{df_\theta} = 0$, $\frac{dT_v}{df_\theta} = 0$. Then, for both the Zhang approach and the two-view reinterpretation, System (10) can be used to solve for vegetation and soil temperatures, T_v and T_s . So, for different views and in matrix notation, the system becomes,

$$\begin{bmatrix} f_\theta \varepsilon_v & (1 - f_\theta) \varepsilon_s \\ \varepsilon_v & -\varepsilon_s \end{bmatrix} \begin{bmatrix} T_v^4 \\ T_s^4 \end{bmatrix} = \begin{bmatrix} \varepsilon_m T_m^4 \\ 4\varepsilon_m T_m^3 \frac{dT_m}{df_\theta} + T_m^4 \frac{d\varepsilon_m}{df_\theta} \end{bmatrix}.$$

This is congruent with System (10) but with the fractional differential coefficient, $\frac{dT_m}{df_\theta}$, influenced by perceived view effects.

2.5.2 Factoring for view effects.

The mixed temperature rate of change with respect to perceived fraction, $\frac{dT_m}{df_\theta}$ can now be calculated from two views and this would be sufficient for system closure if the view effects are restricted to only an increase of vegetation temperature contribution and a decrease of soil temperature contribution from oblique

views²⁹. However, this is unrealistic since the view effects include outright different sampling of vegetation and soil covers from a centered nadir view to a centered oblique view. As more vegetation cover is introduced into the oblique views, the soil cover contribution is diminished, restricting the amount of soil being sampled. Moreover, depending on the canopy structure, an oblique view angle can include sub-canopy influences, such as canopy temperature gradients. Non-Lambertian effects are also expected. These inherent sampling variances contribute to a divergence in temperature values for each land cover in simultaneous samples at different views. To address these issues, the terms $\frac{dT_s}{df_\theta}$ and $\frac{dT_v}{df_\theta}$ are reintroduced³⁰ in this study into System (10) which gives,

$$\begin{aligned} \epsilon_m T_m^4 &= f_\theta \epsilon_v T_v^4 + (1 - f_\theta) \epsilon_s T_s^4 & (11) \\ 4\epsilon_m T_m^3 \frac{dT_m}{df_\theta} + T_m^4 \frac{d\epsilon_m}{df_\theta} &= \epsilon_v T_v^4 - \epsilon_s T_s^4 + f_\theta 4\epsilon_v T_v^3 \frac{dT_v}{df_\theta} + (1 - f_\theta) 4\epsilon_s T_s^3 \frac{dT_s}{df_\theta} \end{aligned}$$

and becomes non-linear due to the different degrees in the variables, T_v and T_s . This system can be solved for any point in f by substitution and with known differential coefficients along the continuum of f . A discrete implementation of System (11) is discussed in detail in the Methods chapter.

²⁹See the Methods chapter for verification using synthetic data.

³⁰From the total derivative with respect to perceived fractional cover, $\frac{d(\epsilon_m T_m^4)}{df_\theta}$, see Appendix C.

2.6 Parametrization of the temperature function and coefficients.

It is because of the perceived differences in the data from two views that useful information can be extracted and understanding the composition of the factors inducing these differences becomes key in applying the above methods toward more complex situations. Simultaneous bi-angular view sampling has its own set of variance factors (due to geometric and non-Lambertian effects), but for large time spans in view sampling, as in tandem satellite passes, the aerodynamic and energy interactions are also expressed in the data and cannot be ignored. This section describes how System (11) can be used in situations with environmental effects in addition to view effects.

2.6.1 Environmental effects over time.

So far, this study's reinterpretation and adaptation of System (10) allows for a perceived $\frac{dT_m}{df_\theta}$ to be calculated from two simultaneous views. Extending the algebraic System (10) with the terms $\frac{dT_v}{df_\theta}$ and $\frac{dT_s}{df_\theta}$ is proposed above to compensate for view effects in System (11), if their values are known. However, using time-delayed samples also introduces additional meteorological effects through varying radiation, moisture, and aerodynamic contributions from one point in time to another and, strictly speaking, these influences are derived from meteorological differences rendered in the time slices and not directly from time itself. A further extension is proposed in that the differential coefficients, $\frac{dT_v}{df_\theta}$ and $\frac{dT_s}{df_\theta}$, can also

encapsulate environmental influences over time.

The suggestion that the differential coefficients, $\frac{dT_v}{df_\theta}$ and $\frac{dT_s}{df_\theta}$, take on influences driven by the environmental over time seems abstract because the coefficients are expressed with respect to fractional cover and not to environmental variables or even time. A reconciliation becomes necessary and is put forth below.

Consider rearranging Equation (2) so that for either a soil or vegetation surface the cover aerodynamic temperature, T_{ao} , can be expressed as

$$T_{ao} = T_a + \frac{r_a H}{\rho C_p}$$

where ρC_p is the volumetric heat capacity of the air, T_a is the air temperature at some reference height, r_a is the surface-to-atmospheric resistance to heat transport (and is a function of wind friction velocity, displacement height, roughness coefficients based on shape, and other factors). The sensible heat flux H , from the energy balance Equation (1), is a function of net radiation, R_n , possible ground conduction, G , and latent heat, LE . The latent heat is also a functions of relative humidity, R_h , wind velocity, V_w , air pressure, P_a , and other weather variables. So, in general, the surface aerodynamic temperature, T_{ao} , can be expressed as a function of almost innumerable and difficult to obtain environmental values as,

$$T_{ao} = F(T_a, R_n, R_h, V_w, P_a \dots)$$

where the ellipses indicate other variables. Assuming that radiometric surface

temperatures, T_{ro} , are related to aerodynamic temperatures, T_{ao} , and subject to view effects as a function of view angle, we have $T_{ro} = G(T_{ao}, \theta)$. The above general equation can be rewritten to describe what the radiometer senses as,

$$T_{ro} = F(\theta, T_a, R_n, R_h, V_w, P_a \dots).$$

Equation (4) gives $\theta = G^{-1}(f_\theta)$, so now T_{ro} can be expressed generally as,

$$T_{ro} = F(f_\theta, T_a, R_n, R_h, V_w, P_a, \dots). \quad (12)$$

2.6.2 Identification of components.

Introducing the variable f_θ into the cover temperature function is a key feature which allows the differentiation of the other variables with respect to f_θ . Taking the total derivative of Equation (12) with respect to f_θ , and dropping the r subscript in T_{ro} , gives

$$\frac{dT_o}{df_\theta} = \frac{\partial T_o}{\partial f_\theta} + \frac{\partial T_o}{\partial T_a} \frac{dT_a}{df_\theta} + \frac{\partial T_o}{\partial R_n} \frac{dR_n}{df_\theta} + \frac{\partial T_o}{\partial R_h} \frac{dR_h}{df_\theta} + \frac{\partial T_o}{\partial V_w} \frac{dV_w}{df_\theta} + \frac{\partial T_o}{\partial P_a} \frac{dP_a}{df_\theta} + \dots \quad (13)$$

The partial differential term $\frac{\partial T_o}{\partial f_\theta}$ is now identified as the view effect component and the remaining terms are identified as the environmental effect components contributing to the total derivative $\frac{dT_o}{df_\theta}$. The term T_o will now be used as a generic reference to either soil or vegetation cover.

2.7 Theory chapter summary.

2.7.1 Overview

This chapter began by distinguishing between actual vegetation fractional cover, f_a , and perceived vegetation fractional cover, f_θ . Then, the vegetation index, NDVI, was introduced for later use as a surrogate for f_θ and to convey a simple way on how sub-pixel information can be extracted. Afterwards, radiative transfer mixing functions were defined explaining how areal components contribute to a mixed thermal pixel.

The narrative goes on to describe how previous studies used algebraic systems, based on Planck and Stephan-Boltzmann radiative transfer equations, to separate land cover temperatures using two views. Later, a single view method was described which enhanced the algebraic system by introducing a differential equation using changes in f_a .

The study then showed how the coefficient, $\frac{dT_m}{df_a}$, in the differential equation, can be reinterpreted in terms of f_θ and that two simultaneous views can be used in the enhanced system. View effects were later factored in by introducing the coefficients $\frac{dT_v}{df_\theta}$ and $\frac{dT_s}{df_\theta}$ into the differential equation. Finally, the parametrization of the generic surface aerodynamic temperature, T_{ao} , with f_θ showed how view effects *and* environmental effects both contribute to the radiometric value of $\frac{dT_o}{df_\theta}$, in time-delayed sampling, and therefore encapsulate those effects.

2.7.2 A practical interpretation of $\frac{dT_o}{df_\theta}$.

To prepare the above development by this study for practical use, a transcription of Equation (13) into a discrete formulation is proposed using the Mean Value Theorem in differential calculus. Here, the differentials $\frac{dT_o}{df_\theta}$, $\frac{dT_a}{df_\theta}$, $\frac{dR_n}{df_\theta}$, $\frac{dR_h}{df_\theta}$, etc., are assumed to have approximately the same mean value point, f_{θ_c} . This is a reasonable approach since most environmental variables exhibit sinusoidal or linear tendencies under smooth weather patterns, with both functions conveniently approximating f_{θ_c} as the mid-point between fractional values. This does not mean that the variables are in phase with each other, nor that they necessarily track each other. The discrete version of Equation (13) is therefore expressed at f_{θ_c} as

$$\frac{\Delta T_o}{\Delta f_\theta} = \frac{\partial T_o}{\partial f_\theta} + \frac{\partial T_o}{\partial T_a} \frac{\Delta T_a}{\Delta f_\theta} + \frac{\partial T_o}{\partial R_n} \frac{\Delta R_n}{\Delta f_\theta} + \frac{\partial T_o}{\partial R_h} \frac{\Delta R_h}{\Delta f_\theta} + \frac{\partial T_o}{\partial V_w} \frac{\Delta V_w}{\Delta f_\theta} + \frac{\partial T_o}{\partial P_a} \frac{\Delta P_a}{\Delta f_\theta} + \dots$$

where $\frac{\Delta T_o}{\Delta f_\theta}$, $\frac{\Delta T_a}{\Delta f_\theta}$, $\frac{\Delta R_n}{\Delta f_\theta}$, etc., are the averaged rates of change between samples and the partials $\frac{\partial T_o}{\partial T_a}$, $\frac{\partial T_o}{\partial R_n}$, $\frac{\partial T_o}{\partial R_h}$, etc., are unknown. The above equation can be cast as a hyper-surface in $(\Delta T_a, \Delta R_n, \Delta R_h, \Delta V_w, \Delta P_a, \dots)$ orthogonal space using a one-to-one correspondence, such that $C_1 = \frac{\partial T_o}{\partial f_\theta}$, $C_2 = \frac{\partial T_o}{\partial T_a} \frac{1}{\Delta f_\theta}$, $C_3 = \frac{\partial T_o}{\partial R_n} \frac{1}{\Delta f_\theta}$, etc. This gives

$$\frac{\Delta T_o}{\Delta f_\theta} = C_1 + C_2 \Delta T_a + C_3 \Delta R_n + C_4 \Delta R_h + C_5 \Delta V_w + C_6 \Delta P_a + \dots \quad (14)$$

and suggests that a deterministic approach to obtain $\frac{dT_a}{df_\theta}$ is worth exploring, if the coefficients C_1, C_2, \dots, C_n can be sufficiently characterized and weather differential (eg. $dT_a \approx \Delta T_a$) are known. These observations lead to the dissertation hypothesis below.

2.8 Hypothesis.

The dissertation hypothesis is based on the observation that the rate of change of a mixed radiometric temperature with respect to actual fractional vegetation cover, $\frac{dT_m}{df_a}$, originally constructed from spatially distributed land parcels, can also be constructed from bi-angular views of co-centered land parcels, but with the interpretation that bi-angular samples provide a geometrically and environmentally influenced fractional cover differential, $\frac{dT_m}{df_\theta}$. It is also observed that two other fractional differential coefficients, $\frac{dT_v}{df_\theta}$ and $\frac{dT_s}{df_\theta}$, are required to account for these effects when using time-delayed sampling, but whose values are not known when using mixed radiometric samples.

The hypothesis is that the differential coefficients, $\frac{dT_v}{df_\theta}$ and $\frac{dT_s}{df_\theta}$, can be sufficiently characterized at a local temporal scale for the accurate separation of cover temperatures in mixed samples, by trending their response to a minimum of environmental influences using high resolution sensors.

If the hypotheses is correct, then the trending can give insights into developing a more general method. This study presents a first-order approximation

method to estimate these differential coefficients.

3 METHODS and RESULTS (Part I)

This chapter develops practical computing methods for the above theory and describes their experimental applications, first by using synthetic data and then laboratory data.

A brief description is given of the pre-processing approach and computing environment used for this study. A linear discrete version of the unmixing System (11) is developed, in conjunction with synthetically generated data, as a first iteration in transitioning from a continuous context to a discrete sampling space. This is later extended to the quartic version and results are compared for residual closure.

Next, laboratory simulations were performed using potted plants and a thermal camera. Overhead and oblique view angles were exercised with the discrete implementations and evaluated. Later, in Methods (Part II), field plot acquisition and processing methods are described using both thermal and NDVI cameras. Associated experimental and data processing errors are discussed.

3.1 Data pre-processing.

The main computational goal is to separate out sub-pixel land cover temperatures given two mixed thermal views, possibly from two time-delayed satellites with different orbital tracks. Algorithms were developed in this study which exercise the above unmixing systems, and are discussed in detail below, but, for

analytic and verification purposes, pre-processing of higher resolution data is also required.

The approach is to pre-process high resolution data before applying the unmixing algorithms to an emulated mixed pixel. This is done in order to have the necessary information for closure verification and later characterization of the differential coefficients, $\frac{dT_s}{df_\theta}$ and $\frac{dT_v}{df_\theta}$. That is, a high enough resolution is used to segment out a binary cover of soil and vegetation and then the mixed pixel value is emulated and used in the unmixing systems.

This pre-process segmentation allows for fractional cover determination and average cover temperature calculations, *a priori*. In addition, cover temperatures are adjusted by user given emissivity values and a mixed emissivity value is calculated by $\varepsilon_m = f_\theta \varepsilon_v + (1 - f_\theta) \varepsilon_s$, so that a mixed pixel value can be determined using Equation (5) with the averaged values of the cover temperatures.

For each image view presented to the pre-processing programs, a line of output data is produced which lists the perceived vegetation coverage, f_θ , actual average soil and vegetation temperatures, (T_s, T_v) , emissivities, $(\varepsilon_m, \varepsilon_s, \varepsilon_v)$, and the mixed pixel temperature value T_m . This information allows for the calculations of $\frac{dT_m}{df_\theta} \cong \frac{\Delta T_m}{\Delta f_\theta}$ and $\frac{d\varepsilon_m}{df_\theta} = \varepsilon_v - \varepsilon_s$, used in the unmixing algorithms, and which would be available from two views of satellite data.

The differential coefficients, $\frac{dT_s}{df_\theta}$ and $\frac{dT_v}{df_\theta}$, can also be approximated from the output information as $\frac{\Delta T_s}{\Delta f_\theta}$ and $\frac{\Delta T_v}{\Delta f_\theta}$, respectively. Characterizing these now

obtainable coefficients, with respect to environmental changes, is the subject of our study. Before proceeding with the methods of characterization, the computing platforms, algorithmic development and methods for verification are first described below.

3.2 Processing platforms used.

The operating system used for this study is the GNU/Linux based Ubuntu. The image processing platform used is called Python On Line Imaging (POLI) and was designed and authored by this researcher³¹. POLI is based on NumPy, an extension to the programming language Python, which has sophisticated mathematical functions capable of operating on large multi-dimensional arrays.

POLI is designed for multi-band images and is based on the “piping” concept used in GNU/Linux, where small filter programs can be sequenced, on the command line, to achieve some end. That is, the output from one filter operator serves as the input for the next filter down the pipe, denoted by the “|” character. The strength of this approach is that small, yet known to work, filters can be arranged in many flexible ways for reliable execution.

For example, to implement the data pre-processing described above in Section (3.1), a user would smooth an image, segment it by thresholding and then assign emissivity values to the binary covers. The command would be:

```
% flir_source -i image.csv | tee image.poli \
```

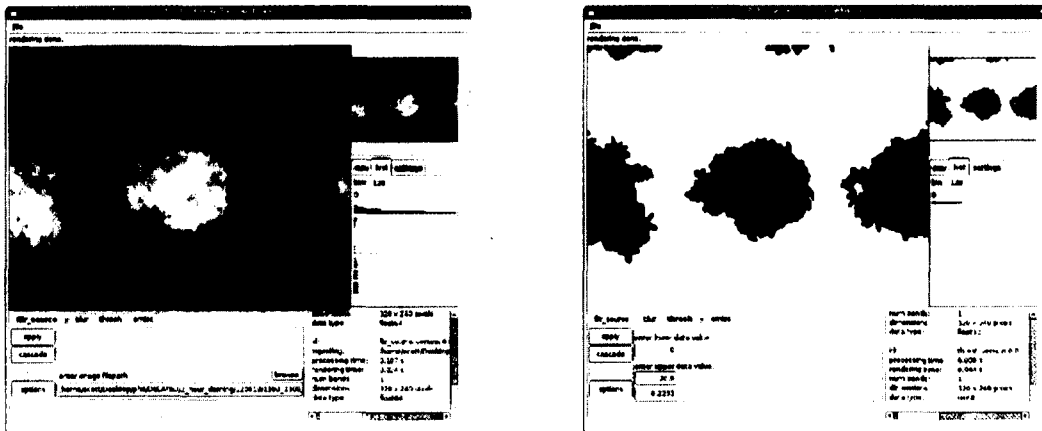
³¹The source code (in alpha version) for POLI and other programs associated with this study can be found in this dissertation’s accompanying data disk.

```
| blur -t gauss | thresh -l 0 -h 20.9 \  
| emiss -s 0.95 -v 0.99 -i image.poli
```

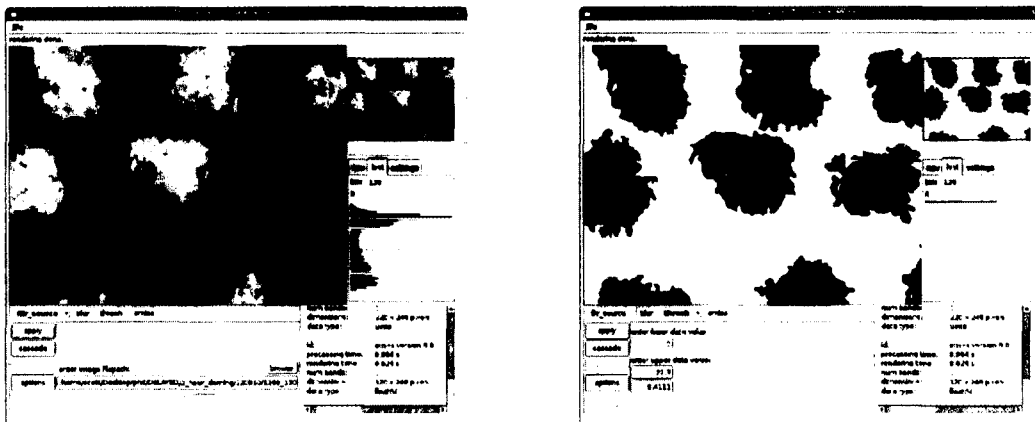
The command starts by reading a thermal image which pipes it to a filter that copies the image into a readable form for later use. The image continues down the pipe to a filter for a slight Gaussian smoothing and then is segmented to provide a mask for the “emiss” filter, which applies the mask to the previously stored image, finally outputting the necessary pre-processing information. The backslash character, “\”, indicates a line continuation.

In POLI, images and filter programs can be retrieved locally or from internet servers. Each filter is designed to be used in either the command line, as above, or directly as a class for batch applications, or to be dynamically loaded into a graphical user interface (GUI) for interactive analysis. Figure (4) shows the POLI GUI containing the same filters as in the above command line. In the GUI version, filters produce their own tabbed panel, housing parameter values which are adjustable by the user. Clicking on the filter’s tab renders the output at that point in the processing pipe, for the user’s inspection. This allows for quick analysis and parameter settings that can be later implemented using batch scripts on large amounts of data. The GUI and batch versions of POLI do not actually pipe the images, but simply point to the data.

Simple statistical analysis was done in the Gnumeric spreadsheet program. Advanced analysis was programmed in the statistical language “R”.



(a) Nadir view (left) and thermal mask (right).



(b) Oblique view (left) and thermal mask (right).

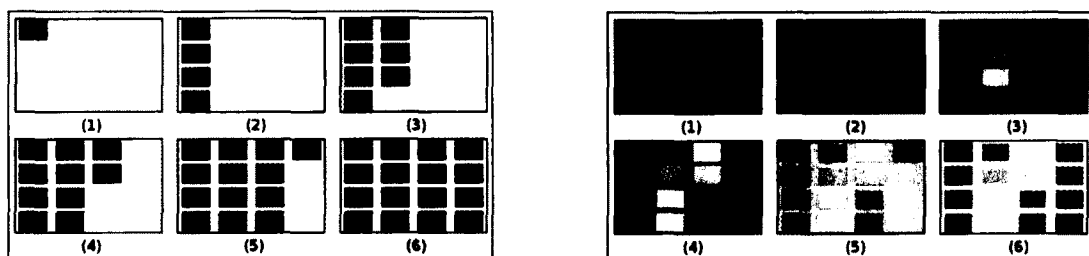
Figure 4: POLI image processing of thermal nadir and oblique views.

3.3 Algorithmic development.

Three algorithms implementing the Systems (8), (10), and (11) were developed and exercised using synthesized and sensed data, with the methods and laboratory results given below.

3.3.1 Synthetic data.

Data were synthesized to emulate a binary land cover with varying coverage and temperatures. The synthesized data consists of a background, representing bare soil, and rectangular parcels representing vegetation cover. Constant temperatures within the background and individual parcels is assumed and represents the average temperature of the components. Successive addition of “vegetation” parcels emulates the increase in vegetation contribution from different views through a spatial change of vegetation, demonstrated in the series of images of Figure (5). This is the interpretation given in Section (2.5.1).



(a) Increasing “vegetation” cover with constant component temperatures.

(b) Increasing “vegetative” cover with varying component temperatures.

Figure 5: Synthetic images used for emulating fractional cover changes for different samples. The smaller rectangles represent vegetative cover. The resulting “mixed” temperature varies with fractional cover.

Figure (5)a shows a series of images with a constant soil (white background) temperature within the image and also across the series. The black rectangles, representing vegetation, are also constant in temperature but increase in number across the series. If the vegetation parcel temperature is cooler than the soil

background then one can expect the mixed temperature of each image to decrease as the fractional cover increases. Because of the constant temperatures, the contributing differential coefficients, $\frac{dT_s}{df_\theta}$ and $\frac{dT_v}{df_\theta}$, are zero and is analogous to a simultaneous sampling over a Lambertian surface.

Figure (5)b shows images with varying soil and vegetation temperatures across the series which are used to model non-Lambertian situations and time delays. In this case, the coefficients, $\frac{dT_s}{df_\theta}$ and $\frac{dT_v}{df_\theta}$, are not zero and need to be accounted for. Here, the discrete differential implementation of the sensed data are calculated from two views and represent average slopes, so $\frac{dT_s}{df_\theta} \cong \frac{\Delta T_s}{\Delta f_\theta}$, $\frac{dT_v}{df_\theta} \cong \frac{\Delta T_m}{\Delta f_\theta}$ and $\frac{dT_m}{df_\theta} \cong \frac{\Delta T_m}{\Delta f_\theta}$. This introduces computational subtleties when reconciling with a continuous context and which need to be addressed for accurate results. A foundation is developed below to address these subtleties using a simple linearized model and then extended to the full quartic radiative transfer version of System (11).

3.3.2 Synthetic data and linearized radiative transfer.

Equation (5) is sometimes expressed in a simplified form as

$$\varepsilon_m T_m = f_\theta \varepsilon_v T_v + (1 - f_\theta) \varepsilon_s T_s \quad (15)$$

because within the expected terrestrial temperature range, the radiance output differences can be approximated linearly in the thermal band of the spectrum.

Equation (15) can be used to construct a system using two sample points,

$$\begin{bmatrix} f_{e0}\varepsilon_v & (1 - f_{e0})\varepsilon_s \\ f_{e1}\varepsilon_v & (1 - f_{e1})\varepsilon_s \end{bmatrix} \begin{bmatrix} T_v \\ T_s \end{bmatrix} = \begin{bmatrix} \varepsilon_{m0}T_{m0} \\ \varepsilon_{m1}T_{m1} \end{bmatrix}. \quad (16)$$

Taking the total derivative of Equation (15) with respect to fractional cover gives

$$T_m \frac{d\varepsilon_m}{df_\theta} + \varepsilon_m \frac{dT_m}{df_\theta} = \varepsilon_v T_v + f_\theta \varepsilon_v \frac{dT_v}{df_\theta} + \varepsilon_s \frac{dT_s}{df_\theta} - \varepsilon_s T_s - f_\theta \varepsilon_s \frac{dT_s}{df_\theta} \quad (17)$$

and assuming $\frac{dT_s}{df_\theta} = 0$ and $\frac{dT_v}{df_\theta} = 0$ allows the construction of the system

$$\begin{bmatrix} f_\theta \varepsilon_v & (1 - f_\theta)\varepsilon_s \\ \varepsilon_v & -\varepsilon_s \end{bmatrix} \begin{bmatrix} T_v \\ T_s \end{bmatrix} = \begin{bmatrix} \varepsilon_m T_m \\ \varepsilon_m \frac{dT_m}{df_\theta} + T_m \frac{d\varepsilon_m}{df_\theta} \end{bmatrix}. \quad (18)$$

Systems (16),(18) are used for navigating purposes by providing a simplified platform for analysis. While this initial approach does not exactly model radiation transfer it serves to exercise key concepts in the discrete implementation of continuous modeling.

Implementing System (16) is straight forward in that sample values are used directly. The system was exercised with the images shown in Figure (5)a for a soil brightness temperature of 30^0C and a vegetation brightness temperature of 22^0C , adjusted with $\varepsilon_s = 0.95$ and $\varepsilon_v = 0.99$. The implementation uses the first view in conjunction with successive views for the unmixing calculations, with each new view increasing the fractional cover. The results for System (16) gave cover temperature residuals on the order of 10^{-10}^0C to 10^{-11}^0C .

Implementing System (18) uses a more direct interpretation of $\frac{d(\epsilon_m T_m)}{df_\theta}$ as a slope between two discrete sample points. The total derivative is now expressed as,

$$\frac{d(\epsilon_m T_m)}{df_\theta} = \epsilon_m \frac{dT_m}{df_\theta} + T_m \frac{d\epsilon_m}{df_\theta} \cong \frac{\epsilon_{m1} T_{m1} - \epsilon_{m0} T_{m0}}{f_{\theta1} - f_{\theta0}}$$

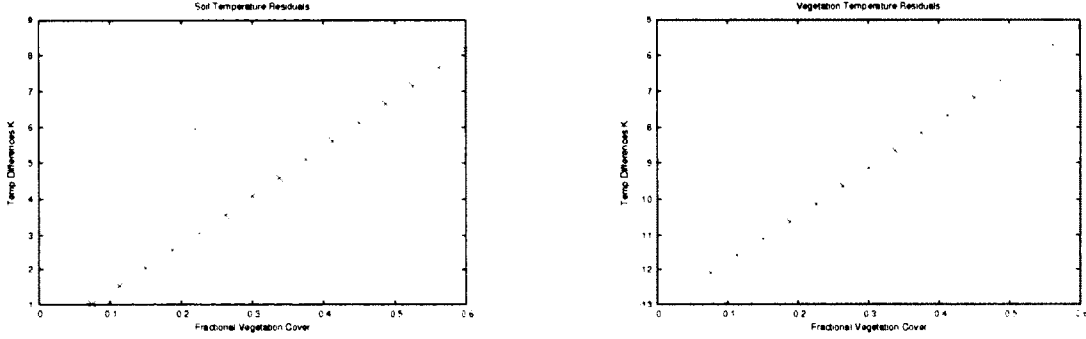
and the system becomes,

$$\begin{bmatrix} f_\theta \epsilon_v & (1 - f_\theta) \epsilon_s \\ \epsilon_v & -\epsilon_s \end{bmatrix} \begin{bmatrix} T_v \\ T_s \end{bmatrix} = \begin{bmatrix} \epsilon_m T_m \\ \frac{\epsilon_{m1} T_{m1} - \epsilon_{m0} T_{m0}}{f_{\theta1} - f_{\theta0}} \end{bmatrix}. \quad (19)$$

The first equation in System (19) can take on either endpoint view values, although when using the *second* sample point the residuals were better with complete closure on half the values, with the other half having residuals on the order of $10^{-13} \text{ } ^\circ\text{C}$ to $10^{-14} \text{ } ^\circ\text{C}$, an improvement of several orders of magnitude, from System (16).

The situation with varying cover temperatures, given in Figure (5)b, has the same initial condition as Figure (5)a but the average soil temperature increases by 0.5°C with each new view and each new “vegetation” parcel temperature increases by 0.2°C . This introduces the differential coefficients, $\frac{dT_s}{df_\theta} \neq 0$ and $\frac{dT_v}{df_\theta} \neq 0$, as additional influences to the mixed temperature T_m . Because these influences are not factored into either Systems (16),(19), we can expect the results given in Figure (6) when applied to the data depicted in Figure (5)b, showing these

systems are not suited to the dynamics by not factoring in the terms containing the differential coefficients. The residual errors reflect the temperature increases given above.



(a) “Soil” residuals, ΔT_s , from synthetic data with varying temperatures and without factors $\frac{dT_s}{df_\theta}$ and $\frac{dT_v}{df_\theta}$.

(b) “Vegetation” residuals, ΔT_v , from synthetic data with varying temperatures and without factors $\frac{dT_s}{df_\theta}$ and $\frac{dT_v}{df_\theta}$.

Figure 6: Temperature residuals using System (19) with data depicted in Figure 5(b).

However, with *a priori* knowledge of $\frac{dT_s}{df_\theta}$ and $\frac{dT_v}{df_\theta}$ as $\frac{\Delta T_s}{\Delta f_\theta}$ and $\frac{\Delta T_v}{\Delta f_\theta}$, respectively, we can factor in these influences into System (19) using Equation (17),

$$\begin{bmatrix} f_{\theta 1} \varepsilon_v & (1 - f_{\theta 1}) \varepsilon_s \\ \varepsilon_v & -\varepsilon_s \end{bmatrix} \begin{bmatrix} T_{v1} \\ T_{s1} \end{bmatrix} = \begin{bmatrix} \frac{\varepsilon_{m1} T_{m1} - \varepsilon_{m0} T_{m0}}{f_{\theta 1} - f_{\theta 0}} - f_{\theta 0} \varepsilon_v \frac{\Delta T_v}{\Delta f_\theta} - (1 - f_{\theta 0}) \varepsilon_s \frac{\Delta T_s}{\Delta f_\theta} \\ \varepsilon_v \frac{\Delta T_v}{\Delta f_\theta} - \varepsilon_s \frac{\Delta T_s}{\Delta f_\theta} \end{bmatrix} \quad (20)$$

and test for accuracies. Like System (19), judicious selection of sample point (as shown in System (20)) is required. Here, the second sample point is used in the first equation, while the first sample fraction, $f_{\theta 0}$, is used in the second equation. The interpretation is that the terms $f_{\theta 0} \varepsilon_v \frac{\Delta T_v}{\Delta f_\theta}$ and $(1 - f_{\theta 0}) \varepsilon_s \frac{\Delta T_s}{\Delta f_\theta}$ are influences on the second sample since the first sample point was taken. While

the cover temperatures, T_{s1} and T_{v1} , are explicitly solved for the second sample point, the first sample point temperatures, T_{s0} and T_{v0} , can also be solved by using $\frac{\Delta T_s}{\Delta f_\theta}$ and $\frac{\Delta T_v}{\Delta f_\theta}$ to backtrack. Using Equation (15) to linearly mix the covers, the results for System (20) with varying data are as accurate and precise as the non-varying application of System (19). It is important to state that when using linear unmixing systems, the target pixel is assumed to have been linearly mixed. Likewise, when using a quartic unmixing system the target is assumed to have been mixed using the quartic radiative transfer equation Equation (5).

3.3.3 Synthetic data and quartic radiative transfer.

The transcription from theory to application continues in this section with the more realistic, and complicated, modeling of quartic radiative transfer, expressed in the Systems (8), (10) and (11). Like the linearized version, System (8) uses the two sample points directly. Discrete versions of the Systems (10) and (11) were developed similarly as above by considering that

$$\frac{d(\varepsilon_m T_m^4)}{df_\theta} = 4\varepsilon_m T_m^3 \frac{dT_m}{df_\theta} + T_m^4 \frac{d\varepsilon_m}{df_\theta} \approx \frac{\varepsilon_{m1} T_{m1}^4 - \varepsilon_{m0} T_{m0}^4}{f_{\theta 1} - f_{\theta 0}}$$

so that System (10) becomes,

$$\begin{bmatrix} f_\theta \varepsilon_v & (1 - f_\theta) \varepsilon_s \\ \varepsilon_v & -\varepsilon_s \end{bmatrix} \begin{bmatrix} T_v^4 \\ T_s^4 \end{bmatrix} = \begin{bmatrix} \varepsilon_m T_m^4 \\ \frac{\varepsilon_{m1} T_{m1}^4 - \varepsilon_{m0} T_{m0}^4}{f_{\theta 1} - f_{\theta 0}} \end{bmatrix}. \quad (21)$$

Exercising System (21) on the non-varying cover temperature data, depicted in Figure 5(a) (with same values as above), gave residual values for soil and vegetation temperatures of $10^{-11} \text{ }^\circ\text{C}$ and $10^{-12} \text{ }^\circ\text{C}$ in both cases, and are slightly better than in the linearized radiative transfer case.

Similar to the approach used in System (20), a discrete version of the second equation in System (11) is developed by leveraging the Mean Value Theorem³², again, in order to address the situation of varying soil and vegetation temperatures,

$$\frac{\varepsilon_{m1}T_{m1}^4 - \varepsilon_{m0}T_{m0}^4}{f_{\theta1} - f_{\theta0}} = \varepsilon_v T_{v1}^4 - \varepsilon_s T_{s1}^4 + f_{\theta0} 4\varepsilon_v T_{vc}^3 \frac{\Delta T_v}{\Delta f_\theta} + (1 - f_{\theta0}) 4\varepsilon_s T_{sc}^3 \frac{\Delta T_s}{\Delta f_\theta} \quad (22)$$

The third and fourth terms of the right hand side of Equation (22) represent the contributions of $\frac{\Delta T_v}{\Delta f_\theta}$ and $\frac{\Delta T_s}{\Delta f_\theta}$, and, as in the linearized case, are interpreted to be the influences to the cover temperatures since the first sample value was taken. Unlike the linearized case, these terms require the mean values of T_v and T_s , somewhere between $f_{\theta0}$ and $f_{\theta1}$, and are denoted with the subscript c . The system remains linear because the mean values of the cover temperatures, T_{vc} and T_{sc} , between samples are used instead of the second endpoint values, T_{v1} , and

³²The prevalence of this calculus theorem in this study, exercised at different scales, cannot be overstated. Historically, this notion was formalized by the French mathematician Augustin-Louis Cauchy, about a century and a half after the philosophers Leibniz and Newton independently discovered differential and integral calculus. Cauchy's Mean Value Theorem gives a rigorous extension of calculus to N-dimensional variables and serves as the definitive basis in the Fundamental Theorem of Calculus.

T_{s1} . This construction has been verified with excellent closure, as above, by using known values of T_{vc} and T_{sc} .

Operationally, however, *a priori* knowledge of T_{vc} and T_{sc} is difficult, if not intractable, to obtain since these values depend on the very target of this study, the cover temperatures T_{v0} , T_{v1} , T_{s0} , and T_{s1} . The approach taken is to investigate how sensitive these values are to the overall system. To do so, an initial guess at the values T_{vc} , T_{sc} is given and then several iterations are made, so that new average temperatures are based on the previously calculated end values. For averaged cover temperatures values given anywhere between $273 - 330^0 K$, only *two* iterations are needed before a convergence occurs, with a closure of $\pm 0.5^0 C$, when applied to varying cover temperatures as shown in Figure (5)b. Subsequent iterations did not improve the results and, although somewhat encouraging, it leaves the linear quartic version markedly less precise than the linearized version given above, if the average values are not exactly known.

Another approach is to use a Newton-Raphson iteration method in order to better converge on the end point temperatures, even if the average temperatures are imprecise as given above. This approach is suggested by the non-linear aspect of the system in continuous space and that tangential corrections are made throughout the iterations, ever so slight in our case.

Rearranging Equation (5), in order to express T_s in terms of T_v , as

$$T_s = \left(\frac{\varepsilon_m T_m^4 - f_\theta \varepsilon_v T_v^4}{(1 - f_\theta) \varepsilon_s} \right)^{\frac{1}{4}}$$

and substituting as the second endpoint and average soil temperature values of Equation (22) gives,

$$\begin{aligned} \frac{\varepsilon_{m1} T_{m1}^4 - \varepsilon_{m0} T_{m0}^4}{f_{\theta 1} - f_{\theta 0}} &= \varepsilon_v T_{v1}^4 - \frac{\varepsilon_{m1} T_{m1}^4 - f_{\theta 1} \varepsilon_v T_{v1}^4}{(1 - f_{\theta 1})} \\ &+ f_{\theta 0} 4 \varepsilon_v T_{vc}^3 \frac{\Delta T_v}{\Delta f_\theta} \\ &+ (1 - f_{\theta 0}) 4 \varepsilon_s \left(\frac{\varepsilon_{mc} T_{mc}^4 - f_{\theta c} \varepsilon_v T_{vc}^4}{(1 - f_{\theta c}) \varepsilon_s} \right)^{\frac{3}{4}} \frac{\Delta T_s}{\Delta f_\theta}. \end{aligned} \quad (23)$$

where the values for ε_{mc} , $f_{\theta c}$ and T_{mc} can be determined from the mean values between samples. Moving the left hand side of the equation to the right hand side and using a Newton-Raphson iteration method to find the zero-crossing solves for T_{v1} . As above, a reasonable value for T_{vc} is given anywhere between 273 – 330⁰ K and a first application of the Newton-Raphson method renders temperature closures of $\pm 10^{-3}$ °C for synthetic data and, surprisingly, closures of $\pm 10^{-6}$ °C for natural sampling (non-synthetic) shown later. The poorer performance using the synthetic data has not been investigated, but is likely due to the artificial increments in the synthetic data. Using the calculated endpoint values to estimate new averaged temperatures, and applying a second iteration, can give closures of $\pm 10^{-9}$ °C, and better, for non-synthetic data.

This approach assumes that all the mean values for all considered variables

occur at the same $f_{\theta c}$, which is really not known under environmental conditions. However, if the variables take on a smooth sinusoidal or linear tendencies then using $f_{\theta c} = \frac{f_{\theta 0} + f_{\theta 1}}{2}$ is reasonable and is remarkably effective as demonstrated below in Chapter 4.

3.3.4 Comparison of linearized and quartic radiative transfer models using synthetic data.

The two right hand columns of Table (1) show the residual results, for each cover, when applying the discrete quartic System (23) to datasets with both cover temperatures varying, depicted in Figure 5(b) and mixed using the quartic radiative model, Equation (5). For comparison purposes, the results of the linearized radiative transfer model, System (20), *as applied to a quartic transfer mixing*, are presented alongside. This comparison shows how the linearized model deconstruction performs with a quartic construction, which is assumed in this study to be a more accurate description of the pixel mixing.

Table (1) shows that applying the linear deconstruction on a quartic construction gives less closure with the vegetation cover than does the quartic one, by orders of magnitude. With maximal residual values of about $\pm 0.009^{\circ}C$ across both covers, seen over a fractional spread of about 0.04 to 0.6, the quartic model appears quite usable for research and operational applications, especially where sensors are only sensitive to $0.1^{\circ}C$. The discrete, quartic, System (23) is now used with real plants in a laboratory setting, described below.

Table 1: Residual results, δT , of using Systems (20) and (23) and quartic radiative mixing on the data depicted in Figure 5(b).

% cov (f_θ)	T_s (K°)	T_v (K°)	T_m (K°)	δT_s (linearised)	δT_v (linearised)	δT_s (quartic)	δT_v (quartic)
0.037	307.06	295.89	306.65				
0.075	307.57	295.99	306.71	0.001	-0.608	0.000	0.000
0.113	308.08	296.09	306.75	0.002	-0.623	0.000	0.000
0.150	308.58	296.19	306.75	0.003	-0.636	0.000	0.000
0.188	309.09	296.29	306.73	0.003	-0.647	0.000	0.000
0.225	309.59	296.39	306.68	0.003	-0.655	0.000	-0.001
0.263	310.10	296.49	306.60	0.004	-0.661	0.000	-0.001
0.300	310.61	296.59	306.48	0.004	-0.665	0.001	-0.001
0.338	311.11	296.69	306.34	0.004	-0.666	0.001	-0.002
0.375	311.62	296.79	306.17	0.004	-0.663	0.001	-0.002
0.412	312.13	296.90	305.97	0.003	-0.658	0.002	-0.003
0.450	312.63	297.00	305.73	0.003	-0.649	0.003	-0.004
0.487	313.14	297.10	305.47	0.003	-0.637	0.004	-0.005
0.525	313.65	297.20	305.17	0.002	-0.621	0.005	-0.005
0.562	314.15	297.30	304.84	0.001	-0.601	0.007	-0.006
0.600	314.66	297.40	304.48	0.000	-0.577	0.009	-0.007

3.4 Methods and results for laboratory modeling.

The objective of the following laboratory trials is to continue testing for closure on System (23) using real plants. In this simulation, the actual fractional vegetation, f_a , emulates f_θ by increasing the plant canopy within the overhead field-of-view of an infra-red camera. Later, different view angles of a single canopy are used to vary f_θ .

A plastic container with dry sand is used to hold a live, healthy, plant canopy. The container is housed in a climate-controlled room with constant temperature. Fluorescence lamps are used to heat the box from below so that thermal shadow effects, which appear when heated from above, are minimized. Canopies

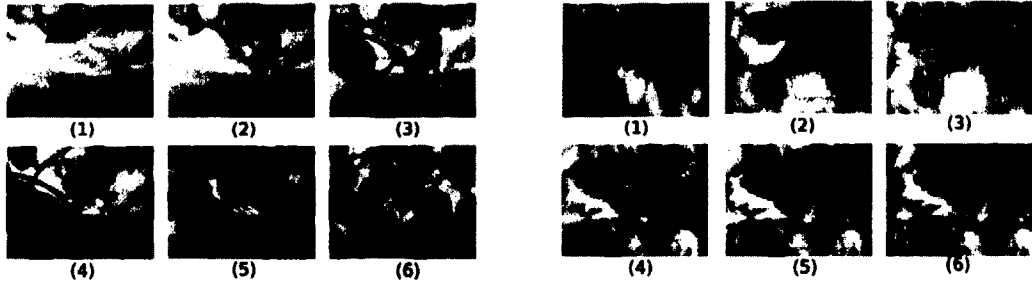
are constructed by placing potted plants inside the sand, or by placing a vine with leaves on top of the sand.

The infrared camera used, model ThermaCAM B2, is produced by FLIR Systems, Incorporated (Wilsonville, Oregon) with a detector pixel resolution of 160x120 pixels and an output resolution of 320x240 pixels. This camera measures thermal radiation energy with a wavelength response from $7.5\mu m - 13\mu m$, and has a sensitivity of $0.1^{\circ}C$ at $25^{\circ}C$, an accuracy of $\pm 2.0^{\circ}C$ and a repeatability of $\pm 1.0^{\circ}C$. Data are sampled with the emissivity set to unity, so that later, after segmenting covers, emissivities can be assigned separately to the covers in order to retrieve true temperatures. Cover emissivity values are set to $\varepsilon_s = 0.95$, and $\varepsilon_v = 0.99$ for these trials. The mixed temperature value is calculated using the same quartic radiative model, System (23), as with the synthetic data. The approach is the same: to sample separate average soil and plant temperatures over various fractional covers, emulate a mixed pixel temperature with a quartic radiative transfer model, derive $\frac{\Delta T_m}{\Delta f_{\theta}}$, $\frac{\Delta T_v}{\Delta f_{\theta}}$ and $\frac{\Delta T_s}{\Delta f_{\theta}}$ from the samples, reconstruct the component temperatures for each instance and compare calculated cover temperatures with known values.

3.4.1 Overhead implementation.

Two series of samples are taken from nadir (0°) with varying canopy. The first series, shown in Figure (7)a, uses a potted house plant, *Philodendron Scan-*

dens, to add canopy by simply placing more of the vine in the field of view. The second series, shown in Figure (7)b, uses *Viola Wittrockiana* (pansy) plants in small plastic containers buried in the sand.



(a) Increasing vegetative cover using *Philodendron Scandens*.

(b) Increasing vegetative cover using *Viola Wittrockiana*.

Figure 7: Thermal infrared images emulating view cover changes by increasing canopy over dry sand for a series of samples.

Applying System (23) to the data depicted in Figure (7)a gives results shown in Table (2) and, as with the synthetic data, expresses good closure.

Table 2: Residual results, δT , for the quartic radiative transfer System (23) using data depicted in Figure 7(a).

% cov (f_θ)	$T_s (K^\circ)$	$T_v (K^\circ)$	$T_m (K^\circ)$	$\frac{\Delta T_s}{\Delta f_\theta}$	$\frac{\Delta T_v}{\Delta f_\theta}$	δT_s	δT_v
0.067	302.32	295.02	301.83				
0.161	302.49	295.28	301.32	1.82	2.73	2.7×10^{-8}	-1.5×10^{-7}
0.376	302.13	294.95	299.42	-0.62	-0.23	-1.2×10^{-7}	2.1×10^{-7}
0.521	302.26	295.21	298.58	-0.13	0.43	1.0×10^{-8}	-9.6×10^{-9}
0.645	301.97	295.19	297.59	-0.61	0.29	-1.1×10^{-6}	6.1×10^{-7}
0.644	301.92	295.71	297.90	-0.70	1.19	-5.0×10^{-7}	2.8×10^{-7}

Columns 5 and 6 in Table (2) show values for the known differential coefficients $\frac{\Delta T_s}{\Delta f_\theta}$ and $\frac{\Delta T_v}{\Delta f_\theta}$. These values are showing the camera repeatability errors

and the thermal variances as the canopy is being constructed on the sand. These effects, and others, are seen in all remaining trials and are relatively small when compared to much larger rates in field trials. Applying System (23), using data depicted in Figure 7(b), gives results shown in Table (3).

Table 3: Residual results, δT , for the quartic System (23) using data depicted in Figure 7(b).

% cov (f_θ)	T_s (K°)	T_v (K°)	T_m (K°)	$\frac{\Delta T_s}{\Delta f_\theta}$	$\frac{\Delta T_v}{\Delta f_\theta}$	δT_s	δT_v
0.025	303.18	296.61	303.01				
0.052	302.78	295.59	302.41	-14.85	-38.44	-7.3×10^{-7}	1.4×10^{-5}
0.092	302.86	295.64	302.19	-4.78	-14.53	-1.3×10^{-7}	1.4×10^{-6}
0.168	302.43	294.57	301.11	-5.23	-14.38	-1.2×10^{-6}	6.4×10^{-6}
0.184	303.19	296.26	301.91	0.11	-2.23	-1.6×10^{-8}	7.2×10^{-8}
0.207	303.48	296.51	302.02	1.67	-0.56	2.3×10^{-7}	-9.1×10^{-7}

In this construction, rather than laying down a canopy, plants in plastic containers were buried one at a time, disturbing both soil and canopy temperatures, and which is reflected in the much higher rates of the differential coefficients. Nevertheless, Table (3) shows high closure rates as before, using known values of the differential coefficients.

3.4.2 View angle implementation.

Varying the view angle of the sensor induces a fractional vegetation change, Δf_θ , on a static canopy, even with small angle differences, as demonstrated in Figure (8) and Table (4). Also, centering the lens angle on the same point for each angle, presents sampling problems in that some plants disappear from view, and others appear, as the view angle changes (see Appendix (E)). For a large

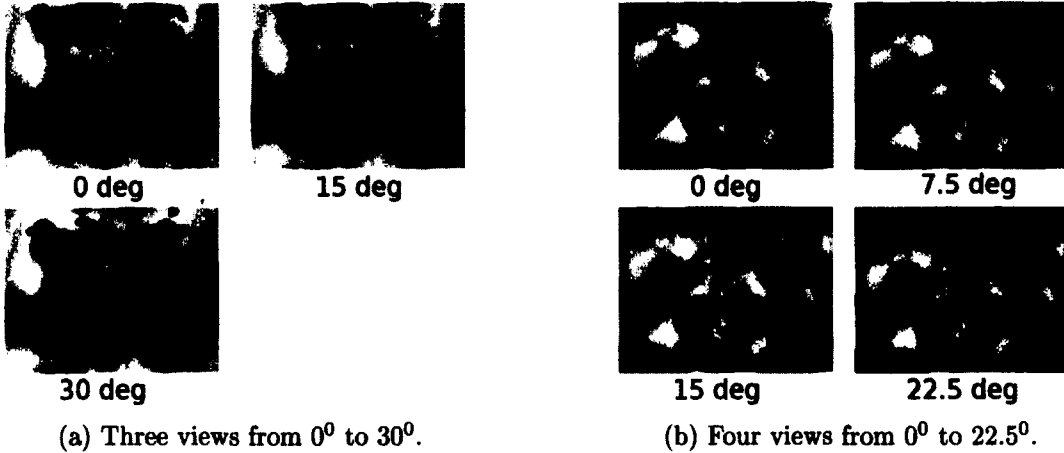


Figure 8: Two sets of thermal infrared images at different view angles, using *Viola Wittrockiana*.

homogeneous canopy distribution this should not be problematic, but for these simulated canopies the boundary of the container is quickly brought into the sample scene as the view angle increases. For this reason, the view angle range is limited to $(0^\circ - 30^\circ)$ in this laboratory setting.

The set of images shown in Figure (8)(a) vary by 15° and the results using Systems (23) are shown in Table 4, with similar closure values as before. Likewise, the set of images shown in Figure (8)(b) vary by 7.5° and the results are also shown in Table 4.

In summary, the discrete quartic System (23) works well within these laboratory simulations, given the known differential coefficients $\frac{\Delta T_s}{\Delta f_\theta}$ and $\frac{\Delta T_v}{\Delta f_\theta}$. In fact, implementing real data gives better results than when using the synthetic data, shown in Table (1), *by orders of magnitude*, for reasons that probably have to do with the mean value uncertainties, as discussed above. However, using the

Table 4: Residual results, δT , for the quartic Systems (23) using data depicted in Figure 8(a) and (b).

% cov (f_θ)	T_s (K°)	T_v (K°)	T_m (K°)	$\frac{\Delta T_s}{\Delta f_\theta}$	$\frac{\Delta T_v}{\Delta f_\theta}$	δT_s	δT_v
0.293	301.81	295.00	299.80				
0.351	301.46	294.35	298.96	-6.04	-11.30	-1.3×10^{-5}	2.5×10^{-5}
0.380	301.29	293.95	298.50	-5.97	-12.08	-2.6×10^{-5}	4.4×10^{-5}

Results for data in Figure 8(a).

% cov (f_θ)	T_s (K°)	T_v (K°)	T_m (K°)	$\frac{\Delta T_s}{\Delta f_\theta}$	$\frac{\Delta T_v}{\Delta f_\theta}$	δT_s	δT_v
0.341	301.56	294.88	299.27				
0.362	301.38	294.74	298.97	-8.08	-6.57	-8.8×10^{-7}	1.6×10^{-6}
0.392	301.22	294.63	298.63	-6.39	-4.76	-3.1×10^{-6}	4.9×10^{-6}
0.406	301.20	294.71	298.55	-5.42	-2.59	-4.9×10^{-6}	7.3×10^{-6}

Results for data in Figure 8(b).

synthetic data exercises parameters beyond those found in this study's field experimental trials, both in fractional differences and rates of change. This gives a very acceptable lower bound for cover residual values of about $10^{-3}{}^\circ C$.

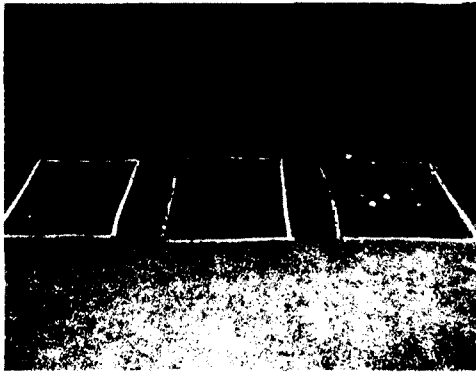
4 METHODS and RESULTS (Part II)

The above Chapter (3) describes this study's computational methods and results used in synthetic and laboratory settings. This chapter describes the auxiliary methods, effects, and results when extending these methods into an outside environment. This field extension also addresses a time delay between data points. Integral to this field-temporal extension is the estimation of the differential coefficients necessary to factor in the environmental influences during the time delay between acquiring data points. Methods used to characterize the differential coefficients for predictive estimations are presented along with the results when using known vegetation cover fractions. Later, methods and results are presented to estimate vegetation fractional cover to fully emulate a mixed pixel application.

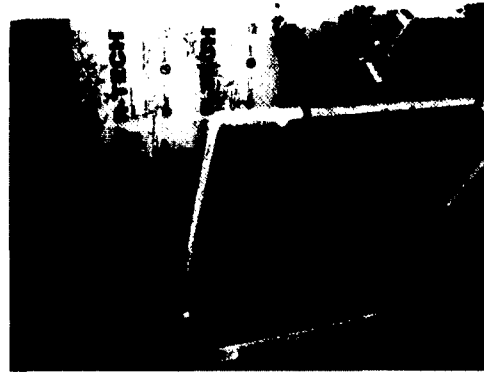
4.1 Field setup.

Field sampling took place in Santa Fe, New Mexico, at an altitude of about 2168 meters, during the summer of 2012. Three beds of marigold plants, *Tagetes erecta*, were constructed to hold different geometries of canopies. The spacing between the stem of the plants was similar in all beds, at about eighteen centimeters apart, staggered between rows. The average size of plants, which roughly resemble a sphere on a stick, varied from bed to bed. The left-most bed in Figure (9)a had plants averaging about six centimeters tall, the middle bed had plants averaging about twelve centimeters tall and the right-most bed had an

average height of about twenty-four centimeters.



(a) Beds with varying canopy geometries.



(b) Acquisition station.

Figure 9: Marigold beds and acquisition station.

4.1.1 Variable parameter clamping.

Several tactics were used during the sampling process to clamp down on environmental effects which would contribute to experimental error and confusion. Restricting the ranges of certain variables can lead to a better understanding of a model by minimizing the effect that one variable has on other variables.

Each bed was surrounded by water resistant thermal insulation to minimize variation in moisture and temperature at the bed boundary. To optimize plant health, potting soil suitable for marigolds was used in the beds, however, the soil was too dark for accurate NDVI ratio readings of near-infrared and red bands³³. Moreover, the speckles of white perlite in the potting soil interfered as artifacts in the image segmentation of plant canopy from soil by falsely registering as canopy.

³³This is probably due to the absorption capacity of very dark soil where any reflection of shortwave radiation is in the noise level of the sensor, giving widely varying values of ratio *nir/red*.

Covering the potting soil with surrounding local soil to a depth of about three centimeters thick made the NDVI signal much more responsive and the cover segmentation better behaved, with less artifact contribution from the soil. On the evenings before sampling, the beds were watered to field capacity at dusk in order to provide a constant water supply to the plants throughout the following day. All flowers on the plants were clipped and debris on the soil surface was removed before sampling.

A key tactic used for this study was to remove direct sunlight as an environmental component so that sampling occurred under shaded conditions. This is because the proposed model is based on a binary land cover and not on a quaternary model of sunlight canopy/soil and shaded canopy/soil, discussed in Section (1.3). A cloth canopy was used to shade the beds and side barriers were constructed from highly reflective material to block strong side thermal insolation, and, as an added clamped parameter, to block the wind. Likewise, a sheet of thermal insulation was placed next to a nearby wall to block its thermal emissions. However, a slight to moderate directional thermal radiation was still noticeable, including shading, mostly in the morning and late afternoon samples. It was not possible to eliminate the full wind effects either, as the plants needed to interact with the atmosphere.

The goal of these restrictions is to have a diffuse radiation environment and to limit the aerodynamic effects to just air temperature, air pressure, relative

humidity and a slight wind, in an attempt to simplify environmental contributions.

4.1.2 Signal acquisition equipment.

The acquisition setup is shown in Figure (9)b. A pivoting stand, with fixed intervals of seven and a half degrees, holds the infrared and NDVI cameras, side by side, at 1.4m height in nadir position. The infrared camera used is the same as described in Section (3.4).

To capture NDVI data, an Agricultural Digital Camera (ADC) from Dycam Incorporated (Woodland Hills, California) was used. It has a 469x365 pixel resolution with a red band response between 0.60 – 0.75 μm and a near-infrared band response between 0.75 – 1.05 μm . A red filter (Wratten 29) is used to block wavelengths below 0.60 μm . The 8.5 mm lens has an f-stop of 4.5, allowing it to focus from 1 m to infinity.

Temperature and relative humidity data were collected by a HOBO U12-013 Data Logger from Onset Computer Corporation (Cape Cod, Massachusetts). The HOBO unit has an operating temperature range of -20° to 70°C with a resolution of 0.03°C at 25°C and an accuracy of $\pm 0.35^{\circ}\text{C}$ between 0° to 50°C . The relative humidity operating range is 5% to 95% with a resolution of 0.03% and an accuracy of $\pm 3.5\%$. The unit was set at 30cm above the ground. Barometric data was taken from the Santa Fe Airport weather station and is expressed in terms of standard temperature and pressure with a sensor resolution of 0.1 millibar. The

horizontal distance from this sensor was 15.5km and the sensor was 234m lower than the field plots.

4.1.3 Sampling issues.

Preliminary exercising of the infrared sensor showed that the bed with the smallest plants was unsuitable for this study due to the lack of thermal contrast exhibited for most of the day. This is likely due to the near proximity to the soil and boundary layer interactions. The other beds, the 12cm and 24cm tall beds, did not share this problem; however, the 24cm bed had consistent problems with the NDVI sensor giving large artifacts, or blooming spots, which are thought to come from the denser canopy not allowing a proper *nir/red* ratio, similar to the problem described above with dark soil. This study uses data from both the 12cm and 24cm beds, except when using NDVI indexing to the vegetation fraction, where only the 12cm bed is used.

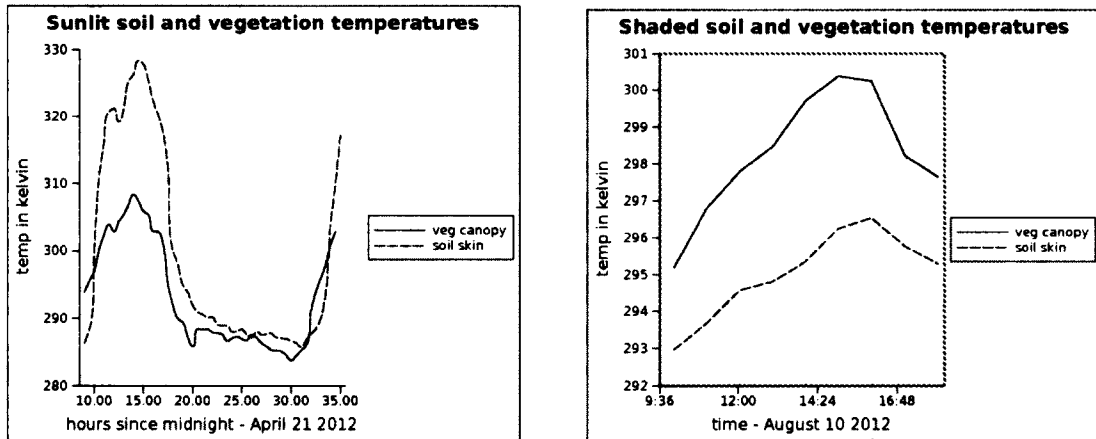
On 12/08/08 sampling did not occur until noon, and two oblique data points at 1200hrs and 1300hrs were not usable due to background artifacts confusing the cover segmentation, so valid samples for the near instantaneous data set did not begin until 1400hrs . However, the nadir views were good and were used in subsequent time delay sets.

For samples days of 12/08/15 and 12/08/16 two data points, instead of one, were taken for the oblique angle of a sample. This was done for comparison

purposes for near instantaneous sampling and only one set of oblique angles per day is used in the field study.

4.1.4 Sampling times.

Land cover temperature data were collected throughout the day of April 21, 2012, for a preliminary analysis, shown below in Figure (10)a. A nadir sample was taken with the infrared camera every half-hour over a twenty-four hour period. For night sampling, the land cover temperatures were separated using a thresholding method and the average temperature reported, as in Section 3.2. For sunlit sampling, the four land covers³⁴ were sampled manually and averaged into soil and vegetation components.



(a) Sunlit land cover temperature response.

(b) Shaded land cover temperature response.

Figure 10: Sunlit and shaded and cover temperature samples.

Figure (10)a shows the signal response in both land covers of sunlight, and later lack of, with steep slopes and near convergence at night, especially right

³⁴The covers being sunlit soil and vegetation, and shaded soil and vegetation.

before dawn. After this time the sun rises, illuminating the land covers, and the vegetation cover temperature leaps ahead of the soil, likely due to the difference in heat capacities and radiation absorptions of plant canopy to that of soil. This effect can also be seen at the end of the day, with the vegetation cover responding quicker to the lack of sunlight than the soil cover. Interestingly, the land cover temperatures cross again at mid-morning, indicating that, for sunlit sampling, the researcher/engineer would want to be aware of these crossovers when sampling.

In contrast, for shaded conditions, the signal response for the day component is reversed with the plant cover temperature being higher than that of the soil cover temperature, as shown in Figure (10)b. The land cover temperatures for Figure (10)b were determined through thresholding segmentation, as above. Implementing swapped cover temperature positions using synthetic images showed that the computational approach used in this study is invariant to either case.

For the field study, samples were taken over four days in August of 2012, from 12/08/08 to 12/08/10 and on 12/08/16 for the 12cm bed and over five days from 12/08/11 to 12/08/15 for the taller 24cm bed. Sampling began when land cover temperature divergence occurred, usually by mid-morning, and continued on the hour and sometimes on the half hour. Hereafter, a data point is defined as an acquired image and a sample contains two data points.

Acquiring data points every hour allows for a staggered sample rendering throughout the day. For example, a nadir data point at 1100hrs can be used with

an oblique data point at 1500hrs to make a time-delayed sample. So, for the 12cm bed, a total of 168 thermal samples with two data points each are used per run, where a run consists of exercising new parameters in the computer processing. Aside from much preparatory work, about 35 runs per bed are represented in this study. Twice as many data points were used for the NDVI runs on the 12cm bed. The 24cm bed total number of samples is 192. On rare occasions, if a sample would not converge in the Newton-Raphson iteration, described in the previous chapter, the sample was ignored.

4.1.5 Sampling views.

An oblique view of approximately fifty-two degrees was chosen for several reasons. The first reason comes from the preliminary study described in Appendix (E), showing that the area increase is fairly linear up to about fifty-two degrees before it hits an exponential growth. This upper bound also corresponds with the practical limitations of the small bed size, such that angles beyond this bound included areas outside of the bed. A preliminary study also showed that the differential coefficient values were more consistent when data points were taken between forty-five and fifty-two degrees rather than with more shallow values. Another reason is that the ATSR platforms also used fifty-two degrees as the oblique angle and so validates its use. All oblique data points used fifty-two degrees, except for one due to operator error, which used forty-five degrees but

did not show adverse effects.

Both nadir and oblique views centered on the top of the same plant. The effective field-of-view was about $38 \times 26 \text{ cm}$ for the nadir view and about $38 \times 60 \text{ cm}$ for the oblique view. It is important to note that while the nadir view gives data for the top of the plant canopy, an oblique view will give data for the top *and* side of the plant canopy, including potential thermal gradients from the ground up. Standard deviations of the cover temperature data points averaged about 0.5°C for the soil and about 0.8°C for the vegetation. The emissivities values used were 0.98 and 0.99 for the soil and vegetation covers respectively.

4.2 Image segmentation of land covers.

The data processing used in this study to discern the differential coefficients and the sensed and calculated temperatures for each cover has already been described in Section (3.2). A key component in this processing is to discriminate land covers, from which the differential coefficients can be calculated and later characterized.

Even seemingly well-behaved images can be problematic when trying to accurately discriminate sections of the image. In this study, for example, morning sample images behaved differently than mid-day samples due to different thermal contrasts and natural variability throughout the land covers. To address the variability in image types, many automated segmentation methods were explored³⁵,

³⁵Such as Otsu's thresholding, Canny's edge detection, and even self-organizing neural nets.

but, off-the-shelf, they did not perform well over all the images.

Simple thresholding to segment the two covers was performed manually. It was not perfect, but performed better under these circumstances than automated methods. Thresholds were specified with a resolution of tenths of a degree Celsius and correspond directly to the temperature resolution of the thermal camera. This threshold temperature does not accurately represent the temperature of either cover since, at this point, emissivity values have not yet been assigned.

A sensitivity study on the effects of varying thresholds was conducted. A best estimate threshold, made by the operator, was assigned to each image, for all images from both beds, and the images were processed to obtain sensed and calculated cover temperatures. Two other runs were conducted with the best estimate threshold value modified by $\pm 0.5^{\circ}C$. This emulates the operator making up to five noticeable shifts up and down from what was considered a best estimate. Results showed an effective difference overall of only a few tenths of a degree Celsius, for the sensed and calculated temperatures and their differences. Results presented in this study use the best estimate threshold.

The sensitivity study showed that simple thresholding is robust for this study, but for larger sample runs an automated method should probably be employed. The automated method might also assign a ribbon of pixels centered on the edge of the covers to mask out ambiguous pixels which fade from one cover to

A Bayesian Maximum Likelihood method was not tried but may be suitable for these sets of images.

the other, and do not really represent either cover.

4.3 Differential coefficients characterization.

The previous chapter describes the reduction of the differential coefficients, $\frac{dT_a}{df_\theta}$ and $\frac{dT_v}{df_\theta}$, from a continuous mode to a discrete one, $\frac{\Delta T_a}{\Delta f_\theta}$ and $\frac{\Delta T_v}{\Delta f_\theta}$, necessary for practical application. For the remainder of this study, both modes will be generically referred to in the continuous mode. Moreover, $\frac{dT_\theta}{df_\theta}$ will be used to refer to either land cover's differential coefficient.

This sections describes the methods and results used to characterize the differential coefficient, $\frac{dT_\theta}{df_\theta}$, for both land covers. It is a heuristic and empirical approach, where the differences in weather variables are used to characterize $\frac{dT_\theta}{df_\theta}$ over a day or more. This characterization is exercised later, using its own and other day's data to probe its behavior.

Some questions that arise are: 1) can the characterization of one day be applied to other days? 2) can a composite of days smooth out the component values, leading to a generalization? and, 3) to what extent are missing variables influencing results?

To begin, a zeroth-order approximation for $\frac{dT_\theta}{df_\theta}$ is given below, for near instantaneous sampling, together with the metrics with which the results were measured. Later, a first-order approximation is developed which gives an environmentally influenced version. Finally, Principal Component Analysis (PCA)

methods are used to describe anomalies in the results.

4.3.1 Special case of view effects.

The total derivative of Equation (12), as developed in Section (2.6), defines the land cover differential coefficient as,

$$\frac{dT_o}{df_\theta} = \frac{\partial T_o}{\partial f_\theta} + \frac{\partial T_o}{\partial T_a} \frac{dT_a}{df_\theta} + \frac{\partial T_o}{\partial R_n} \frac{dR_n}{df_\theta} + \frac{\partial T_o}{\partial R_h} \frac{dR_h}{df_\theta} + \frac{\partial T_o}{\partial V_w} \frac{dV_w}{df_\theta} + \frac{\partial T_o}{\partial P_a} \frac{dP_a}{df_\theta} + \dots \quad (24)$$

where the subscript o denotes either soil or vegetation cover. The partial differential term, $\frac{\partial T_o}{\partial f_\theta}$, is proposed to be the view effect component, with the remaining terms encapsulating the environmental contributions to the total derivative, $\frac{dT_o}{df_\theta}$, and are addressed in a generalized form below in Section (4.3.2).

Since the field approach in this study made efforts to minimize environmental components, described in Section (4.1.1), the above Equation (24) reduces to

$$\frac{dT_o}{df_\theta} = \frac{\partial T_o}{\partial f_\theta} + \frac{\partial T_o}{\partial T_a} \frac{dT_a}{df_\theta} + \frac{\partial T_o}{\partial R_h} \frac{dR_h}{df_\theta} + \frac{\partial T_o}{\partial P_a} \frac{dP_a}{df_\theta} \quad (25)$$

and, for the “instantaneous” sampling, the equation is further reduced to $\frac{dT_o}{df_\theta} = \frac{\partial T_o}{\partial f_\theta}$ because the environment changes, (eg. $dT_a \approx \Delta T_a$) are negligible and so the environmentally influenced terms are set to zero. In this study, the time difference for “instantaneous” sampling is about a minute or two where environmental differences can still be registered but appear as acceptable noise with a small range,

or experimental error, as demonstrated below.

Table (43), in Appendix (N), shows the differential coefficients, $\frac{dT_s}{df_\theta}$ and $\frac{dT_v}{df_\theta}$, of the 12cm bed, over different time intervals. The bottom of the “Near Instantaneous” column gives the averages of the differential coefficients as $\frac{dT_v}{df_\theta} = 0.212$ and $\frac{dT_s}{df_\theta} = 1.577$. Applying these averaged values in the “unmix” computer program³⁶ to all of the near instantaneous samples gives an average temperature difference between sensed and calculated temperatures of $\Delta T_{v_{avg}} = 0.007^\circ C$ and $\Delta T_{s_{avg}} = 0.005^\circ C$ with standard deviations of $std_v = 0.610^\circ C$ and $std_s = 0.435^\circ C$ respectively. The terms, $\Delta T_{v_{avg}}$ and $\Delta T_{s_{avg}}$, are actually the bias of the system, expressed as the mean of differences and is a measure of accuracy, while the standard deviations are a measure of precision.

The goal of this study is to separate out the binary land cover temperatures from the sensed mixed pixel in a bid for more accurate temperature estimation. The above bias and precision seem a reasonable outcome for exercising the instantaneous samples with the view effect component, but the question arises: How does this method compare to the mixed temperature, especially when the dynamic range of land cover temperature differences is low under shaded conditions? Put forth another way: How much closer is the computed cover temperature to the sensed cover temperature than the mixed temperature is to the sensed cover

³⁶Described in Section (3.4). The unmix program has command line options to specify the values of $\frac{dT_s}{df_\theta}$ and $\frac{dT_v}{df_\theta}$.

temperature?

A sample-by-sample comparison is given for both covers of the 12 *cm* bed in the tables of Appendix (F.1). The calculated temperature differences are compared to the mixed temperature differences, as posed in the last question in the above paragraph, and the performance is reported on the two right most columns. The second most right column, “ a/b ”, gives a proportional measurement of how much closer the calculated temperature is to the sensed temperature than is the mixed temperature. The furthest right column simply reports if it was closer and is assigned a “hit” value of one. The bottom of that column shows the percentage of sample points which outperformed the mixed temperature difference.

Similar calculations for the view effect were made for the 24 *cm* bed and result tables can be found in Appendix (G.1). Table (5), below, summarizes the results of applying the respective averaged differential coefficients of both beds to the near instantaneous samples. The response columns indicate the precision, or the Gaussian spread of the difference from the calculated to sensed temperatures, with the label “std”. Likewise, the accuracy is indicated by the label “bias”. The “% better” column shows the percentage of points that the calculated temperatures outperformed the mixed temperature. The results are encouraging.

It is important to note that the 12 *cm* bed has less vegetation cover, with mean values of $f_{\theta_{nadir}} = 0.219$ and $f_{\theta_{oblique}} = 0.418$, than does the 24 *cm* bed, with mean values of $f_{\theta_{nadir}} = 0.485$ and $f_{\theta_{oblique}} = 0.716$. This gives an opportunity for

bed	# smpl	# days	$\frac{dT_s}{df_a}$	$\frac{dT_v}{df_a}$	veg response			soil response		
					std C	bias C	% better	std C	bias C	% better
12 cm	34	4	1.577	0.212	0.610	0.007	91.2	0.435	0.005	91.2
24 cm	41	5	2.230	0.825	0.316	-0.007	100.0	0.803	-0.003	100.0

Table 5: Near-instantaneous results using averaged $\frac{dT_s}{df_a}$ and $\frac{dT_v}{df_a}$.

comparing behavior between the two beds. For example, in Table (5) a transpose in precision is observed, in that the sparser cover has a slightly larger vegetation spread than the soil does and this is reversed for the more densely covered bed.

Table (6), below, shows the cover responses for the near instantaneous samples when $\frac{dT_v}{df_a}$ and $\frac{dT_s}{df_a}$ are set to zero, rather than using averaged values. The effect is to raise the bias by orders of magnitude for both beds while the precision stays about the same. It also reduced the overall performance metric for the 24 cm bed, as expected. Curiously, the overall metric improved for the 12 cm bed, but when the individual samples were compared with the previous run, using view effect values, the results showed that this run had more cover temperatures closer to the mixed temperature, and with just one more point qualifying. The previous run had many more points closer to the sensed temperature, but missed that extra point by just 2/100th of a degree.

bed	# smpl	# days	$\frac{dT_s}{df_a}$	$\frac{dT_v}{df_a}$	veg response			soil response		
					std C	bias C	% better	std C	bias C	% better
12 cm	34	4	0.000	0.000	0.594	0.715	94.1	0.439	-0.534	94.1
24 cm	41	5	0.000	0.000	0.312	0.415	95.1	0.818	-1.131	95.1

Table 6: Near-instantaneous results using $\frac{dT_s}{df_a} = 0$ and $\frac{dT_v}{df_a} = 0$.

Another way to express the proportional closeness of calculated and mixed temperatures to the sensed temperature, is to use a decibel, $dB = 10\text{Log}_{10}(a/b)$, representation. This logarithmic rendering gives a compact sense of the dynamic range of the closeness measure. Figure (11) shows the frequency distribution of the proportional closeness of the above runs, with and without view effects, and allows for a comparison. Both histograms used the same bin spacing.

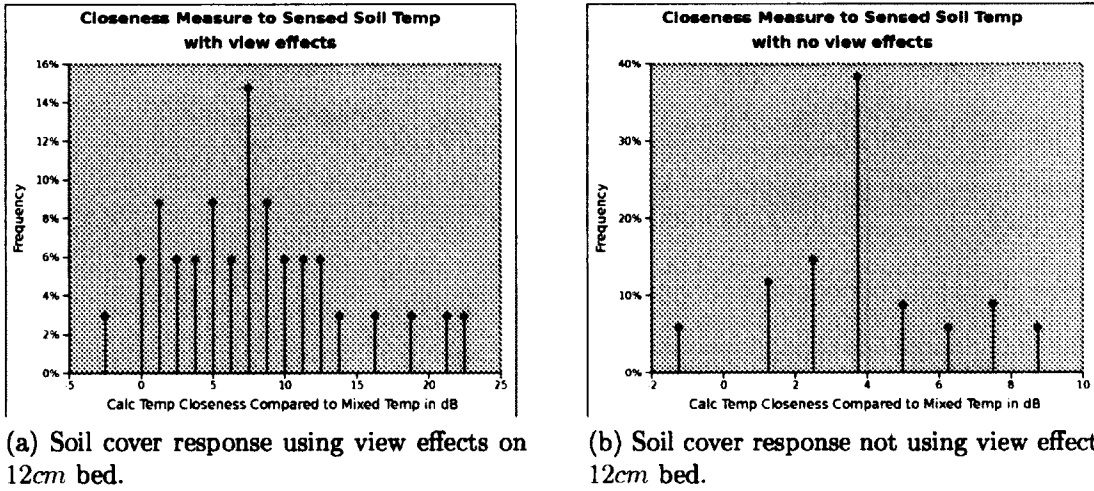


Figure 11: Power decibel representation of closeness to sensed soil temperature.

Figure (11)b shows the results of setting the coefficients to $\frac{dT_v}{df_\theta} = 0$ and $\frac{dT_s}{df_\theta} = 0$ (no view effects), with about forty percent registering a little over twice the closeness for the calculated temperature than the mixed temperature was to the sensed temperature. Maximum closeness was about eight times ($a/b = 10^{0.9}$) closer. Figure (11)a shows the results of using the averaged values of $\frac{dT_v}{df_\theta}$ and $\frac{dT_s}{df_\theta}$ (with view effects). The dynamic range has increased over ten times and twenty-eight percent of the calculated temperatures are ten times closer to the sensed

temperatures than is the mixed temperature.

When using the “better than” system, in the data runs throughout this study, typical misses are just by tenths of a degree, even with high hit rates, where the majority of points are orders of magnitude closer to the sensed temperature, proportionally, than is the mixed temperature. A decibel system expresses this dynamic range well, however the “better than” frequency system is used in this study because it is more intuitive.

Stepping back in scale, either set of the above results is quite acceptable for practical purposes and gives substance to previous studies which set these coefficients to zero for near instantaneous sampling. Nevertheless, implementing the view effect in this study shows a higher level of accuracy than when not implementing it, as shown in Table (6). A decibel representation also showed that many more calculated temperatures were significantly closer to the sensed temperature when using the view effects.

4.3.2 Generalizing by correlating differential coefficients to weather.

The previous section shows that the view effect component, expressed as the partial differential $\frac{\partial T_o}{\partial f_\theta}$, is just a zeroth-order approximation of Equation (24) that works well for near instantaneous sampling and that it is a function of canopy geometry and view angle, since environmental influences can be ignored. This allows the characterization of the canopy so that view effects can be derived and

used thereafter, as long as the canopy geometry and sensor angles remain constant. The task now is to extend the characterization to the truncated environmental components of Equation (25) as a first-order approximation. This section outlines the methods used to extend the characterization and gives an analysis.

Inclusive of near instantaneous sampling, this study now considers samples with two data points separated in time, throughout the day. The staggered sampling procedure is explained in Section (4.1.4). It is clear that a time delay between data points introduces environmental influences which are complex and inter-related. However, these influences are reflected by the environmental components on the right hand side of Equation (24), and do not consider time as a factor. Recognizing that accounting for all environmental components in a general way is ambitious, this study has narrowed its focus experimentally to just three variables, ΔT_a , ΔR_h and ΔP_a , and seeks a function to express $\frac{dT_a}{df_\theta}$, as in Equation (25). Because of this limitation and for practical reasons, this study also narrows its scope to a more local sense, rather than to strive for a complete generalization. This study's definition of local scope is on the order of days extending into a week.

The characterization approach for the environmental components is essentially the same as in the special case above, where known values³⁷ can lead to patterns and, for this, a first-order approximation regression analysis is used.

³⁷The reader is reminded that the high resolution data gives known values of cover fraction, known differential coefficients, $\frac{dT_a}{df_\theta}$ and $\frac{dT_h}{df_\theta}$, and known cover temperature distributions from which to form a basis of characterization.

Correlation plots for the beds can be found in Appendix (H) and (I). These plots show the linear regression fits of the differential coefficient, $\frac{dT_o}{df_o}$, to the differences in air temperature, relative humidity and air pressure for each sample day. In general, and as expected, the coefficient of determination, R^2 , is strongest with the air temperature difference, followed by relative humidity and air pressure differences.

First approximations for $\frac{dT_o}{df_o}$ were made using a linear regression fit to just air temperature differences, ΔT_a . Using this approximation in the unmix computer program gave unsatisfactory results when comparing calculated cover temperatures to sensed cover temperatures, although these values were not entirely hopeless. A review of $\frac{dT_o}{df_o}$ correlations with ΔT_a , found in the tables of Appendix (H) and (I), will show mostly high coefficients of determination, R^2 , but not always. The sample data from dates 12/08/08 and 12/08/13 are examples of this, with R^2 values of 0.47 and 0.64, respectively, for the vegetation cover. These same dates also gave $R^2 = 0.65$ and $R^2 = 0.64$, respectively for the soil cover. For other dates, the R^2 values range between 0.72 and 0.94, for both covers. These observations become relevant later when later considering anomalies.

Also recognizing that other weather influences are at play, a second approximation for $\frac{dT_o}{df_o}$ extends the single-variate fit to a bi-variate one by introducing the difference in relative humidity, ΔR_h , as a new variable. This improved the R^2 values for regression fits used in approximating $\frac{dT_o}{df_o}$ and, subsequently, the results. However, higher correlations were limited to particular time delays, such as one,

two, and three hour delays throughout the day. For example, surface fit coefficients for a one hour delay could be used to estimate $\frac{dT_o}{df_o}$ for any one hour delay sample with reasonable cover temperature results, a two hour delay surface coefficient could be used to estimate two hour sample delays, and so on. Example regression surface fits can be seen in the figures of Appendix (K). These figures show a bi-linear surface regression fit for the 12cm bed at different time-delays across all sample days. It is interesting to note the warping effect on the surface induced by the interaction between the ΔT_a , ΔR_h variables (the bottom-left corner of the surface is closest to the reader).

Realizing that this bi-variate approach was too limited and that it was addressing the situation in terms of time, which is not a component in our equations, this study's third approximation for $\frac{dT_o}{df_o}$ now includes a multi-variate fit by introducing the difference in atmospheric pressure, ΔP_a , as a new variable, in a bid to generalize over the entire day. The intent was to see if a hyper-surface set of correlation coefficients can give an estimate to $\frac{dT_o}{df_o}$ for use in any time delay sampling throughout the day, including near instantaneous sampling. For simplicity, the term "surface" will be used hence forth to refer to the hyper-surface generated by the variables ΔT_a , ΔR_h , ΔP_a . Unlike the previous bi-variate, bi-linear surface fit, this multi-variate fit is strictly linear, as experimental comparisons showed little difference in results between the linear and bi-linear correlation surface fits.

Table (7), below, shows the effects of progressively including variables to

the daily regression fit, as expressed in R^2 , for both covers and both beds. In general, adding either variables, ΔR_h or ΔP_a , to make a bi-variate surface with ΔT_a apparently strengthens the R^2 value. In some examples, these influences seem minimal but when one variable doesn't seem to influence a better R^2 , the other one will. Using all three variables, ΔT_a , ΔR_h , and ΔP_a , ultimately gives the best R^2 overall and is thus used to present this study's results. Also, both individual day and composite correlation surfaces (described below) have extremely low variable p -values, the probability that the variable null-hypothesis is true.

day	R^2 of vegetation regression fit of $\frac{dT_a}{dJ_a}$				R^2 of soil regression fit of $\frac{dT_a}{dJ_a}$			
	ΔT_a	$\Delta T_a, \Delta R_h$	$\Delta T_a, \Delta P_a$	$\Delta T_a, \Delta R_h, \Delta P_a$	ΔT_a	$\Delta T_a, \Delta R_h$	$\Delta T_a, \Delta P_a$	$\Delta T_a, \Delta R_h, \Delta P_a$
120808	0.467	0.467	0.625	0.803	0.653	0.788	0.654	0.896
120809	0.904	0.955	0.919	0.974	0.771	0.775	0.960	0.969
120810	0.894	0.907	0.946	0.962	0.763	0.772	0.945	0.960
120816	0.725	0.775	0.804	0.867	0.915	0.916	0.925	0.925
all	0.834	0.834	0.886	0.890	0.737	0.794	0.788	0.902

(a) 12 cm correlation responses.

day	R^2 of vegetation regression fit of $\frac{dT_a}{dJ_a}$				R^2 of soil regression fit of $\frac{dT_a}{dJ_a}$			
	ΔT_a	$\Delta T_a, \Delta R_h$	$\Delta T_a, \Delta P_a$	$\Delta T_a, \Delta R_h, \Delta P_a$	ΔT_a	$\Delta T_a, \Delta R_h$	$\Delta T_a, \Delta P_a$	$\Delta T_a, \Delta R_h, \Delta P_a$
120811	0.883	0.899	0.913	0.916	0.873	0.902	0.924	0.926
120812	0.944	0.949	0.946	0.949	0.898	0.906	0.898	0.914
120813	0.859	0.869	0.880	0.881	0.641	0.751	0.849	0.866
120814	0.858	0.859	0.916	0.934	0.813	0.821	0.912	0.927
120815	0.920	0.969	0.988	0.988	0.643	0.949	0.927	0.967
all	0.874	0.874	0.895	0.901	0.803	0.804	0.882	0.888

(b) 24 cm correlation responses.

Table 7: Differential coefficient correlation R^2 values as environmental variables are progressively included.

Tables (8) and (9), below, show day-by-day surface correlation coefficients

and corresponding R^2 values for all staggered and near instantaneous samples for both covers and beds. To the right of the surface coefficients, results can be found from using each day's surface coefficients to estimate the differential coefficient, $\frac{dT_o}{df_\theta}$, on its own data with known cover fractions. As in the near instantaneous case, the results are measured by the standard deviation (precision), bias (accuracy) and if the calculated temperature was closer to the sensed temperature than was the mixed temperature. This initial feasibility test shows reasonable results when using a day's surface coefficients to estimate that day's differential coefficient. If, by some manner, daily surface coefficients were known then this implementation and its results would be considered operationally successful. That is, it could deliver calculated temperatures that performed better than mixed temperature with a hit rate of about nine times out of ten, for any time delay between samples, from mid-morning to late afternoon.

The next task is to see how sensitive the results are to combined and averaged surface fit coefficients. A combined surface fit means that all sample points across all sample days, per bed, are used to generate the surface fit needed to estimate $\frac{dT_o}{df_\theta}$. However, not all days have the same number of samples and so the combined surface can be skewed by those days with more sample points. Averaging surface fit coefficients across the days attempts to neutralize this effect.

day	intrcpt	ΔT_a	ΔR_h	ΔP_a	R^2	stdev C	bias C	# smpl	% better
120808	-0.993	2.319	1.067	-4.897	0.803	0.824	-0.003	33	87.9
120809	2.522	6.571	1.226	-1.196	0.974	0.523	-0.003	45	100.0
120810	0.116	4.246	0.639	-1.479	0.962	0.512	0.000	45	97.8
120816	-1.404	3.873	0.788	-3.275	0.867	0.617	0.001	45	100.0

(a) Vegetation cover response using day-by-day surface fit.

day	intrcpt	ΔT_a	ΔR_h	ΔP_a	R^2	stdev C	bias C	# smpl	% better
120808	0.621	2.504	1.348	-3.010	0.896	0.568	0.008	33	87.9
120809	1.705	1.951	0.242	-1.917	0.969	0.390	-0.003	45	100.0
120810	1.889	2.288	0.372	-1.639	0.960	0.452	0.004	45	97.8
120816	0.866	3.383	-0.014	-0.830	0.925	0.449	0.007	45	100.0

(b) Soil cover response using day-by-day surface fit.

Table 8: Unmixing results using estimated differential coefficients, $\frac{dT_s}{df_\theta}$ and $\frac{dT_v}{df_\theta}$, from daily weather fit for 12cm bed.

day	intrcpt	ΔT_a	ΔR_h	ΔP_a	R^2	stdev C	bias C	# smpl	% better
120811	1.225	4.258	0.900	-2.435	0.915	0.421	0.010	28	100.0
120812	1.586	3.730	-0.563	0.213	0.949	0.591	-0.015	45	91.1
120813	0.643	6.146	0.178	-0.787	0.881	0.322	-0.006	36	100.0
120814	1.315	3.573	0.905	-3.393	0.934	0.444	0.009	55	92.7
120815	0.305	2.591	-0.069	-1.524	0.988	0.126	-0.001	28	100.0

(a) Vegetation cover response using day-by-day surface fit.

day	intrcpt	ΔT_a	ΔR_h	ΔP_a	R^2	stdev C	bias C	# smpl	% better
120811	2.901	1.836	0.388	-1.320	0.925	1.217	0.014	28	100.0
120812	2.824	2.993	0.625	-1.078	0.914	1.355	-0.011	45	91.1
120813	2.347	2.847	0.412	-1.378	0.866	0.801	-0.002	36	100.0
120814	2.016	2.258	0.610	-3.034	0.927	1.337	-0.020	55	92.7
120815	2.008	-0.153	-0.597	-0.830	0.967	0.343	0.000	28	100.0

(b) Soil cover response using day-by-day surface fit.

Table 9: Unmixing results using estimated differential coefficients, $\frac{dT_s}{df_\theta}$ and $\frac{dT_v}{df_\theta}$, from daily weather fit for 24cm bed.

Both combined and averaged correlation surfaces will be presented for comparison.

Tables (10) and (11), below, show the results of applying combined and averaged correlation surfaces of all days *to* all days for both beds. While bias values have increased somewhat, the results give hit-rates between eighty and one-hundred percent, excluding sample day 12/08/08, which will be addressed in the next sub-section. Out of thirty-two cover points, four cover points are in the 100% category, twenty in the 90%, and eight in the 80% range. Tables (18)(19) and (31)(32) in Appendix (F.1) and (G.1), respectively, give a better sense of how the method performs overall.

Different surface combinations and averages were applied to the sample days to exercise the behavior of the cover temperature responses to different estimations of $\frac{dT_c}{df_\theta}$. Compilation of the results are given in Appendix (F.2) and (G.2) for both beds.

For the 12cm bed, Tables (20)-(22) in Appendix (F.2) show results of applying a correlation surface of 12/08/08 mixed separately with dates 12/08/09, 12/08/10, and 12/08/16 to other dates. Surprisingly (because 12/08/08 results behave differently) the outcome shows a good performance when applied to other days for the combined surface, but less so for the averaged surface. To note, the combined surface scheme is likely to behave better than the averaged scheme

	type	intrcpt	ΔT_a	ΔR_h	ΔP_a	R^2
veg fit	combined	0.219	3.714	0.184	-1.864	0.890
	averaged	0.060	4.252	0.930	-2.712	
soil fit	combined	1.254	3.023	0.660	-1.829	0.902
	averaged	1.270	2.531	0.487	-1.849	

(a) Combined and averaged surface fit coefficients.

day	veg response			soil response		
	std C	bias C	%	std C	bias C	%
120808	1.283	-0.282	54.6	0.890	0.196	54.6
120809	0.532	0.468	95.6	0.405	-0.353	95.6
120810	0.651	-0.045	95.6	0.605	0.044	95.6
120816	0.882	-0.223	93.3	0.636	0.190	91.1

(b) Cover responses using combined surface fit.

day	veg response			soil response		
	std C	bias C	%	std C	bias C	%
120808	1.271	-0.491	54.5	0.880	0.342	54.5
120809	0.653	0.594	95.6	0.497	-0.453	95.6
120810	0.615	-0.103	97.8	0.556	0.088	97.8
120816	0.994	-0.104	91.1	0.711	0.107	91.1

(c) Cover responses using averaged surface fit.

Table 10: Unmixing results using estimated differential coefficients, $\frac{dT_s}{df_\theta}$ and $\frac{dT_v}{df_\theta}$, from combined and averaged surface fits of all days for 12cm bed.

	type	intrcpt	ΔT_a	ΔR_h	ΔP_a	R^2
veg fit	combined	1.195	3.965	0.408	-1.722	0.901
	averaged	1.107	3.323	-0.082	-1.356	
soil fit	combined	2.202	2.003	0.241	-1.761	0.888
	averaged	2.419	1.956	0.287	-1.528	

(a) Combined surface fit coefficients.

day	veg response			soil response			day	veg response			soil response		
	std C	bias C	%	std C	bias C	%		std C	bias C	%	std C	bias C	%
120811	0.458	-0.109	96.4	1.354	0.356	96.4	120811	0.459	-0.102	96.4	1.360	0.338	96.4
120812	0.826	0.073	84.4	1.779	-0.145	82.2	120812	0.790	0.073	88.9	1.708	-0.147	88.9
120813	0.391	0.017	100.0	0.994	-0.017	100.0	120813	0.386	0.051	100.0	0.964	-0.113	100.0
120814	0.540	-0.011	87.0	1.631	0.000	83.3	120814	0.556	-0.009	85.2	1.684	-0.014	85.2
120815	0.300	0.026	96.4	0.807	-0.054	96.4	120815	0.344	0.070	96.4	0.919	-0.164	96.4

(b) Cover responses using combined surface fit. (c) Cover responses using averaged surface fit.

Table 11: Unmixing results using estimated differential coefficients from combined and averaged surface fits of all days for 24cm bed.

for the mixtures of 12/08/09, 12/08/10, and 12/08/16 because these sample dates have the same number of samples. However, for the 24cm bed, an averaged surface gives better results.

Tables (23)-(25) in Appendix (F.2) show results of different surface mixtures for the 12cm bed, not including 12/08/08, as applied to the sample dates. These surface fit composites performed very well on other days. For example, using surface fit dates 12/08/09 and 12/08/16 as predictor for 12/08/10 results in a hit rate of 95.6% for both covers. Likewise, using dates 12/08/10 and 12/08/16 as predictor for 12/08/09 gives a hit rate of 97.8% for the vegetation cover and 95.6% for the soil cover. Finally, using 12/08/09 and 12/08/10 as predictor to 12/08/16, *a week apart*, gives a hit rate of 93.3% for both covers. Averaging results for these combinations gives a hit rate of 95.6% for the vegetation cover and 94.8% for the soil cover.

Continuing to exercise correlation surface fit behavior, for the 12cm bed, Table (26) in Appendix (F.3) shows the results of applying individual date surface fits to the other dates. As expected, using the correlation surface fit from 12/08/08 gave poor performance when applied to the other dates. Excluding 12/08/08 and using the individual surface fits of 12/08/09 and 12/08/10 on other dates gave high hit rates as before. Interestingly, the surface fit from 12/08/16 did not perform well when applied to dates 12/08/09 and 12/08/10, with respective hit rates of 66.7% and 71.1%, for both covers, indicating that this surface fit exceeded some

bound for reciprocal application. This gives substance for the use of a broader scale mixed surface scheme which has better application performance, even when incorporating a sample date such as 12/08/08.

For the 24cm bed, Tables (33)-(36) in Appendix (G.2) show results of applying a correlation surface fit, composed of two days, applied to other days. Both combined and averaged surface fits responses showed some volatility and degradation in hit rates. Although Tables (35) and (36) show high hit rates, it is clear that that two days mixing of surface fits is not sufficient for confident prediction in this case.

Table (37) shows the results of applying three day surface fit compositions on the remaining days. Overall, using a three day composition surface fit gives better results than a two day composition one. Sub-tables (c) and (d) show a date of 12/08/14a which signifies an adjustment to the data. The data set of 12/08/14 has a troublesome data point at 1000hrs, the first of the day. Removing this data point improves the results by about ten percentage points for that day and means that sampling starts at 1030hrs instead of 1000hrs, for a total of 44 samples over the day. The data point was not removed for surface fits using the 12/08/14 data set.

Table (38) shows the results of applying four day composite surface fit on the remaining day. Average hits rates are 91.5% for the vegetation cover and to 90.6% for the soil cover, when using the 12/08/14a data set. As with the 12cm bed,

hit rate results get better as more days are entered into the surface composition. For completion, Table (39) in Appendix (G.3) shows the result of individual day surface fits applied to the other days. As with the two day composites, this table shows some success but it is not sufficient to get consistently high hit rates.

The above results, excluding data set 12/08/08, show that differential coefficient, $\frac{dT_o}{df_\theta}$, can be related to simple differences in common weather data, specifically ΔT_a , ΔR_h , and ΔP_a , for each land cover. This is accomplished by generating a hyper-plane function, derived from local historical data through regression, to estimate the values of $\frac{dT_o}{df_\theta} \approx \frac{\Delta T_o}{\Delta f_\theta}$.

In summary, the hyper-plane function is generated by a linear regression fit from known data and takes on the form,

$$\frac{\Delta T_o}{\Delta f_\theta} = C_0 + C_1 \Delta T_a + C_2 \Delta R_h + C_3 \Delta P_a$$

where C_0 is the planar intercept and $C_{1,2,3}$ are surface coefficients derived from the correlation surface fits. This equation has the same form as the truncated total derivative,

$$\frac{dT_o}{df_\theta} = \frac{\partial T_o}{\partial f_\theta} + \frac{\partial T_o}{\partial T_a} \frac{dT_a}{df_\theta} + \frac{\partial T_o}{\partial R_h} \frac{dR_h}{df_\theta} + \frac{\partial T_o}{\partial P_a} \frac{dP_a}{df_\theta}$$

A term-by-term association between the two equations gives, $C_0 = \frac{\partial T_o}{\partial f_\theta}$, $C_1 = \frac{\partial T_o}{\partial T_a} \frac{1}{\Delta f_\theta}$, etc., as developed in Section (2.7.2) and shows that the regressive fit is a

first-order approximation of the total derivative, $\frac{dT_o}{df_\theta}$. Verification of this for the view effect, $\frac{\partial T_o}{\partial f_\theta}$, has been shown above as a special case, with near instantaneous examples. In this first-order rendering, the surface intercept, C_0 , and $\frac{\partial T_o}{\partial f_\theta}$ are known for these data and an example is presented in Table (12) below, for the composite surface fit of both beds. A maximum discrepancy of only $0.4^\circ C$ can be seen in both beds, derived from hundreds of sample points for all days. The view effect values, $\frac{\partial T_o}{\partial f_\theta}$, in the table are the same as those used in the special case above and the intercepts, C_0 , are from the composite correlation surface fit of all sample days, per bed. Therefore, from this limited exercise, view effects can be seen as the weather intercepts of the regressive surface fits.

bed	veg		soil		# samples
	$\frac{\partial T_o}{\partial f_\theta}$	C_0	$\frac{\partial T_o}{\partial f_\theta}$	C_0	
12cm	0.21	0.22	1.58	1.25	168
24cm	0.83	1.19	2.23	2.20	192

Table 12: Surface intercept, C_0 , and view effect, $\frac{\partial T_o}{\partial f_\theta}$, comparison.

Not as straight forward, the environmental partial terms can be characterized, but not as discrete versions of the partials. It is tempting to approximate the partial differentials with known differences, such as $\frac{\partial T_o}{\partial T_a} \approx \frac{\Delta T_o}{\Delta T_a}$, etc, so that the above equation looks like,

$$\frac{\Delta T_o}{\Delta f_\theta} = \frac{\partial T_o}{\partial f_\theta} + \frac{\Delta T_o}{\Delta T_a} \frac{\Delta T_a}{\Delta f_\theta} + \frac{\Delta T_o}{\Delta R_h} \frac{\Delta R_h}{\Delta f_\theta} + \frac{\Delta T_o}{\Delta P_a} \frac{\Delta P_a}{\Delta f_\theta}$$

but canceling gives,

$$\frac{\Delta T_o}{\Delta f_\theta} \neq \frac{\partial T_o}{\partial f_\theta} + \frac{\Delta T_o}{\Delta f_\theta} + \frac{\Delta T_o}{\Delta f_\theta} + \frac{\Delta T_o}{\Delta f_\theta}$$

and is ill-posed. Instead, approximate values for the partial differential terms can be gleaned from the expressions $\frac{\partial T_o}{\partial T_a} = C_1 \Delta f_\theta$, etc. These are instantaneous values of the partials at the mean value point in f_θ , and not at the mean value point with respect to the environment variable. Table (13), below, shows the partial values of the vegetation cover differential, $\frac{dT_v}{df_\theta}$, for the 12cm bed.

day	$\frac{\partial T_o}{\partial T_a}$		$\frac{\partial T_o}{\partial R_b}$		$\frac{\partial T_o}{\partial P_a}$		# samples
	avg	stdev	avg	stdev	avg	stdev	
120809	1.320	0.067	0.246	0.013	-0.240	0.012	33
120810	0.917	0.132	0.170	0.024	-0.707	0.102	36
120816	0.744	0.068	0.152	0.014	-0.630	0.058	36

Table 13: Averaged environmental partial differentials for 12cm vegetation cover.

This gives a feel for what the partial term values are doing, but, in effect, they remain coupled to the regression fit coefficients, C_1, C_2, C_3, \dots , etc. The variance from day to day shows that the partial and total derivatives are subject to other influences, not accounted for, and are reflected in the fit coefficients.

Sample days 12/08/08 and 12/08/13 were mentioned above, implying they may be special cases. The results in Table (10) show that sample day 12/08/08 performed poorly with respect to the other days, while in Table (11) sample day 12/08/13 performed at the 100% hit rate. The next subsection will address this variance by using a Principal Component Analysis.

4.3.3 Principal component analysis.

Co-related input variables to a model, as found in weather data, complicate the description of their contributions to the recipient model. This is especially true when related, and unaccounted for, variables do not remain constant and so influence, in a hidden way, the other input variable values, thus compounding the effects on the result.

It is problematic to a model if a sometimes influential variable is not accounted for. In this study it was assumed that other variables were at play, but hoped that they were suppressed sufficiently to give good results, which did happen eight out of nine days. This variable, or variables, expressed itself in the data set of 12/08/08 and not so much in the other days. The most likely factor is wind, but this is speculative since reliable wind data is not available for this study, unfortunately.

Scatterplots of $\frac{dT_a}{df_\theta}$ against each of the variables, $\Delta T_a, \Delta R_h, \Delta P_a$, for all sample days, are given in Appendix (H) and (I) for the 12cm and 24cm beds, respectively. Figure (14) shows the graphs for sample day 12/08/08 and abnormal behavior can be seen when compared to the rest of the sample days. Aside from low R^2 values with respect to ΔT_a and ΔR_h , the main difference is seen in the scatter plots of $(\frac{dT_a}{df_\theta}, \Delta R_h)$, Sub-Figure (b), where the regression line is going in a different direction, with a positive slope, to that of the rest of the sample days

which have a negative slope. Sample days of 12/08/16 and 12/08/13, Figures (17) and (21), also show low R^2 values for scatter plots ($\frac{dT_a}{df_\theta}, \Delta R_h$) but maintain the same direction in the regression lines as the other sample dates. As the previous section showed, the results of both 12/08/16 and 12/08/13 behaved well.

It is well known that air temperature and relative humidity have a strong inverse relationship, but this is not always the case. Figures (25) and (26) in Appendix (J) show scatter plots of $(\Delta T_a, \Delta R_h)$ for all sample days, demonstrating a strong correlation between the two for all but sample date 12/08/08. Here too, a change in direction is noted in the regression line of Figure (25)a, indicating that something is breaking the usual relationship between ΔT_a and ΔR_h . Turbulent wind cells are known to do this and is the likely cause.

Another way to show that sample date 12/08/08 is being influenced differently than the other dates is to use a technique called Principal Component Analysis (PCA). Correlated variables, especially in multi-dimensional space, are better understood if their contributions to the regression surface fit can be projected to a set of orthogonal basis vectors. PCA does this by using a singular value decomposition on the data set to create a set of eigenvectors which serve as the new basis. The first eigenvector is in the direction of the strongest variation, the second eigenvector will be orthogonal to the first and has the second strongest variation, and so on.

Appendix (L) and (M) show PCA graphs for the $\frac{dT_a}{df_\theta}$ correlation surface fits

of the sample days for 12cm and 24cm beds, respectively. The scree plots on the left side show the proportion of variances each orthogonal component contributes to the signal. The biplots on the right side show the data points projected onto the space created by the first two principal components. This gives the best view on how the points are distributed and is called the “score” plot. This projection can also reveal clustering of the points and is used in signal processing to detect patterns. In these plots, there is little clustering on the daily graphs indicating an even distribution of points throughout the data space. The graphs in Figures (33) and (39), show small clusters of data points but also a wide distribution of points.

The vectors shown in the biplot represent the input and dependent variable contributions to the principal components and is called the “load” plot. The loadings on the principal component by each variable vector can be visualized by projecting the vector to the principal component axis. So, a variable vector running horizontally contributes to the first principal component and not to the second principal component. In this PCA transform, variables are scaled since different units are used for each variable.

Figure (29) shows the scree plot and the biplot for sample day 12/08/08. There are two unusual features that are not seen the other graphs. The scree plot, for both covers, gives the second principal component a large percentage of the total variance, unlike most other days. Also, the loading on the biplot gives

the variable vectors all pointing in the same direction with respect to the first principal component, unlike the other days, where the ΔT_a and ΔR_h vectors run in opposite directions. This distinction is similar to the directional difference in the scatter plot of $(\Delta T_a, \Delta R_h)$, shown in Figure (25).

It is interesting to follow the vector behavior of the other biplots. As mentioned earlier, ΔT_a and ΔR_h vectors run generally in opposite directions. Vectors $\frac{dT_a}{df_\theta}$ and ΔT_a usually have small separation in angle, while the ΔP_a vector has a strong angle separation to the rest of the vectors, greatly contributing to the second principal component and to the overall results. Also, clustering that appears in the score plots do so near and perpendicular to the ΔP_a vector. This is probably due to the low time sampling resolution (once an hour) of the barometric sensor. All vectors can change direction with respect to the second component and still not adversely affect results. Indeed, even changing directions in the first principle component, as in Figure (38), does not seem to highly impact results either, as long as the relative angle separation is maintained. Considering these variations in vector alignment, the vector alignment that does not work for this method is that given in sample day 12/08/08 and it is clearly distinct from the others. Days that exhibit this weather anomaly should not be used with this study's limited variable implementation. It is not clear if adding new variable inputs, such as wind, would improve the situation of 12/08/08; this can be the topic of future study.

4.4 Estimating perceived vegetation cover fraction.

The previous section used known land cover fractions to characterize and estimate the differential coefficient, $\frac{dT_o}{df_o}$. In a mixed thermal data point there is no information regarding cover fractions and so some other method is required to estimate them. One approach is to use *a priori* information gathered in the characterization of the correlation surface used to estimate $\frac{dT_o}{df_o}$. For example, the averaged cover fraction values for each angle could be used in place of the known fraction. A similar approach is to use *a priori* NDVI regression fits and sensed values to index the cover fraction. Both methods and results are presented below.

4.4.1 Using averaged perceived fractional cover.

In the study's approach, the camera resolution allows for the segmentation of the land covers and therefore known cover fractions are given for each sample. Variation is introduced into every sample by the operator and equipment, but this has been accounted for previously by calculating each sample's own cover fractions and using it throughout the processing. Practically, a mixed pixel approach does not give the land cover fractions, so this study now exercises the effect of applying an averaged cover value to each view. Averaged vegetation cover fractions are taken from the nadir and oblique samples for each bed and applied to all samples in place of the known individual cover fractions. The results can be found in Appendix (F.4) and (G.4) for each bed, respectively.

For the 12cm bed, individual day surface fits applied to other days give an average hit rate of 83.3% for the vegetation cover and 87.4% for the soil cover, excluding as above the 12/08/08 data set. Implementing the composite of two days on the remaining day raises the results to 93.3% for vegetation cover and 98.5% for the soil cover.

For the 24cm bed, individual day surface fits applied to other days give an average hit rate of 73.3% for the vegetation cover and 76.8% for the soil cover, including the full 12/08/14 data set. Implementing the composite of four days on the remaining day raises the results to 80.9% for vegetation cover and 83.6% for the soil cover.

4.4.2 Using NDVI to estimate perceived fractional cover.

This study now follows many other researcher's use of the NDVI value as an index to the vegetation fractional cover. The methods used and results are presented below in this final subsection.

As with the averaged fraction method above, prior characterization of the canopy geometry for NDVI indexing is required with this method. This method acquired NDVI samples, on the 12cm bed, at many angles and at different soil moistures, ranging from saturation to field capacity, to partially wet, and finally, to dry conditions. The images were segmented for land cover fractions by simple thresholding on the near-infrared band, as in the thermal images. Graphs

and tables for NDVI estimation of vegetation cover fraction are presented in Appendix(F.5). The scatter plot of known fraction and NDVI values shows the responses to different soil moistures. It is interesting that the dry soil samples are distinct and at the top of the scatter plot.

The regression fit associated with field capacity soil moisture was used to index the vegetation cover (perceived) fraction because the plants in this study had a constant water supply at the field capacity level. Overall sampling procedures are described in Section(4.1.2) and its subsequent sections, but additionally, in order to use the NDVI data, post-acquisition processing was necessary. Thermal image to NDVI image registration is necessary because both images, representing different spectral bands, need to represent the same objects, even in mixed form.

Additionally, spectral band adjustments need to be performed for the NDVI image. For each sample run, a photographic "gray" card was placed on the canopy and imaged. This image was used to calibrate the near-infrared and red bands of the image for equal data range responses, similar to a photographer "white balancing" a color image in the (now digital) darkroom. Because the NDVI camera has a different field-of-view and pixel resolution than does the thermal camera, a scaling operation was performed to match the images in pixel size. Registration of the two images was then performed by convolving the thermal image over the NDVI image with the maximum, normalized, cross-correlation value indicating the position in the image of the best match. The NDVI image was then cropped

to match thermal image in size and, finally, all pixels were averaged to represent a mixed pixel NDVI value. The mixed value is used to calculate the vegetation perceived fraction from the previous regression fit. Figures in Appendix(F.5) show a data sample composed of four images, demonstrating the registration. Due to small differences in positioning the two cameras, some parallax errors can be seen as shifts in both the background and foreground in the images.

Tables in Appendix (F.5) show the results of using NDVI indexes to cover fractions for individual and combined surface fits, as applied to other days. The individual day surface fits applied to other days give an average hit rate of 78.2% for the vegetation cover and 78.9% for the soil cover. As in the known and averaged fraction implementations, the sample day 12/08/16 responds well as a recipient to the other day's surface fits but does not reciprocate well to the other days. Applying combined surface fits to the remaining day with NDVI indexes gave an averaged hit rate of of 88.2% for the vegetation cover and 90.4% for the soil cover. As before, using combined day surface fits gives a boost to the results.

In summary, this method of estimating perceived vegetation cover fraction appears better than the averaged method above. Overall, for this bed and scope, about nine times out ten the NDVI method gets closer to the sensed cover temperature than does the mixed temperature for any arbitrary time delay sampling throughout the day. The averaged method is slightly behind at eight and a half times out of ten closer than the mixed temperature.

5 CONCLUSIONS and RECOMMENDATIONS for FUTURE STUDIES.

5.1 Summary of approach.

The intention of this study is to incrementally add to the understanding and computational practice of separating mixed land cover temperatures found in low-resolution thermal sensor data, as from current weather satellites. Data from these sensors render the temperature of large land expanses as radiometrically mixed values of the different component cover temperatures and not on a cover-by-cover basis. The ability to discriminate cover temperatures at the sub-pixel level is important because the segmented temperatures can be applied separately in two-source water and energy balance models, and to a greater effect than using mixed models on sparsely vegetated land.

This research expands the scope of previous studies by including time-delayed sampling of mixed thermal data, which inherently introduces environmental influences to the component cover temperatures from one data point to the other. To address these influences, the differential coefficients, $\frac{dT_v}{df_\theta}$ and $\frac{dT_s}{df_\theta}$, are proposed in this research to express the environmental *and* radiometric view effects and so are retained in the algebraic system,

$$\begin{aligned} \epsilon_m T_m^4 &= f_\theta \epsilon_v T_v^4 + (1 - f_\theta) \epsilon_s T_s^4 & (26) \\ 4\epsilon_m T_m^3 \frac{dT_m}{df_\theta} + T_m^4 \frac{d\epsilon_m}{df_\theta} &= \epsilon_v T_v^4 - \epsilon_s T_s^4 + f_\theta 4\epsilon_v T_v^3 \frac{dT_v}{df_\theta} + (1 - f_\theta) 4\epsilon_s T_s^3 \frac{dT_s}{df_\theta} \end{aligned}$$

while previous bi-angular studies, using near instantaneous sampling, set these coefficients to zero.

Nonetheless, the encapsulation of environmental and view influences in the differential coefficients is shown by rearranging the sensible heat equation as,

$$T_{ao} = T_a + \frac{r_a H}{\rho C_p}$$

and using the energy balance equation and radiometric view conditions on the above equation allows the radiometric cover temperature to be expressed environmentally and geometrically in general as,

$$T_{ro} = F(f_\theta, T_a, R_n, R_h, V_w, P_a \dots).$$

Taking the total derivative with respect to perceived fraction, and dropping the radiometric subscript,

$$\frac{dT_o}{df_\theta} = \frac{\partial T_o}{\partial f_\theta} + \frac{\partial T_o}{\partial T_a} \frac{dT_a}{df_\theta} + \frac{\partial T_o}{\partial R_n} \frac{dR_n}{df_\theta} + \frac{\partial T_o}{\partial R_h} \frac{dR_h}{df_\theta} + \frac{\partial T_o}{\partial V_w} \frac{dV_w}{df_\theta} + \frac{\partial T_o}{\partial P_a} \frac{dP_a}{df_\theta} + \dots$$

gives a definition of the differential coefficient in view and environmental terms.

Synthetic data, with known differential coefficient values, were used to verify the more descriptive approach of separating, or unmixing, cover temperatures. Next, a thermal camera was used which allowed the values of the differential coefficients to be computed and used, as in the synthetic case. Laboratory ver-

ification exercises were performed under controlled environmental conditions on potted plants providing canopy and sand.

Field studies were conducted on two beds of plants with different geometries and with limited environmental influences. Environmental variables were clamped by shade and partial thermal and wind blocks to reduce complexity, leaving the truncated definition of the differential coefficient as,

$$\frac{dT_o}{df_\theta} = \frac{\partial T_o}{\partial f_\theta} + \frac{\partial T_o}{\partial T_a} \frac{dT_a}{df_\theta} + \frac{\partial T_o}{\partial R_h} \frac{dR_h}{df_\theta} + \frac{\partial T_o}{\partial P_a} \frac{dP_a}{df_\theta}.$$

Concurrent weather data and staggered radiometric samples in time were used to generate estimation functions for $\frac{dT_o}{df_\theta}$ through multi-variate regression fits. These weather surface fits were exercised on the data sets in various ways from using a composite fit of all days applied to all days, to composite fits of some days applied to other days, and from individual day fits applied to other days. Result anomalies were identified and described using the Principal Component Analysis method which decomposes correlated input variables onto an orthogonal basis, giving a better understanding of surface fit contributions made by the variables.

Finally, to emulate a complete mixed pixel situation, perceived vegetation fractional covers were estimated by using an averaged value for each view from previous sampling and, separately, by using a mixed NDVI value as an index to fractional cover for each view. The estimated fractions were then exercised with the weather surface fits used to estimate the differential coefficient, $\frac{dT_o}{df_\theta}$.

5.2 Observations.

The functions used in this study to estimate the differential coefficient, $\frac{dT_o}{df_\theta}$, were generated by a regression fit of weather variables and the dependent variable, $\frac{dT_o}{df_\theta}$. As more weather variables were introduced into the data space, R^2 values improved and so did results in general. As a first order estimation for the differential coefficient,

$$\frac{dT_o}{df_\theta} = C_0 + C_1\Delta T_a + C_2\Delta R_h + C_3\Delta P_a$$

this estimation function has a direct term-by-term correspondence with the above truncated definition of the differential coefficient. Here, the view effect term can be seen as approximately equal to the intercept of the weather surface fit, $\frac{\partial T_o}{\partial f_\theta} \approx C_0$. The results in this study validates this interpretation.

Results also improved when more data points across days are used to generate the surface fit. Individual day surface fits applied to that day's data worked well, but could not be applied to other days reliably. Surface fits using all sample points for a bed also worked well on all the days, but as with the individual day self application, this application only verifies that the surface fit works on its own data.

Days were divided into training and target data sets for both beds. The 12cm bed, excluding day 12/08/08, gave excellent results when a two day surface

fit was applied to the remainder day. In one case, a week separated the training and target sets and the results were that 93% of calculated cover temperatures for both covers were closer to the sensed temperature than was the mixed temperature, for all time delayed sampling, throughout the target day.

For the 24cm bed, applying a two day composite surface fit on the remainder days was not as successful, however, the three and four day composite surface fits did boost results. The three day composite fit gave results that averaged 87% hit rate for both covers on the target days. One three day composite surface fit gave 100% hit rate for both covers, for both remaining days. Using a four day composite surface fit raised the average hit slightly to 90% for the vegetation cover and to 89% for the target day. These averages include the complete data of day 12/08/14.

The above results came from exercises conducted with known perceived vegetation fractions. Using estimated fractions from *a priori* averaged fraction value for nadir and oblique views affected the 24cm bed results more the 12cm bed. The average hit rate was lowered to 81% for the vegetation cover and 84% for soil cover when a four day composite surface with the average fractional values for the 24cm bed. The 12cm bed actually improved results by using the averaged fractional cover. Exercising NDVI estimates for fractional cover was not done for the 24cm bed, due to bad signal acquisition. However, the 12cm bed responded well to NDVI estimations with an average hit rate of 88% and 90% for vegetation

and soil covers, respectively, when using a two day composite surface fit on the remaining day.

Another observation is that when the inverse relationship between the difference in air temperature and the difference in relative humidity is broken, then this method with just three weather parameters does not work well. Another description of the same situation using Principal Component Analysis indicates that if the vector loadings, of all variables, in the data set point in the same direction with respect to the principal component, then this method will not work well.

5.3 Conclusions.

This study has heuristically derived a first-order estimation of the differential coefficients required to decompose land cover temperatures from time-delayed mixed data points. Applying the estimated values on target days gave a high success rate for a local time span. The success criteria was based on whether the results were better than just using the mixed pixel to determining cover temperature. Moreover, a decibel representation of closeness showed that most calculated points were many times closer to the sensed temperature than was the mixed temperature.

This study's results indicate that the sparse canopy, 12cm bed, had tighter precision spreads and smaller biases than did the denser canopy, 24cm bed. This is probably due to the diminished soil cover presentation at the oblique angle

for the dense canopy. Future studies can determine if a less oblique angle would suffice for more dense canopies or to determine the upper limit of canopy density for reliable results.

This has been a preliminary study and can be considered incomplete in that a generalized estimation function was not put forth. However, the intent of the study was more narrowly defined in the hypothesis. The intent was to see if the differential coefficients, $\frac{dT_v}{df_\theta}$ and $\frac{dT_s}{df_\theta}$, could be sufficiently characterized, for accurate separation of cover temperatures, by trending their response to a minimum of environmental influences. This study has demonstrated, within this scope, that the estimated differential coefficients can be used successfully. By doing so, this study has established a foothold in the pursuit of a more generalized estimation function for the application of delayed sampling of mixed pixels. Additionally, this study has also showed that using NDVI values to index perceived fractional cover is also successful and so completes the process of strictly using mixed pixel values.

5.4 Potential improvements and recommendations.

Large turbulent air disturbances can affect the relationship between air temperature and relative humidity and on these occasions, adding a wind variable to the regressive fit may improve the results in this method. Another suggestion for improvement is to increase the sample day size to see what the optimal com-

bination of days might be and to what extent the training surfaces can be applied to other days. For both cases, it is clear that additional automation in acquisition and processing is required. The intent is to see if adding more variables, or more samples, or both, can lead to a generalized estimation function of $\frac{dT_o}{df_\theta}$. One aspect of this would include synthesizing surface fits for $\frac{dT_o}{df_\theta}$ in order to probe the limits of functional surface fit boundaries.

Results might improve by reducing the sampling time brackets, that is, to wait for full separation of cover temperatures in the morning and stopping in mid-afternoon rather than early evening. These times correspond to large $\frac{dT_o}{df_\theta}$ values and with this study's limited parametric definition the large values became problematic with the results on occasion, such as with sample day 12/08/14. These early and late times were included in this study to exercise the method to a fuller extent and are included the results. Additional aspects that should be included in future studies is to consider non-Lambertian effects regarding different angle views and to consider how varying soil moisture content would vary results.

Implementing this study in a large greenhouse, where environmental conditions can be controlled, would advance the level of understanding practically in several ways. Shading can be applied when sampling occurs, and removed when not sampling to maintain plant health. The greenhouse would allow for a higher elevation placement of the cameras thereby expanding the field-of-view scale. This would give a better representation of the land covers. Expanding

the range in cover temperatures would better exercise this method with larger cover temperature differences. A well-equipped greenhouse can provide this condition by heating the air temperature while providing constant water supply to the plants. To provide the opposite effect, soil could be heated from the floor and cool air temperatures generated artificially.

The greenhouse implementation can also lead to a sunlit version study, where four land covers are considered: shaded and sunlit portions of vegetation and soil. In this case, sophisticated imaging would be required to discriminate the covers. Radiometers would be needed as net radiation values would be an added weather variable. The main question to be answered in the sunlit version study is: can shaded and sunlit covers be treated independently?

With the greenhouse experience in sunlit and shaded covers, the study can be scaled up to sparse biomes and used to ground truth satellite implementations.

References

- [1] ALLEN, R., PEREIRA, L., AND RAES, D. *Crop evapotranspiration - Guidelines for computing crop water requirements*. Food and Agriculture Organization of the United Nations, Rome, (1998).
- [2] ARISTOTLE. *Meteorology (350 BCE)*, Translated by E. W. Webster. University of Adelaide, Adelaide, South Australia, (2004).
- [3] BRUTSAERT, W. *Evaporation into the atmosphere: Theory, history, and applications*. Environmental Fluid Mechanics. D. Reidel Publishing Company, (1991).
- [4] CARLSON, T., GILLIES, R., AND SCHMUGGE, T. An interpretation of methodologies for indirect measurement of soil water content. *Agricultural and Forest Meteorology* 77 (1995), 191–205.
- [5] CHEHBOUNI, A., LO SEEN, D., NJOKU, E., AND MONTENY, B. Examination of the difference between radiative and aerodynamic surface temperatures over sparsely vegetated surfaces. *Remote Sensing of Environment* 58 (1996), 177–186.
- [6] EHRLER, W. Cotton leaf temperatures as related to soil water depletion and meteorological factors. *Agronomy Journal* 65 (1973), 404–409.
- [7] FRANCOIS, C., OTTLE, C., AND PREVOT, L. Analytical parametrization of canopy directional emissivity and directional radiance in the thermal infrared: Application on the retrieval of soil and foliage temperatures using two directional measurements. *International Journal of Remote Sensing* 18, 12 (1997), 2587–2621.
- [8] GILLIES, R., CARLSON, T., CUI, J., KUSTAS, W., AND HUMES, K. A verification of the 'triangle' method for obtaining surface soil water content and energy fluxes from remote measurements of the normalized difference vegetation index (ndvi) and surface radiant temperature. *International Journal of Remote Sensing* 18, 15 (1997), 3145–3166.
- [9] GUTMAN, G., AND IGNATOV, A. The derivation of the green vegetation fraction from noaa/avhrr data for use in numerical weather prediction models. *International Journal of Remote Sensing* 19, 8 (1998), 1533–1543.
- [10] HALL, F., HUEMMIRICH, K., GOETZ, S., SELLERS, P., AND NICKESON, J. Satellite remote sensing of surface energy balance: success, failures, and unresolved issues in fife. *Journal of Geophysical Research* 97, D17 (Nov. 1992), 19,061–19,089.

- [11] JIA, L., LI, Z.-L., MENENTI, M., SU, Z., VERHOEF, W., AND WAN, Z. A practical algorithm to infer soil and foliage component temperatures from bi-angular atsr-2 data. *International Journal of Remote Sensing* 24, 23 (2003), 4739–4760.
- [12] KIMES, D. Effects of vegetation canopy structure on remotely sensed canopy temperatures. *Remote Sensing of Environment* 10 (1980), 165–174.
- [13] KIMES, D. Remote sensing of row crop structure and component temperatures and inversion techniques. *Remote Sensing of Environment* 13 (1983), 33–55.
- [14] KIMES, D., AND KIRCHNER, J. Directional radiometric measurements of row-crop temperatures. *International Journal of Remote Sensing* 4, 2 (1983), 299–311.
- [15] KUSTAS, W., AND NORMAN, J. Use of remote sensing for evapotranspiration monitoring over land surfaces. *Hydrological Sciences Journal* 41, 4 (Aug. 1996).
- [16] KUSTAS, W., AND NORMAN, J. A two-source approach for estimating turbulent fluxes using multiple angle thermal infrared observations. *Water Resources Research* 33, 6 (June 1997), 1495–1508.
- [17] KUSTAS, W., AND NORMAN, J. Evaluation of soil and vegetation heat flux predictions using a simple two-source model with radiometric temperatures for partial canopy cover. *Agricultural and Forest Meteorology* 94 (1999), 13–29.
- [18] KUSTAS, W., AND NORMAN, J. A two-source energy balance approach using directional radiometric temperature observations for sparse canopy covered surfaces. *Agronomy Journal* 92 (2000), 847–854.
- [19] KUSTAS, W., NORMAN, J., ANDERSON, M., AND FRENCH, A. Estimating subpixel surface temperatures and energy fluxes from the vegetation index-radiometric temperature relationship. *Remote Sensing of Environment* 85 (2003), 429–440.
- [20] LAGOUARDE, J., KERR, Y., AND BRUNET, Y. An experimental study of angular effects on surface temperature for various plant canopies and bare soils. *Agricultural and Forest Meteorology* 77, 3 (Dec. 1995).
- [21] LHOMME, J., MONTENY, B., AND AMADON, M. Estimating sensible heat flux from radiometric temperature over sparse millet. *Agricultural and Forest Meteorology* 68 (1994), 77–91.

- [22] LI, Z.-L., STOLL, M., ZHANG, R.-H., JIA, L., AND SU, Z. On the separate retrieval of soil and vegetation temperatures from atsr data. *Science in China: Earth Sciences* 44, 2 (Feb. 2001).
- [23] MONTIETH, J. Evaporation and environment. *Symposium of the Society of Experimental Biology* 19 (1965), 205–234.
- [24] MORAN, M., CLARKE, T., INOUE, Y., AND VIDAL, A. Estimating crop water deficit using the relation between surface-air temperature and spectral vegetation index. *Remote Sensing of Environment* 49 (1994), 246–263.
- [25] MORAN, M., PINTER, P., CLOTHIER, B., AND ALLEN, S. Effect of water stress on the canopy architecture and spectral indices of irrigated alfalfa. *Remote Sensing of Environment* 29, 3 (Sept. 1989), 251–261.
- [26] NORMAN, J., AND KUSTAS, W. Source approach for estimating soil and vegetation energy fluxes in observations of directional radiometric surface temperature. *Agricultural and Forest Meteorology* 77 (1995), 263–293.
- [27] OTTERMAN, J., BRAKKE, T., FUCHS, M., LAKSHMI, V., AND CADEDU, M. Longwave emission from a plant/soil surface as a function of the view direction: dependence on the canopy architecture. *International Journal of Remote Sensing* 20, 11 (1999), 2195–2201.
- [28] PENMAN, H. Natural evaporation from open water, bare soil and grass. *Proceedings of the Royal Society of London, Series A, Mathematical and Physical Sciences* 193, 1032 (Apr. 1948), 120–145.
- [29] RAMSEY, W., AND DONNAN, F. *The life and letters of Joseph Black, M.D.* Constable and Company, LTD, London, (1918).
- [30] ROSENZWEIG, C., POWLSON, D., AND HATFIELD, J. *Encyclopedia of soils in the environment*, vol. 1. Elsevier Science, (2005).
- [31] SOBRINO, J., JIMÉNEZ-MUÑOZ, J., AND VERHOEF, W. Canopy directional emissivity: comparison between models. *Remote Sensing of Environment* 99 (2005), 304–314.
- [32] TUCKER, C. Red and photographic infrared linear combinations for monitoring vegetation. *Remote Sensing of Environment* 8 (1979), 127–150.
- [33] VERHOEF, A., DE BRUIN, H., AND VAN DEN HURK, B. Some practical notes on the parameter kb-1 for sparse vegetation. *Journal of Applied Meteorology* 36 (1997), 560–572.

- [34] ZHAN, W., CHEN, Y., ZHOU, J., AND LI, J. An algorithm for separating soil and vegetation temperatures with sensors featuring a single thermal channel. *IEEE Transactions on Geoscience and Remote Sensing*, 99 (2011).
- [35] ZHANG, R.-H., SUN, X.-M., LI, Z.-L., XU, J.-P., JING-TIAN, ZHU, Z.-L., AND WANG, W.-M. To separate mixed pixel temperature using differential coefficient of pixel mixed temperature to vegetation fractional cover. *Geoscience and Remote Sensing Symposium* (2005), 3262–3265.
- [36] ZHANG, R.-H., SUN, X.-M., WANG, W.-M., XU, J.-P., ZHU, Z.-L., AND TIAN, J. An operational two-layer remote sensing model to estimate surface flux in regional scale: physical background. *Science in China: Earth Sciences* 48, Supp. (2005).
- [37] ZHANG, R.-H., TIAN, J., SU, H.-B., SUN, X.-M., CHEN, S., AND XIA, J. Two improvements of an operational two-layer model for terrestrial surface heat flux retrieval. *Sensors* 8 (2008), 6165–6187.

A Variable Lists.

The variables used in this dissertation are described below:

Table 14: Greek Variable List

Variable	Description
α	Albedo (shortwave reflection)
γ	Psychrometric constant
ε	Surface Emissivity
ε_a	Atmospheric emissivity
ε_m	Mixed surface emissivity
ε_o	General land cover surface emissivity
ε_s	Soil surface emissivity
ε_v	Vegetation surface emissivity
ρ	Atmospheric density
σ	Stefan-Boltzmann constant
ψ_h	Correction factor for sensible heat transfer
ψ_m	Correction factor for momentum transfer
ψ_v	Correction factor for vapor flow

Table 15: Modern Variable List

Variable	Description
a_{bi}	Intensity (reflected or emitted) of the i^{th} end-member in b
b	Spectral band
C_p	Specific heat capacity of air
d_p	Zero plane offset of the wind profile
$e(T)$	water vapor pressure at water temperature T
$e_s(T_o)$	Saturated water vapor pressure at T_o
f_a	Actual vegetation cover fraction (0-1)
f_i	Areal fraction of the pixel of the i^{th} end-member (0-1)
f_{θ}	Perceived vegetation cover fraction (0-1)
G	Ground heat transfer flux (conduction)
H	Sensible heat transfer flux (turbulent)
I	Electrical current flux
I_p	Pixel intensity value
k	von Karmen constant
L	Long wave solar radiation (thermal)
LE	Latent heat transfer (evapotranspiration)
m	Denotes a mixed value
N	Number of end-members
r_{ah}	Aerodynamic surface resistance to heat flow
P_a	Atmospheric pressure
r_{ov}	Surface resistance to vapor flow
r_{av}	Aerodynamic resistance to vapor flow
r	Electrical resistance
R_n	Net solar radiation
R_h	Relative humidity
S	Short wave solar radiation (visible)

Table 16: Modern Variable List (con't)

Variable	Description
T_a	Air temperature
T_o	Generic surface temperature
T_{ao}	Generic aerodynamic surface temperature
T_{ro}	Generic radiometric surface temperature
T_m	Radiometric mixed temperature
T_s	Radiometric soil temperature
T_w	Wet bulb temperature
T_v	Radiometric vegetation temperature
u_z	Wind measurement at height z_u
V	Electrical voltage
V_w	Wind velocity
z_{oh}	Roughness length for sensible heat transfer
z_{om}	Roughness length for momentum transfer
z_T	Height at which air temperature is measured
z_u	Height at which wind velocity is measured

B Acronym List.

Table 17: Acronym List

Acronym	Description
ATSR	Along Track Scanning Radiometer (ESA)
AATSR	Advanced Along Track Scanning Radiometer (ESA)
AVHRR	Advanced Very High Resolution Radiometer
ESA	European Space Agency
GNU	GNU's Not Unix (Free Software Foundation)
GUI	Graphical User Interface
LST	Land Surface Temperature
METOP-A	Operational Meteorological Polar Orbiting Satellite (ESA)
MODIS	Moderate Resolution Imaging Spectroradiometer (NASA)
NASA	National Aeronautics and Space Agency
NDVI	Normalized Difference Vegetation Index
NOAA	National Oceanic and Atmospheric Agency
NOAA-18,19	NOAA Weather Polar Orbiting Satellites
PCA	Principal Component Analysis
POLI	Python On Line Imaging
STP	Standard Temperature and Pressure

C Differential Calculations.

Linear and quartic radiative transfer differentiations are given below.

C.1 Linear radiative transfer differentiation.

The linearized Stephan-Boltzmann equation for a mixed pixel with two components, T_v and T_s is,

$$\varepsilon_m T_m = f \varepsilon_v T_v + (1 - f) \varepsilon_s T_s \quad (27)$$

Taking the total derivative of the left side of Equation (27) with respect to fractional cover, f ,

$$\frac{d(\varepsilon_m T_m)}{df} = \frac{\partial(\varepsilon_m T_m)}{\partial T_m} \frac{dT_m}{df} + \frac{\partial(\varepsilon_m T_m)}{\partial \varepsilon_m} \frac{d\varepsilon_m}{df} = \varepsilon_m \frac{dT_m}{df} + T_m \frac{d\varepsilon_m}{df}$$

Taking the total derivative of the right side of Equation (27) with respect to f , term by term,

$$\begin{aligned} \frac{d(f \varepsilon_v T_v)}{df} &= \frac{\partial(f \varepsilon_v T_v)}{\partial T_v} \frac{dT_v}{df} + \frac{\partial(f \varepsilon_v T_v)}{\partial \varepsilon_v} \frac{d\varepsilon_v}{df} + \frac{\partial(f \varepsilon_v T_v)}{\partial f} \\ \frac{d(\varepsilon_s T_s)}{df} &= \frac{\partial(\varepsilon_s T_s)}{\partial T_s} \frac{dT_s}{df} + \frac{\partial(\varepsilon_s T_s)}{\partial \varepsilon_s} \frac{d\varepsilon_s}{df} \\ -\frac{d(f \varepsilon_s T_s)}{df} &= -\left(\frac{\partial(f \varepsilon_s T_s)}{\partial T_s} \frac{dT_s}{df} + \frac{\partial(f \varepsilon_s T_s)}{\partial \varepsilon_s} \frac{d\varepsilon_s}{df} + \frac{\partial(f \varepsilon_s T_s)}{\partial f} \right) \end{aligned}$$

Setting emissivity differentials $\frac{d\varepsilon_v}{df} = 0$ and $\frac{d\varepsilon_s}{df} = 0$ gives

$$\begin{aligned}
\frac{d(f\varepsilon_v T_v)}{df} &= f\varepsilon_v \frac{dT_v}{df} + \varepsilon_v T_v \\
\frac{d(\varepsilon_s T_s)}{df} &= \varepsilon_s \frac{dT_s}{df} \\
\frac{-d(f\varepsilon_s T_s)}{df} &= -(f\varepsilon_s \frac{dT_s}{df} + \varepsilon_s T_s)
\end{aligned}$$

Assembling both sides of the total derivative of Equation (27) gives

$$\varepsilon_m T_m \frac{dT_m}{df} + T_m \frac{d\varepsilon_m}{df} = \varepsilon_v T_v - \varepsilon_s T_s + f\varepsilon_v \frac{dT_v}{df} + (1-f)\varepsilon_s \frac{dT_s}{df} \quad (28)$$

Weighing out fractional vegetation cover for the mixed emissivity, $\varepsilon_m = f\varepsilon_v + (1-f)\varepsilon_s$, and taking the total derivative with respect to f gives

$$\frac{d\varepsilon_m}{df} = \frac{\partial(f\varepsilon_v)}{\partial\varepsilon_v} \frac{d\varepsilon_v}{df} + \frac{\partial(f\varepsilon_v)}{\partial f} + \frac{d\varepsilon_s}{df} - \frac{\partial(f\varepsilon_s)}{\partial\varepsilon_s} \frac{d\varepsilon_s}{df} - \frac{\partial(f\varepsilon_s)}{\partial f}$$

As above, $\frac{d\varepsilon_v}{df} = 0, \frac{d\varepsilon_s}{df} = 0$, yields

$$\begin{aligned}
\frac{d\varepsilon_m}{df} &= \frac{\partial(f\varepsilon_v)}{\partial f} - \frac{\partial(f\varepsilon_s)}{\partial f} \\
&= \varepsilon_v - \varepsilon_s
\end{aligned} \quad (29)$$

C.2 Quartic radiative transfer differentiation.

Stephan-Boltzmann equation for a mixed pixel with two components, T_v and T_s , is

$$\varepsilon_m T_m^4 = f \varepsilon_v T_v^4 + (1 - f) \varepsilon_s T_s^4 \quad (30)$$

Taking the total derivative of the left side of Equation (30) with respect to fractional cover, f ,

$$\frac{d(\varepsilon_m T_m^4)}{df} = \frac{\partial(\varepsilon_m T_m^4)}{\partial T_m} \frac{dT_m}{df} + \frac{\partial(\varepsilon_m T_m^4)}{\partial \varepsilon_m} \frac{d\varepsilon_m}{df} = 4\varepsilon_m T_m^3 \frac{dT_m}{df} + T_m^4 \frac{d\varepsilon_m}{df}$$

Taking the total derivative of the right side of Equation (30) with respect to f , term by term,

$$\begin{aligned} \frac{d(f \varepsilon_v T_v^4)}{df} &= \frac{\partial(f \varepsilon_v T_v^4)}{\partial T_v} \frac{dT_v}{df} + \frac{\partial(f \varepsilon_v T_v^4)}{\partial \varepsilon_v} \frac{d\varepsilon_v}{df} + \frac{\partial(f \varepsilon_v T_v^4)}{\partial f} \\ \frac{d(\varepsilon_s T_s^4)}{df} &= \frac{\partial(\varepsilon_s T_s^4)}{\partial T_s} \frac{dT_s}{df} + \frac{\partial(\varepsilon_s T_s^4)}{\partial \varepsilon_s} \frac{d\varepsilon_s}{df} \\ -\frac{d(f \varepsilon_s T_s^4)}{df} &= -\left(\frac{\partial(f \varepsilon_s T_s^4)}{\partial T_s} \frac{dT_s}{df} + \frac{\partial(f \varepsilon_s T_s^4)}{\partial \varepsilon_s} \frac{d\varepsilon_s}{df} + \frac{\partial(f \varepsilon_s T_s^4)}{\partial f} \right) \end{aligned}$$

Setting emissivity differentials $\frac{d\varepsilon_v}{df} = 0$ and $\frac{d\varepsilon_s}{df} = 0$ gives

$$\begin{aligned} \frac{d(f \varepsilon_v T_v^4)}{df} &= 4f \varepsilon_v T_v^3 \frac{dT_v}{df} + \varepsilon_v T_v^4 \\ \frac{d(\varepsilon_s T_s^4)}{df} &= 4\varepsilon_s T_s^3 \frac{dT_s}{df} \\ -\frac{d(f \varepsilon_s T_s^4)}{df} &= -(4f \varepsilon_s T_s^3 \frac{dT_s}{df} + \varepsilon_s T_s^4) \end{aligned}$$

Assembling both sides of the total derivative of Equation (30) gives

$$4\varepsilon_m T_m^3 \frac{dT_m}{df} + T_m^4 \frac{d\varepsilon_m}{df} = \varepsilon_v T_v^4 - \varepsilon_s T_s^4 + 4f\varepsilon_v T_v^3 \frac{dT_v}{df} + (1-f)4\varepsilon_s T_s^3 \frac{dT_s}{df}$$

and, as in the above linear version,

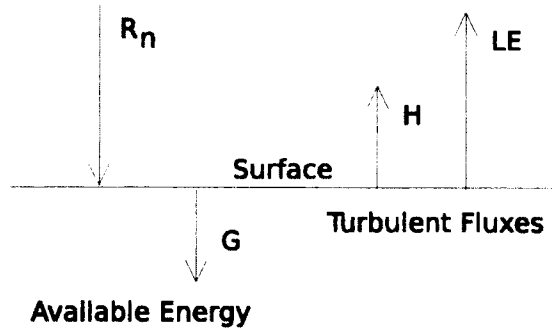
$$\frac{d\varepsilon_m}{df} = \varepsilon_v - \varepsilon_s$$

D Energy balance equations.

The surface energy balance in its simplified form is given as [30]:

$$R_n + H + LE + G = 0 \quad (31)$$

Surface Energy Balance



with positive values going toward the surface and negative values going away from the surface. Metabolic, chemical and other heat contributions (*ie.* uranium decay) are generally ignored due to their relatively small contributions. Sometimes, the ground conductive flux, G , is also ignored but it is usually estimated

as a function of the radiative energy, R_n , the overall driver of this system. R_n is constructed from short and long wave components from the sun, earth and atmosphere:

$$R_n = S(1 - \alpha) + L + \varepsilon_a \sigma T_a^4 - \varepsilon_o \sigma T_o^4$$

In general, short waves are considered as mostly reflective and long waves are considered as almost wholly absorptive, so there is no albedo factor for L . Also, knowing the aerodynamic surface temperature, T_{ao} , along with T_a , allows for better estimates of R_n for places without ground radiometer sensors. In our binary case, T_o can be represented by vegetation surface temperature, T_v , or soil surface temperature, T_s .

The turbulent fluxes, H and LE , are potential, diffusive equations and are analogous to Ohm's Law, $I = V/r$. For the sensible heat flux to and from the atmosphere we have the aerodynamic expression:

$$H = \frac{\rho C_p (T_{ao} - T_a)}{r_{ah}} \quad (32)$$

where r_{ah} is the aerodynamic resistance to heat flow between some mean height within the canopy to some reference height, z_u , above the canopy surface and is defined as:

$$r_{ah} = \frac{(\ln(\frac{z_u - d_p}{z_{om}}) - \psi_m)(\ln(\frac{z_T - d_p}{z_{oh}}) - \psi_h)}{k^2 u_z} \quad (33)$$

Therefore, to determine the sensible heat component, H , three highly variable values must be obtained, aerodynamic surface temperature, T_{ao} , surrounding air temperature, T_a , and wind velocity, u_z , in addition to the more static components z_u , d_p , z_{om} , ψ_m , z_T , z_{oh} , ψ_h and k .

Residual estimates of LE can be calculated by rearranging Equation (31):

$$LE = -R_n - H - G.$$

However, to obtain arithmetic closure, the aerodynamic expression for latent heat flux to and from the atmosphere should be included and is similar to Equation (32):

$$LE = \frac{\rho C_p (e_s(T_{ao}) - e(T_a))}{\gamma (r_{av} + r_{\alpha v})} \quad (34)$$

where $e(T)$ is the water vapor pressure at some temperature T . For both leaf and soil, if the surface, or slightly within, has available water, then T_{ao} can be considered as the wet bulb temperature, T_w , which gives the saturated vapor pressure $e_s(T_{ao})$. The vapor pressure of the surrounding air, $e(T_a)$, at some surface height, z , can be easily obtained by knowing the relative humidity, $R_h = \frac{e(T_a)}{e_s(T_a)}$. γ

is the psychrometric constant. Just as the temperature difference, $(T_{ao} - T_a)$, drives the sensible heat flux, it is the water vapor pressure difference, $(e_s(T_o) - e(T_a))$, that drives the latent heat flux, or evaporation.

The aerodynamic resistance to vapor flow, r_{av} , is similar to Equation (33),

$$r_{av} = \frac{(\ln(\frac{z_u - d_p}{z_{om}}) - \psi_m)(\ln(\frac{z_v - d_p}{z_{ov}}) - \psi_v)}{k^2 u_z}$$

but z_T is replaced by z_v , z_{oh} is replaced by z_{ov} , and ψ_h is replaced by ψ_v , a correction factor for vapor flow on the boundary layer. Practically, both humidity and temperature sensors are usually placed at the same height so that $z_T = z_v$, $z_{ov} = z_{oh}$ with the assumption that $\psi_v = \psi_h$. For a well-watered surface $\psi_v = \psi_h = \psi_m = 0$ [3].

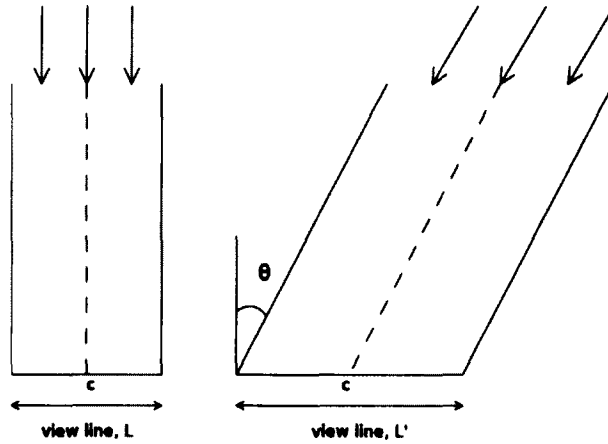
E Geometric effects.

E.1 Camera angle and view area.

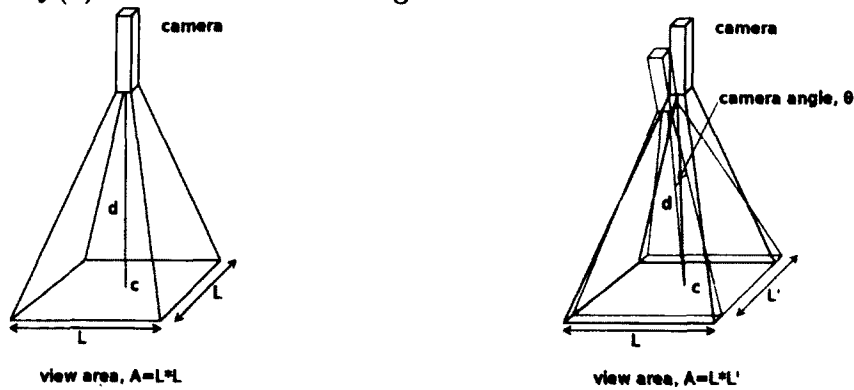
Observing that changing the camera view angle, θ , results in a change of sensed area, A , we wish to quantify and evaluate this effect. In this study's experimental setup, the camera angle variation is restricted to one plane, and ignoring side perspective effects, the area is defined as $A = L' \times L$, where the side L represents the fixed width and L' represents the length which varies with camera view angle, θ .

The function, $f_\theta(\theta) = A$, depends on the optical vector geometries used,

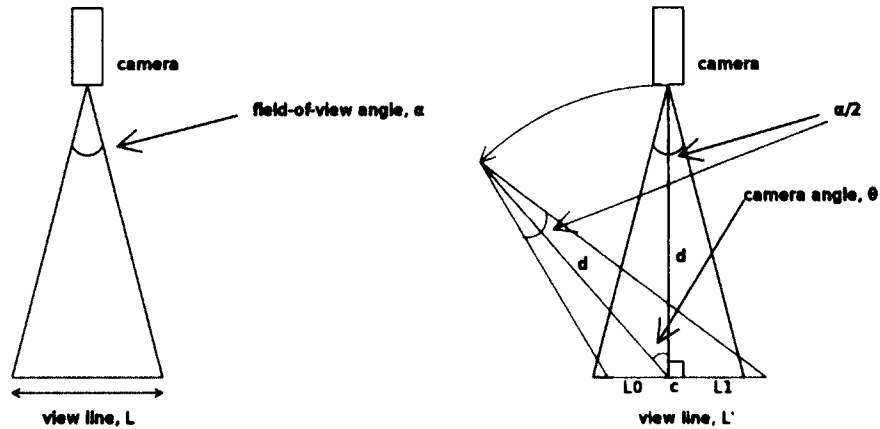
so, if the optical rays are parallel, we can use the Cosine Rule for area projection for a plane restricted rotation: $A = A_p / \cos \theta$, where A_p is the initial area at a perpendicular view, or nadir, shown below:



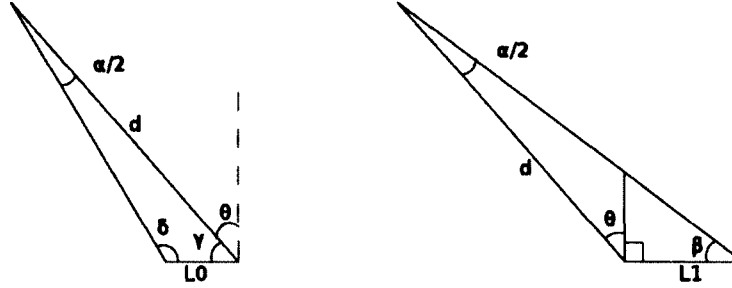
In this study, the center points in all camera views are kept coincident, within experimental means. For the hypothetical parallel case, the center point, c , can be kept centered by a simple halving of L' . In practice, sensor lenses have radial vector geometries centered at the focal point requiring a different approach to determine $f(\theta) = A$. A derivation is given below.



The above figures illustrate the approach taken. The figure on the left shows the camera sensor perpendicular to the view area, with d as the distance to the area center, c . We restrict camera angle variation to one plane, as in our experiment setup, so the side L represents the fixed length of the view area, ignoring perspective effects. The figure on the right shows how the length L' varies with changing camera angle, θ , and correspondingly, the area. The focal distance, d , remains fixed for all views.



These figures show the geometry involved within the restricted plane. The sensor has a field-of-view angle, α , which remains constant. Point c is kept in the center of angle α and at a constant distance d from the sensor. Varying θ then varies the view line L , so that $L' = L0 + L1$. The figures below are used to derive expressions for $L0$ and $L1$ as a function of θ .



The angles γ and δ are calculated by summing angles,

$$\gamma = 90^\circ - \theta$$

$$\delta = 180^\circ - \gamma - \alpha/2 = 90^\circ + \theta - \alpha/2$$

with $\alpha < 180^\circ$. Rearranging, $\delta = 90^\circ - \alpha/2 + \theta$ and using $a = 90^\circ - \alpha/2$,

$$\delta = a + \theta.$$

The Sine Rule and angles δ , $\alpha/2$ are used to solve for $L0$,

$$L0 = \frac{d \sin(\alpha/2)}{\sin(\delta)} = \frac{d \sin(\alpha/2)}{\sin(a + \theta)}.$$

Likewise, $\beta = a - \theta$ is used to solve for $L1$,

$$L1 = \frac{d \sin(\alpha/2)}{\sin(\beta)} = \frac{d \sin(\alpha/2)}{\sin(a - \theta)}.$$

So,

$$L' = L_0 + L_1 = \frac{d \sin(\alpha/2)}{\sin(a + \theta)} + \frac{d \sin(\alpha/2)}{\sin(a - \theta)}$$

and is restricted to $a > \theta$, since negative lengths are undefined. Setting $\theta = 0$, we can define the fixed length, L , as

$$L = \frac{2d \sin(\alpha/2)}{\sin(a)}$$

The varying area, A , is defined as $A = L \cdot L'$, so

$$A = f(\theta) = L \cdot \left[\frac{d \sin(\alpha/2)}{\sin(a + \theta)} + \frac{d \sin(\alpha/2)}{\sin(a - \theta)} \right]$$

Setting $r = L \cdot d \sin(\alpha/2)$ we have

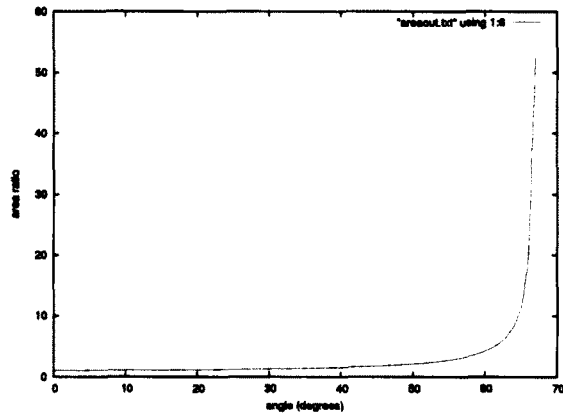
$$A = f(\theta) = \frac{r}{\sin(a + \theta)} + \frac{r}{\sin(a - \theta)}$$

Taking the derivative with respect to camera angle, θ , gives

$$\frac{dA}{d\theta} = \frac{r \cos(\theta - a)}{\sin^2(\theta - a)} - \frac{r \cos(\theta + a)}{\sin^2(\theta + a)}$$

E.2 Generated data.

A computer program generates values for the view area A , at 1° increments with camera distance of $1.0m$ and a field-of-view angle of $\alpha = 45^\circ$. The area values are plotted below as a ratio to the area at nadir:



The generated values show that the view area increases monotonically by 10% at $\theta = 21^\circ$, 25% at $\theta = 31^\circ$, and 100% at $\theta = 50^\circ$.

F Tabulated results for 12cm bed.

The first sub-section below shows results on the near instantaneous sampling and how the calculated temperatures compare to the mixed temperature value. Subsequent sub-sections show results of applying different hyper-surface fits to the mixed temperature data of the 12cm bed. Hyper-surfaces are henceforth called “surfaces” for simplicity. Sample day surface coefficients can be found in Table (8) while combined and average surface coefficients are given below when used.

F.1 Near instantaneous sampling results and metrics used.

The following tables show the results of applying averaged differential coefficients, $\frac{dT_v}{df_\theta}$ and $\frac{dT_s}{df_\theta}$, to all near instantaneous samples for both land covers. The calculated temperatures are then compared to the mixed temperature values. Table headings are: t_s is the sensed cover temperature, t_m is the mixed temperature; t_c is the calculated temperature from unmixing; a is the absolute difference of the sensed temperature, t_s , and the mixed temperature, t_m ; and b is the absolute difference of the sensed temperature, t_s , and the calculated temperature t_c . Dividing b into a gives a measure of performance. If the calculated temperature is closer to the sensed temperature than is the mixed temperature, then a “1” is assigned to the right most column. Bottom row indicates the percentage of samples that performed better than the mixed temperature.

t_{sensed}	t_{mixed}	$a = abs(t_{sensed} - t_{mixed})$	t_{calc}	$b = abs(t_{sensed} - t_{calc})$	a/b	
296.254	295.718	0.536	295.260	0.994	0.539	
297.727	296.385	1.342	297.511	0.216	6.213	1
297.867	296.637	1.230	298.055	0.188	6.543	1
298.365	297.191	1.174	298.735	0.370	3.173	1
296.886	295.966	0.920	295.967	0.919	1.001	1
296.150	294.376	1.774	294.585	1.565	1.134	1
294.900	294.024	0.876	294.355	0.545	1.607	1
296.733	295.338	1.395	296.665	0.068	20.515	1
297.951	296.301	1.650	298.661	0.710	2.324	1
298.298	296.407	1.891	298.351	0.053	35.679	1
299.396	297.433	1.963	299.385	0.011	178.455	1
300.644	298.376	2.268	300.395	0.290	9.108	1
301.864	299.146	2.718	302.506	0.642	4.234	1
301.190	298.894	2.296	301.925	0.735	3.124	1
298.211	297.090	1.121	299.078	0.867	1.293	1
294.548	293.724	0.824	293.701	0.847	0.973	
296.739	295.161	1.578	296.716	0.023	68.609	1
297.467	296.003	1.464	297.160	0.307	4.769	1
298.140	296.481	1.659	298.237	0.097	17.103	1
299.884	297.581	2.303	300.393	0.509	4.525	1
300.557	298.283	2.274	300.683	0.126	18.048	1
300.734	298.982	1.752	301.086	0.352	4.977	1
298.370	296.919	1.451	297.923	0.447	3.246	1
297.961	296.626	1.335	298.074	0.113	11.814	1
294.430	292.812	1.618	294.686	0.256	6.320	1
295.980	294.404	1.576	295.966	0.014	112.571	1
296.056	294.805	1.251	294.662	1.394	0.897	
296.174	295.156	1.018	296.874	0.700	1.454	1
297.218	295.775	1.443	297.495	0.277	5.209	1
298.524	296.68	1.844	298.139	0.385	4.790	1
298.142	296.28	1.862	298.739	0.597	3.119	1
298.956	296.908	2.048	299.188	0.232	8.828	1
298.627	296.711	1.916	298.771	0.144	13.306	1
299.864	298.138	1.726	300.660	0.796	2.168	1
						91.2%

Table 18: Vegetation cover results for “instantaneous” samples with averaged $\frac{dT_v}{df_\theta}$ and $\frac{dT_s}{df_\theta}$ for 12cm bed.

t_{sensed}	t_{mixed}	$a = abs(t_{sensed} - t_{mixed})$	t_{calc}	$b = abs(t_{sensed} - t_{calc})$	a/b	
295.311	295.718	0.407	296.064	0.753	0.541	
295.425	296.385	0.960	295.582	0.157	6.115	1
295.984	296.637	0.653	295.883	0.101	6.465	1
296.389	297.191	0.802	296.133	0.256	3.133	1
295.346	295.966	0.620	295.965	0.619	1.002	1
293.133	294.376	1.243	294.231	1.098	1.132	1
293.445	294.024	0.579	293.806	0.361	1.604	1
294.378	295.338	0.960	294.425	0.047	20.426	1
295.092	296.301	1.209	294.561	0.531	2.277	1
295.072	296.407	1.335	295.034	0.038	35.132	1
295.929	297.433	1.504	295.939	0.010	150.400	1
296.636	298.376	1.740	296.831	0.195	8.923	1
297.128	299.146	2.018	296.638	0.490	4.118	1
297.229	298.894	1.665	296.682	0.547	3.044	1
296.302	297.090	0.788	295.682	0.620	1.271	1
293.075	293.724	0.649	293.743	0.668	0.972	
293.999	295.161	1.162	294.016	0.017	68.353	1
294.877	296.003	1.126	295.116	0.239	4.711	1
295.262	296.481	1.219	295.19	0.072	16.930	1
295.846	297.581	1.735	295.453	0.393	4.415	1
296.582	298.283	1.701	296.486	0.096	17.719	1
297.144	298.982	1.838	296.766	0.378	4.862	1
295.840	296.919	1.079	296.175	0.335	3.221	1
295.573	296.626	1.053	295.483	0.090	11.700	1
291.747	292.812	1.065	291.576	0.171	6.228	1
293.310	294.404	1.094	293.32	0.010	109.400	1
294.063	294.805	0.742	294.889	0.826	0.898	
294.441	295.156	0.715	293.942	0.499	1.433	1
294.764	295.775	1.011	294.568	0.196	5.158	1
295.417	296.680	1.263	295.685	0.268	4.713	1
294.991	296.280	1.289	294.568	0.423	3.047	1
295.429	296.908	1.479	295.258	0.171	8.649	1
295.413	296.711	1.298	295.314	0.099	13.111	1
296.835	298.138	1.303	296.221	0.614	2.122	1
						91.2%

Table 19: Soil cover results for near instantaneous samples with averaged $\frac{dT_v}{df_\theta}$ and $\frac{dT_s}{df_\theta}$ for 12cm bed.

F.2 Combined and averaged surface fits with known cover fractions.

The following tables show the results of applying combined and averaged surface fits to estimate the differential coefficients, $\frac{dT_v}{df_\theta}$ and $\frac{dT_s}{df_\theta}$, to the mixed data with known cover fractions. Asterisks denote when surface coefficients were applied to days from which they were partially derived.

	type	intrept	ΔT_a	ΔR_h	ΔP_a	R^2
veg fit	combined 08 09	1.140	3.979	0.261	-1.974	0.897
	averaged 08 09	0.765	4.445	1.146	-3.047	
soil fit	combined 08 09	1.689	3.295	0.833	-1.966	0.922
	averaged 08 09	1.163	2.227	0.795	-2.463	

(a) Combined and averaged surface fit coefficients.

day	veg response			soil response		
	std C	bias C	%	std C	bias C	%
120808*	1.200	-0.282	60.6	0.833	0.188	60.6
120809*	0.607	0.189	100.0	0.461	-0.145	97.8
120810	0.757	-0.460	93.3	0.694	0.377	93.3
120816	0.933	0.739	86.7	0.694	0.565	86.7

(b) Cover responses using combined surface fit.

day	veg response			soil response		
	std C	bias C	%	std C	bias C	%
120808*	1.001	-0.501	66.6	0.694	0.348	66.6
120809*	1.441	0.905	68.9	1.096	-0.708	68.9
120810	1.272	-0.384	75.6	1.018	0.298	75.6
120816	1.335	-0.164	80.0	0.962	0.161	78.0

(c) Cover responses using averaged surface fit.

Table 20: Unmixing results using estimated differential coefficients, $\frac{dT_v}{df_\theta}$ and $\frac{dT_s}{df_\theta}$, derived from combined and averaged surface fits for dates 12/08/08 and 12/08/09 as predictor for 12cm bed. Known cover fractions were used.

	type	intrcpt	ΔT_a	ΔR_h	ΔP_a	R^2
veg fit	combined 08 10	0.184	3.295	0.167	-1.766	0.883
	averaged 08 10	-0.438	3.282	0.853	-3.188	
soil fit	combined 08 10	1.514	3.077	0.902	-1.806	0.929
	averaged 08 10	1.255	2.396	0.860	-2.324	

(a) Combined and averaged surface fit coefficients.

day	veg response			soil response		
	std C	bias C	%	std C	bias C	%
120808*	1.130	-0.062	72.7	0.790	0.046	72.7
120809	0.805	0.906	88.9	0.619	-0.690	88.9
120810*	0.603	0.034	97.7	0.528	-0.029	97.7
120816	1.119	-0.210	91.1	0.801	0.190	91.1

(b) Cover responses using combined surface fit.

day	veg response			soil response		
	std C	bias C	%	std C	bias C	%
120808*	1.026	-0.424	78.8	0.712	0.300	78.8
120809	1.540	1.163	66.7	1.179	-0.907	66.7
120810*	1.337	-0.165	77.8	1.064	0.118	77.8
120816	1.393	0.073	77.8	0.995	-0.011	77.8

(c) Cover responses using averaged surface fit.

Table 21: Unmixing results using estimated differential coefficients, $\frac{dT_v}{df_\theta}$ and $\frac{dT_s}{df_\theta}$, derived from combined and averaged surface fits for dates 12/08/08 and 12/08/10 as predictor for 12cm bed. Known cover fractions were used.

	type	intrcpt	ΔT_a	ΔR_h	ΔP_a	R^2
veg fit	combined 08 16	-0.895	2.900	0.741	-4.268	0.860
	averaged 08 16	-1.198	3.096	0.927	-4.086	
soil fit	combined 08 16	0.685	3.482	0.556	-1.488	0.888
	averaged 08 16	0.743	2.943	0.667	-1.920	

(a) Combined and averaged surface fit coefficients.

day	veg response			soil response		
	std C	bias C	%	std C	bias C	%
120808*	1.260	0.101	57.6	0.873	-0.068	57.6
120809	0.651	0.551	91.1	0.496	-0.414	91.1
120810	0.835	0.034	95.6	0.768	-0.017	93.3
120816*	0.849	-0.065	95.6	0.616	0.075	95.6

(b) Cover responses using combined surface fit.

day	veg response			soil response		
	std C	bias C	%	std C	bias C	%
120808*	1.126	-0.053	75.8	0.779	0.043	75.8
120809	0.877	0.932	80.0	0.673	-0.712	80.0
120810	0.848	0.015	91.1	0.732	-0.010	91.1
120816*	1.084	0.127	88.9	0.776	-0.057	88.9

(c) Cover responses using averaged surface fit.

Table 22: Unmixing results using estimated differential coefficients, $\frac{dT_v}{df_\theta}$ and $\frac{dT_s}{df_\theta}$, derived from combined and averaged surface fits for dates 12/08/08 and 12/08/16 as predictor for 12cm bed. Known cover fractions were used.

	type	intrcpt	ΔT_a	ΔR_h	ΔP_a	R^2
veg fit	combined 09 10	0.875	4.658	0.532	-1.424	0.934
	averaged 09 10	1.319	5.409	0.932	-1.338	
soil fit	combined 09 10	1.808	2.122	0.282	-1.748	0.963
	averaged 09 10	1.797	2.119	0.307	-1.778	

(a) Combined and averaged surface fit coefficients.

day	veg response			soil response		
	std C	bias C	%	std C	bias C	%
120808	1.472	-0.959	39.4	1.020	0.658	39.4
120809*	0.542	0.222	100.0	0.405	-0.172	100.0
120810*	0.532	-0.215	95.6	0.492	0.180	95.6
120816	0.917	-0.337	93.3	0.655	0.270	93.3

(b) Cover responses using combined surface fit.

day	veg response			soil response		
	std C	bias C	%	std C	bias C	%
120808	1.446	-0.935	39.4	1.003	0.642	39.4
120809*	0.550	0.255	100.0	0.412	-0.197	100.0
120810*	0.523	-0.218	95.6	0.483	0.182	95.6
120816	0.933	-0.335	91.1	0.667	0.269	91.1

(c) Cover responses using averaged surface fit.

Table 23: Unmixing results using estimated differential coefficients, $\frac{dT_v}{df_\theta}$ and $\frac{dT_s}{df_\theta}$, derived from combined and averaged surface fits for dates 12/08/09 and 12/08/10 as predictor for 12cm bed. Known cover fractions were used.

	type	intrcpt	ΔT_a	ΔR_h	ΔP_a	R^2
veg fit	combined 09 16	-0.326	4.729	0.470	-1.850	0.905
	averaged 09 16	0.559	5.222	1.007	-2.235	
soil fit	combined 09 16	1.499	2.303	0.278	-1.851	0.904
	averaged 09 16	1.286	2.667	0.114	-1.374	

(a) Combined and averaged surface fit coefficients.

day	veg response			soil response		
	std C	bias C	%	std C	bias C	%
120808	1.669	-0.942	33.3	1.147	0.646	33.3
120809*	0.605	0.116	97.8	0.453	-0.091	97.8
120810	0.667	-0.128	95.6	0.623	0.116	95.6
120816*	0.797	-0.113	97.8	0.569	0.103	97.8

(b) Cover responses using combined surface fit.

day	veg response			soil response		
	std C	bias C	%	std C	bias C	%
120808	1.574	-0.560	39.4	1.088	0.384	39.4
120809*	0.885	0.002	95.6	0.659	-0.002	95.6
120810	1.025	-0.055	86.7	0.900	0.055	86.7
120816*	0.690	-0.285	100.0	0.500	0.224	100.0

(c) Cover responses using averaged surface fit.

Table 24: Unmixing results using estimated differential coefficients, $\frac{dT_v}{df_\theta}$ and $\frac{dT_s}{df_\theta}$, derived from combined and averaged surface fits for dates 12/08/09 and 12/08/16 as predictor for 12cm bed. Known cover fractions were used.

	type	intrcpt	ΔT_a	ΔR_h	ΔP_a	R^2
veg fit	combined 10 16	-0.572	4.257	0.664	-1.799	0.925
	averaged 10 16	-0.644	4.060	0.714	-2.377	
soil fit	combined 10 16	1.598	2.280	0.206	-1.721	0.899
	averaged 10 16	1.378	2.835	0.179	-1.234	

(a) Combined and averaged surface fit coefficients.

day	veg response			soil response		
	std C	bias C	%	std C	bias C	%
120808	1.704	-0.963	39.4	1.171	0.662	39.4
120809	0.560	0.285	97.8	0.420	-0.218	95.6
120810*	0.579	-0.002	95.6	0.538	0.011	95.6
120816*	0.860	0.013	93.3	0.603	0.012	93.3

(b) Cover responses using combined surface fit.

day	veg response			soil response		
	std C	bias C	%	std C	bias C	%
120808	1.597	-0.484	39.4	1.104	0.335	39.4
120809	0.782	0.263	95.5	0.583	-0.197	95.5
120810*	0.904	0.163	88.9	0.796	-0.122	88.9
120816*	0.735	-0.047	97.8	0.523	0.735	97.8

(c) Cover responses using averaged surface fit.

Table 25: Unmixing results using estimated differential coefficients using combined and averaged dates 12/08/10 and 12/08/16 with known cover fractions as predictor for 12cm.

F.3 Individual day surface fits with known land cover fractions.

These tables show the results of applying individual day surface fits to other days.

surf 08		veg response			soil response		
day	std C	bias C	%	std C	bias C	%	
120808*	0.824	-0.003	87.9	0.568	0.008	87.9	
120809	2.696	1.786	44.4	2.092	-1.427	44.4	
120810	2.516	-0.342	53.3	1.974	0.220	53.3	
120816	1.352	0.240	64.4	1.352	-0.121	64.4	

(a) Cover responses using surface fit from 12/08/08.

surf 09		veg response			soil response		
day	std C	bias C	%	std C	bias C	%	
120808	1.414	-1.011	36.4	0.979	0.690	36.4	
120809*	0.523	-0.003	100.0	0.390	-0.003	100.0	
120810	0.581	0.433	95.6	0.546	0.357	95.6	
120816	0.872	-0.569	91.1	0.633	0.437	91.1	

(b) Cover responses using surface fit from 12/08/09.

surf 10		veg response			soil response		
day	std C	bias C	%	std C	bias C	%	
120808	1.485	-0.858	45.5	1.029	0.593	45.5	
120809	0.623	0.515	97.8	0.469	-0.393	97.8	
120810*	0.512	0.000	98.0	0.452	0.004	98.0	
120816	1.000	-0.098	91.1	0.706	0.098	91.1	

(c) Cover responses using surface fit from 12/08/10.

surf 16		veg response			soil response		
day	std C	bias C	%	std C	bias C	%	
120808	1.749	-0.115	39.4	1.209	0.078	39.4	
120809	1.532	-0.006	71.1	1.132	0.002	71.1	
120810	1.598	0.312	66.7	1.357	-0.245	66.7	
120816*	0.617	0.001	100.0	0.449	0.007	100.0	

(d) Cover responses using surface fit from 12/08/16.

Table 26: Unmixing results using estimated differential coefficients, $\frac{dT_v}{df_e}$ and $\frac{dT_s}{df_e}$, derived from individual day surface fits as predictors on other dates for 12cm bed. Used with known cover fractions.

F.4 Results using averaged land cover fractions.

These tables show the results of applying averaged land cover fractions to different types surface fits to estimate the differential coefficients, $\frac{dT_v}{df_\theta}$ and $\frac{dT_s}{df_\theta}$. Asterisks denote when surface coefficients were applied to days from which they were derived.

09	veg response			soil response		
	std C	bias C	%	std C	bias C	%
120809*	0.692	0.050	100.0	0.498	-0.057	100.0
120810	1.134	0.107	82.2	0.650	0.047	97.8
120816	0.544	-0.865	88.9	0.414	0.597	88.9

(a) Cover responses using surface fit from 12/08/09 and averaged fractions.

10	veg response			soil response		
	std C	bias C	%	std C	bias C	%
120809	0.805	0.571	95.6	0.588	-0.453	95.6
120810*	1.222	0.553	82.2	0.732	-0.290	91.1
120816	0.618	-0.399	100.0	0.478	0.251	100.0

(b) Cover responses using surface fit from 12/08/10 and averaged fractions.

16	veg response			soil response		
	std C	bias C	%	std C	bias C	%
120809	1.480	0.054	71.1	1.109	-0.067	71.1
120810	1.610	0.882	62.2	1.115	-0.544	71.1
120816*	0.749	-0.295	95.5	0.507	0.172	95.5

(c) Cover responses using surface fit from 12/08/10 and averaged fractions.

Table 27: Unmixing results using estimated differential coefficients, $\frac{dT_v}{df_\theta}$ and $\frac{dT_s}{df_\theta}$, from individual day surface fits on the remainder days with averaged fractions.

09 10	veg response			soil response		
day	std C	bias C	%	std C	bias C	%
120809*	0.722	0.233	100.0	0.521	-0.196	100.0
120810*	1.138	0.369	86.7	0.658	-0.150	97.8
120816	0.612	-0.500	97.8	0.456	0.326	97.8

(a) Cover responses using surface fit from combined 12/08/09 and 12/08/10.

09 16	veg response			soil response		
day	std C	bias C	%	std C	bias C	%
120809*	0.726	0.170	100.0	0.529	-0.147	100.0
120810	1.077	0.417	84.4	0.613	-0.185	97.8
120816*	0.588	-0.411	97.8	0.425	0.260	97.8

(b) Cover responses using surface fit from combined 12/08/09 and 12/08/16.

10 16	veg response			soil response		
day	std C	bias C	%	std C	bias C	%
120809	0.709	0.345	97.8	0.515	-0.279	100.0
120810*	1.100	0.551	88.9	0.630	-0.286	95.6
120816*	0.605	-0.287	97.8	0.444	0.168	100.0

(c) Cover responses using surface fit from combined 12/08/10 and 12/08/16.

Table 28: Unmixing results using estimated differential coefficients, $\frac{dT_v}{df_\theta}$ and $\frac{dT_s}{df_\theta}$, from two combined day surface fits as predictors, on the remainder day with averaged fractions.

F.5 Results using NDVI land cover fractions.

Graphs and tables for NDVI estimation of vegetation cover fraction are presented below. The scatterplot shows the NDVI responses to different soil moistures. Regression equations follow same order as legend, top to bottom.

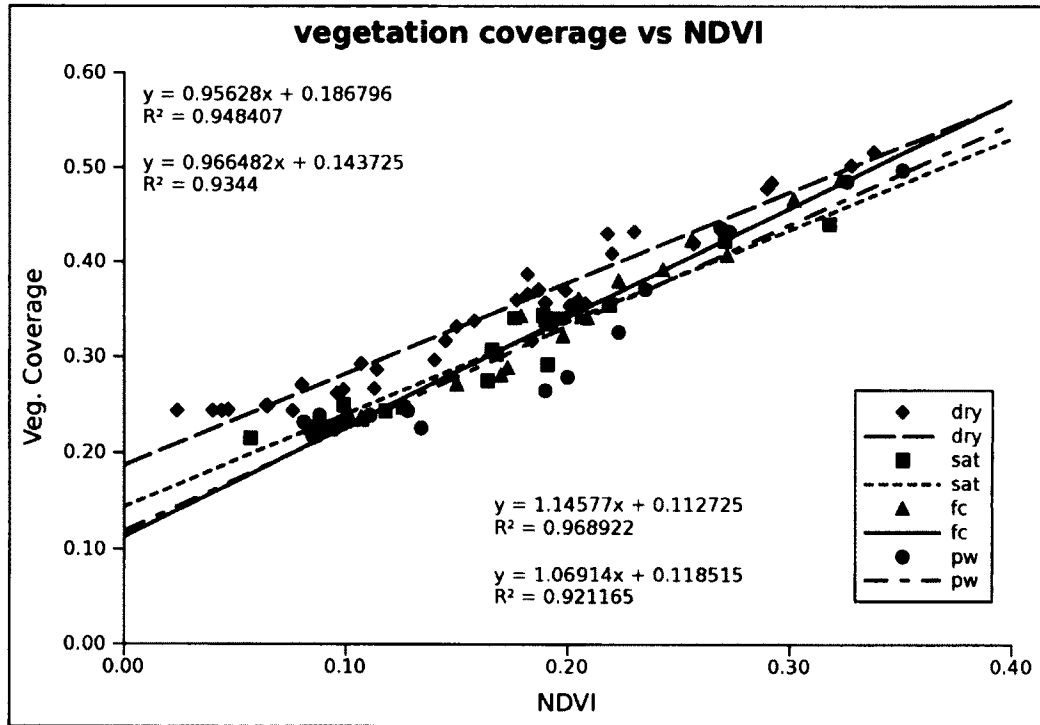


Figure 12: Scatter plot of various soil moistures and NDVI.

09	veg response			soil response		
	day	std C	bias C	%	std C	bias C
120809*	1.184	-0.325	84.4	0.854	0.184	84.4
120810	1.159	-0.641	80.0	0.971	0.515	80.0
120816	0.966	-0.433	91.1	0.577	0.496	88.9

(a) Cover responses using surface fit from 120809.

10	veg response			soil response		
	day	std C	bias C	%	std C	bias C
120809	1.181	0.177	91.1	0.842	-0.209	93.3
120810*	1.145	-0.217	88.9	0.911	0.145	86.7
120816	1.088	-0.054	88.9	0.638	0.261	91.1

(b) Cover responses using surface fit from 120810.

16	veg response			soil response		
	day	std C	bias C	%	std C	bias C
120809	1.998	-0.357	57.8	1.514	0.201	57.8
120810	1.849	0.144	60.0	1.513	-0.089	62.2
120816*	0.832	0.038	95.6	0.483	0.188	97.8

(c) Cover responses using surface fit from 120816.

Table 29: Unmixing results using estimated differential coefficients, $\frac{dT_v}{df_\theta}$ and $\frac{dT_s}{df_\theta}$, from individual day surface fits on the remainder days with NDVI fractions.

09 10	veg response			soil response		
	day	std C	bias C	%	std C	bias C
120809*	1.184	-0.151	84.4	0.851	0.046	86.7
120810*	1.091	-0.393	84.4	0.894	0.301	84.4
120816	1.003	-0.129	91.1	0.588	0.305	95.6

(a) Cover responses using combined surface fit from 12/08/09 and 12/08/10.

09 16	veg response			soil response		
	day	std C	bias C	%	std C	bias C
120809*	1.283	-0.213	86.7	0.940	0.094	86.7
120810	1.150	-0.339	86.7	0.978	0.271	88.9
120816*	0.888	-0.053	95.6	0.520	0.254	97.8

(b) Cover responses using surface fit from combined 12/08/09 and 12/08/16.

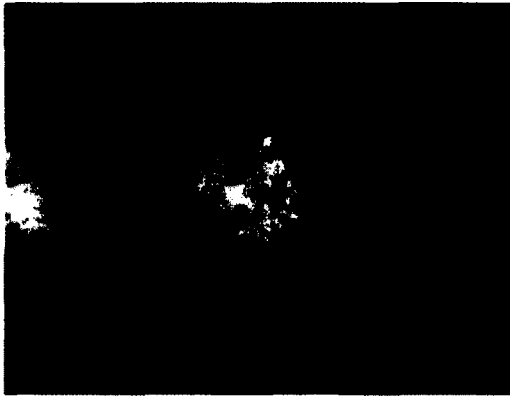
10 16	veg response			soil response		
	day	std C	bias C	%	std C	bias C
120809	1.242	-0.053	86.7	0.902	-0.030	86.7
120810*	1.116	-0.209	91.1	0.922	0.154	91.1
120816*	0.943	0.057	91.1	0.548	0.186	95.6

(c) Cover responses using surface fit from combined 12/08/10 and 12/08/16.

Table 30: Unmixing results using estimated differential coefficients, $\frac{dT_v}{df_\theta}$ and $\frac{dT_s}{df_\theta}$, from two combined day surface fits as predictors, on the remainder day with NDVI fractions.

F.6 NDVI and thermal registered images.

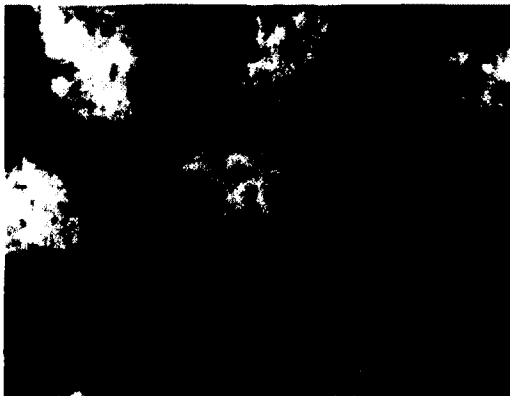
Two registered nadir images and two registered oblique images are shown below.



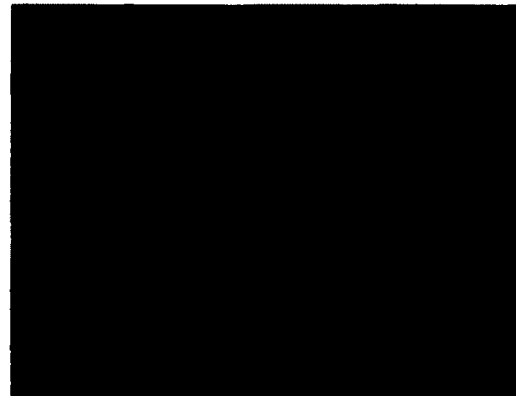
(a) Nadir thermal image.



(b) Nadir NDVI image.



(c) Oblique thermal image.



(d) Oblique NDVI image.

Figure 13: Four images make one sample. Green buffer represents near-infrared band.

G Tabulated results for 24 cm bed.

Tables showing results of applying different hyper-surface fits to the mixed data of 24 cm bed are presented below. Hyper-surfaces are henceforth called “surfaces” for simplicity. Sample day surface coefficients can be found in Table (9) while combined and average surface coefficients are given below when used.

G.1 Near instantaneous sampling results and metrics used.

The following tables show the results of applying averaged differential coefficients, $\frac{dT_v}{df_\theta}$ and $\frac{dT_s}{df_\theta}$, to all near instantaneous samples for both land covers. The calculated temperatures are then compared to the mixed temperature values. Table headings are: t_s is the sensed cover temperature, t_m is the mixed temperature; t_c is the calculated temperature from unmixing; a is the absolute difference of the sensed temperature, t_s , and the mixed temperature, t_m ; and b is the absolute difference of the sensed temperature, t_s , and the calculated temperature t_c . Dividing b into a gives a measure of performance. If the calculated temperature is closer to the sensed temperature than is the mixed temperature, then a “1” is assigned to the right most column. Bottom row indicates the percentage of samples that performed better than the mixed temperature.

t_{sensed}	t_{mixed}	$a = abs(t_{sensed} - t_{mixed})$	t_{calc}	$b = abs(t_{sensed} - t_{calc})$	a/b	
296.515	295.814	0.701	296.454	0.061	11.492	1
297.687	296.895	0.792	297.696	0.009	88.000	1
299.674	298.526	1.148	299.869	0.195	5.887	1
300.176	299.178	0.998	300.044	0.132	7.561	1
302.262	300.591	1.671	302.029	0.233	7.172	1
302.779	301.186	1.593	303.279	0.500	3.186	1
301.280	299.964	1.316	301.701	0.421	3.126	1
296.230	295.742	0.488	296.272	0.042	11.619	1
297.786	296.928	0.858	297.456	0.330	2.600	1
297.015	296.296	0.719	296.898	0.117	6.145	1
297.066	296.365	0.701	296.573	0.493	1.422	1
301.244	299.737	1.507	302.278	1.034	1.457	1
300.953	299.573	1.380	300.843	0.110	12.545	1
299.164	298.017	1.147	299.341	0.177	6.480	1
298.432	297.366	1.066	298.012	0.420	2.538	1
297.594	296.852	0.742	297.597	0.003	247.333	1
296.987	296.178	0.809	297.511	0.524	1.544	1
298.304	297.384	0.920	298.593	0.289	3.183	1
298.721	297.771	0.950	298.694	0.027	35.185	1
299.309	298.056	1.253	299.086	0.223	5.619	1
299.748	298.520	1.228	299.749	0.001	1228.000	1
299.799	298.616	1.183	299.522	0.277	4.271	1
300.051	298.986	1.065	299.700	0.351	3.034	1
299.927	299.182	0.745	300.560	0.633	1.177	1
294.370	293.863	0.507	293.936	0.434	1.168	1
294.877	294.399	0.478	294.965	0.088	5.432	1
295.812	295.250	0.562	295.306	0.506	1.111	1
297.402	296.643	0.759	297.285	0.117	6.487	1
299.933	298.967	0.966	299.851	0.082	11.780	1
299.879	299.067	0.812	299.847	0.032	25.375	1
299.024	298.182	0.842	298.998	0.026	32.385	1
299.570	298.915	0.655	299.585	0.015	43.667	1
300.538	299.629	0.909	300.582	0.044	20.659	1
300.318	299.521	0.797	300.518	0.200	3.985	1
296.290	295.604	0.686	295.982	0.308	2.227	1
298.300	297.356	0.944	298.401	0.101	9.347	1
299.507	298.514	0.993	299.260	0.247	4.020	1
299.786	298.905	0.881	299.922	0.136	6.478	1
297.521	296.810	0.711	297.297	0.224	3.174	1
297.725	296.983	0.742	297.608	0.117	6.342	1
298.319	297.626	0.693	298.492	0.173	4.006	1
						100.0%

Table 31: Vegetation cover results for near instantaneous samples with averaged $\frac{dT_v}{df_\theta}$ and $\frac{dT_s}{df_\theta}$ for the 24cm bed.

t_{sensed}	t_{mixed}	$a = abs(t_{sensed} - t_{mixed})$	t_{calc}	$b = abs(t_{sensed} - t_{calc})$	a/b	
293.502	295.814	2.312	293.706	0.204	11.333	1
294.191	296.895	2.704	294.159	0.032	84.500	1
295.336	298.526	3.190	294.779	0.557	5.727	1
295.999	299.178	3.179	296.426	0.427	7.445	1
296.332	300.591	4.259	296.940	0.608	7.005	1
296.647	301.186	4.539	295.165	1.482	3.063	1
296.213	299.964	3.751	294.972	1.241	3.023	1
294.423	295.742	1.319	294.306	0.117	11.274	1
295.016	296.928	1.912	295.757	0.741	2.580	1
294.625	296.296	1.671	294.898	0.273	6.121	1
294.937	296.365	1.428	295.946	1.009	1.415	1
296.751	299.737	2.986	294.623	2.128	1.403	1
296.710	299.573	2.863	296.943	0.233	12.288	1
295.683	298.017	2.334	295.314	0.369	6.325	1
295.147	297.366	2.219	296.030	0.883	2.513	1
294.795	296.852	2.057	294.786	0.009	228.556	1
294.471	296.178	1.707	293.340	1.131	1.509	1
294.807	297.384	2.577	293.977	0.830	3.105	1
295.264	297.771	2.507	295.336	0.072	34.819	1
295.348	298.056	2.708	295.838	0.490	5.527	1
295.675	298.52	2.845	295.671	0.004	711.250	1
295.906	298.616	2.710	296.551	0.645	4.202	1
296.267	298.986	2.719	297.175	0.908	2.994	1
296.772	299.182	2.410	294.659	2.113	1.141	1
292.805	293.863	1.058	293.713	0.908	1.165	1
292.879	294.399	1.520	292.597	0.282	5.390	1
293.509	295.250	1.741	295.077	1.568	1.110	1
294.449	296.643	2.194	294.792	0.343	6.397	1
296.344	298.967	2.623	296.570	0.226	11.606	1
296.805	299.067	2.262	296.897	0.092	24.587	1
296.124	298.182	2.058	296.189	0.065	31.662	1
296.615	298.915	2.300	296.561	0.054	42.593	1
296.973	299.629	2.656	296.842	0.131	20.275	1
297.012	299.521	2.509	296.370	0.642	3.908	1
293.773	295.604	1.831	294.602	0.829	2.209	1
294.867	297.356	2.489	294.594	0.273	9.117	1
295.697	298.514	2.817	296.408	0.711	3.962	1
296.311	298.905	2.594	295.899	0.412	6.296	1
294.867	296.810	1.943	295.485	0.618	3.144	1
295.200	296.983	1.783	295.484	0.284	6.278	1
295.877	297.626	1.749	295.433	0.444	3.939	1
						100.0%

Table 32: Soil cover results for near instantaneous samples with averaged $\frac{dT_s}{df_o}$ and $\frac{dT_a}{df_o}$ for the 24cm bed.

G.2 Combined and averaged surface fits with known cover fractions.

The following tables show the results of applying combined and averaged surface fits to estimate the differential coefficients, $\frac{dT_v}{df_\theta}$ and $\frac{dT_s}{df_\theta}$, to the mixed data with known cover fractions. Asterisks denote when surface coefficients were applied to days from which they were partially derived.

	type	intrcpt	ΔT_a	ΔR_h	ΔP_a	R^2
veg fit	combined 11 12	0.977	3.230	-0.673	-0.204	0.932
	averaged 11 12	1.406	3.994	0.168	-1.111	
soil fit	combined 11 12	2.660	2.400	0.349	-0.793	0.895
	averaged 11 12	2.863	2.414	0.506	-1.199	

(a) Combined and averaged surface fit coefficients.

day	veg response			soil response		
	std C	bias C	%	std C	bias C	%
120811*	0.450	0.191	96.4	1.198	-0.160	100.0
120812*	0.758	-0.792	55.6	1.718	1.524	57.8
120813	0.735	0.284	75.0	1.655	-0.850	58.3
120814	0.834	0.420	63.5	2.071	-0.803	67.3
120815	0.711	0.324	64.3	1.968	-0.808	64.3

(b) Cover responses using combined surface fit.

day	veg response			soil response		
	std C	bias C	%	std C	bias C	%
120811*	0.466	-0.110	96.4	1.392	0.365	96.4
120812*	0.770	0.060	91.1	1.664	-0.127	86.7
120813	0.416	0.041	100.0	1.025	-0.097	100.0
120814	0.566	0.010	76.9	1.713	-0.078	76.9
120815	0.467	0.114	89.2	1.231	-0.273	85.7

(c) Cover responses using averaged surface fit.

Table 33: Unmixing results using estimated differential coefficients, $\frac{dT_v}{df_\theta}$ and $\frac{dT_s}{df_\theta}$, derived from combined and averaged surface fits for dates 12/08/11 and 12/08/12 as predictor. Known cover fractions were used.

	type	intrcpt	ΔT_a	ΔR_h	ΔP_a	R^2
veg fit	combined 12 13	1.206	4.082	-0.206	-1.000	0.937
	averaged 12 13	1.114	4.938	-0.193	-0.287	
soil fit	combined 12 13	2.594	2.916	0.587	-1.284	0.906
	averaged 12 13	2.585	2.920	0.518	-1.228	

(a) Combined and averaged surface fit coefficients.

day	veg response			soil response		
	std C	bias C	%	std C	bias C	%
120811	0.582	-0.033	100.0	1.504	0.423	100.0
120812*	0.917	-0.846	48.9	2.105	1.656	48.9
120813*	0.594	0.041	88.9	1.260	-0.197	97.2
120814	0.808	0.245	66.0	1.984	-0.336	75.5
120815	0.607	0.264	71.4	1.682	-0.643	71.4

(b) Cover responses using combined surface fit.

day	veg response			soil response		
	std C	bias C	%	std C	bias C	%
120811	0.801	-0.397	78.6	2.348	1.165	78.6
120812*	0.675	-0.101	90.9	1.650	0.173	90.9
120813*	0.354	0.056	100.0	0.877	-0.174	100.0
120814	0.879	-0.307	55.8	2.628	0.804	55.8
120815	1.039	0.354	53.6	2.772	-0.899	53.6

(c) Cover responses using averaged surface fit.

Table 34: Unmixing results using estimated differential coefficients, $\frac{dT_v}{df_\theta}$ and $\frac{dT_s}{df_\theta}$, derived from combined and averaged surface fits for dates 12/08/12 and 12/08/13 as predictor. Known cover fractions were used.

	type	intrcpt	ΔT_a	ΔR_h	ΔP_a	R^2
veg fit	combined 13 14	1.246	2.798	0.252	-2.276	0.892
	averaged 13 14	0.979	4.859	0.542	-2.090	
soil fit	combined 13 14	2.131	1.877	0.235	-2.131	0.910
	averaged 13 14	2.182	2.552	0.511	-2.206	

(a) Combined and averaged surface fit coefficients.

day	veg response			soil response		
	std C	bias C	%	std C	bias C	%
120811	0.429	0.232	96.4	1.151	-0.269	100.0
120812	0.455	-0.804	64.4	1.069	1.564	71.1
120813*	0.528	-0.015	91.7	1.191	-0.046	94.4
120814*	0.659	0.524	61.5	1.631	-1.069	75.0
120815	0.428	-0.097	85.7	1.014	0.311	85.7

(b) Cover responses using combined surface fit.

day	veg response			soil response		
	std C	bias C	%	std C	bias C	%
120811	0.619	-0.324	92.6	1.781	0.945	92.6
120812	0.669	-0.006	86.7	1.510	-0.013	86.7
120813*	0.399	-0.144	97.2	1.085	0.418	97.2
120814*	0.656	-0.227	67.3	1.971	0.620	67.3
120815	0.388	0.061	96.4	1.047	-0.140	96.4

(c) Cover responses using averaged surface fit.

Table 35: Unmixing results using estimated differential coefficients, $\frac{dT_v}{df_\theta}$ and $\frac{dT_s}{df_\theta}$, derived from combined and averaged surface fits for dates 12/08/13 and 12/08/14 as predictor. Known cover fractions were used.

	type	intrcpt	ΔT_a	ΔR_h	ΔP_a	R^2
veg fit	combined 14 15	0.997	3.180	0.298	-1.944	0.937
	averaged 14 15	0.810	3.082	0.418	-2.458	
soil fit	combined 14 15	1.991	1.761	0.188	-2.269	0.924
	averaged 14 15	2.012	1.053	0.006	-1.932	

(a) Combined and averaged surface fit coefficients.

day	veg response			soil response		
	std C	bias C	%	std C	bias C	%
120811	0.411	0.254	96.4	1.098	-0.327	100.0
120812	0.468	-0.752	68.9	1.060	1.430	73.3
120813	0.529	0.046	91.7	1.183	-0.207	94.4
120814*	0.653	0.549	57.7	1.607	-1.135	76.9
120815*	0.360	-0.002	100.0	0.846	0.065	100.0

(b) Cover responses using combined surface fit.

day	veg response			soil response		
	std C	bias C	%	std C	bias C	%
120811	0.498	0.135	100.0	1.405	-0.357	100.0
120812	1.248	0.152	66.7	2.709	-0.280	64.4
120813	0.438	0.089	100.0	1.141	-0.188	100.0
120814*	0.504	0.189	90.4	1.480	-0.574	88.5
120815*	0.402	-0.159	85.7	1.050	0.390	85.7

(c) Cover responses using averaged surface fit.

Table 36: Unmixing results using estimated differential coefficients, $\frac{dT_v}{df_\theta}$ and $\frac{dT_s}{df_\theta}$, from combined and averaged surface fits for dates 12/08/14 and 12/08/15 as predictor. Known cover fractions were used.

13 14 15	veg response			soil response		
day	std C	bias C	%	std C	bias C	%
120811	0.468	-0.098	96.4	1.382	0.320	96.4
120812	0.810	0.081	86.7	1.755	-0.161	86.7

(a) Cover responses using surface fit from averaged 12/08/13, 12/08/14, 12/08/15.

12 13 14	veg response			soil response		
day	std C	bias C	%	std C	bias C	%
120811	0.571	-0.275	92.6	1.652	0.809	92.6
120815	0.530	0.129	82.1	1.411	-0.306	78.6

(b) Cover responses using surface fit from averaged 12/08/12, 12/08/13, 12/08/14.

11 12 13	veg response			soil response		
day	std C	bias C	%	std C	bias C	%
120814	0.672	-0.140	67.3	2.032	0.348	67.3
120814a	0.578	0.039	79.1	1.779	-0.178	79.1
120815	0.658	0.224	75.0	1.742	-0.555	75.0

(c) Cover responses using surface fit from averaged 12/08/11, 12/08/12, 12/08/13.

12 13 15	veg response			soil response		
day	std C	bias C	%	std C	bias C	%
120811	0.464	-0.064	100.0	1.360	-0.064	100.0
120814	0.678	-0.077	70.4	2.063	0.161	70.4
120814a	0.571	0.111	83.7	1.771	-0.3945	83.7

(d) Cover responses using surface fit from averaged 12/08/12, 12/08/13, 12/08/15.

12 14 15	veg response			soil response		
day	std C	bias C	%	std C	bias C	%
120811	0.427	0.013	100.0	1.242	0.003	100.0
120813	0.401	0.100	100.0	1.000	-0.401	100.0

(e) Cover responses using surface fit from averaged 12/08/12, 12/08/14, 12/08/15.

Table 37: Unmixing results using estimated differential coefficients, $\frac{dT_v}{df_\theta}$ and $\frac{dT_s}{df_\theta}$, from an averaged fit of three other days as predictor on the remainder days. Used with known cover fractions.

day	veg response			soil response		
	std C	bias C	%	std C	bias C	%
120811	0.483	-0.131	96.4	1.436	0.418	96.4
120812	0.860	0.105	82.2	1.847	-0.212	80.0
120813	0.416	0.065	100.0	1.047	-0.142	100.0
120814	0.596	0.005	78.8	1.815	-0.038	76.9
120814a	0.528	0.148	86.0	1.622	-0.492	83.7
120815	0.418	0.088	92.9	1.114	-0.207	92.9

Table 38: Unmixing results using estimated differential coefficients, $\frac{dT_v}{df_\theta}$ and $\frac{dT_s}{df_\theta}$, from an averaged fit of four other days as predictor. Used with known cover fractions.

G.3 Individual day surface fits with known land cover fractions.

These tables show the results of applying individual day surface fits to other days.

surf 11	veg response			soil response		
day	std C	bias C	%	std C	bias C	%
120811*	0.421	0.010	100.0	1.217	0.014	100.0
120812	1.063	0.177	77.8	2.277	-0.370	77.8
120813	0.477	-0.035	100.0	1.255	0.146	100.0
120814	0.536	0.193	82.3	1.591	-0.598	82.3
120815	0.549	-0.032	78.6	1.464	0.063	78.6

(a) Cover responses using surface fit from 12/08/11.

surf 12	veg response			soil response		
day	std C	bias C	%	std C	bias C	%
120811	0.540	-0.175	96.4	1.587	0.533	96.4
120812*	0.591	-0.015	91.1	1.355	-0.011	91.1
120813	0.431	0.118	100.0	1.087	-0.349	100.0
120814	0.735	-0.171	65.4	2.223	0.424	65.4
120815	0.915	0.264	53.6	2.430	-0.655	53.6

(b) Cover responses using surface fit from 12/08/12.

surf 13	veg response			soil response		
day	std C	bias C	%	std C	bias C	%
120811	1.038	-0.561	71.4	2.991	1.606	71.4
120812	0.864	-0.116	84.1	2.117	0.156	84.1
120813*	0.322	-0.006	100.0	0.801	-0.002	100.0
120814	1.053	-0.410	53.9	3.099	1.073	54.9
120815	1.168	0.445	53.6	3.131	-1.147	53.6

(c) Cover responses using surface fit from 12/08/13.

surf 14	veg response			soil response		
day	std C	bias C	%	std C	bias C	%
120811	0.533	-0.184	100.0	1.531	0.566	100.0
120812	1.155	0.053	71.1	2.508	-0.084	71.1
120813	0.570	-0.283	83.3	1.669	0.831	83.3
120814*	0.444	0.009	96.4	1.337	-0.020	96.4
120815	0.768	-0.318	71.4	1.992	0.766	71.4

(d) Cover responses using surface fit from 12/08/14.

surf 15	veg response			soil response		
day	std C	bias C	%	std C	bias C	%
120811	0.612	0.448	96.4	1.731	-1.282	96.4
120812	1.411	0.241	60.0	3.093	-0.478	60.0
120813	0.484	0.457	83.3	1.227	-1.218	80.6
120814	0.611	0.382	78.8	1.822	-1.172	76.9
120815*	0.126	-0.001	100.0	0.343	0.000	100.0

(e) Cover responses using surface fit from 12/08/15.

Table 39: Unmixing results using estimated differential coefficients, $\frac{dT_v}{df_e}$ and $\frac{dT_s}{df_e}$, from individual day surface fits as predictors on other dates. Used with known cover fractions.

G.4 Results using averaged land cover fractions.

These tables show the results of applying averaged land cover fractions to different types surface fits to estimate the differential coefficients, $\frac{dT_v}{df_\theta}$ and $\frac{dT_s}{df_\theta}$. Asterisks denote when surface coefficients were applied to days from which they were derived.

surf 11	veg response			soil response		
day	std C	bias C	%	std C	bias C	%
120811*	0.368	0.281	100.0	0.990	-0.399	100.0
120812	0.463	-0.660	82.2	1.005	1.195	82.2
120813	0.539	-0.025	91.7	1.271	-0.023	97.2
120814	0.794	0.700	51.9	2.027	-1.552	65.3
120815	0.640	0.071	71.4	1.624	-0.141	71.4

(a) Cover responses using surface fit from 12/08/11.

surf 12	veg response			soil response		
day	std C	bias C	%	std C	bias C	%
120811	0.562	0.023	100.0	1.484	0.285	100.0
120812*	0.900	-0.843	46.7	2.061	1.649	51.1
120813	0.714	0.159	80.6	1.593	-0.514	94.4
120814	0.871	0.311	61.5	2.156	-0.516	65.4
120815	0.806	0.341	64.3	2.229	-0.860	60.7

(b) Cover responses using surface fit from 12/08/12.

surf 13	veg response			soil response		
day	std C	bias C	%	std C	bias C	%
120811	1.048	-0.321	71.4	2.728	1.160	71.4
120812	1.490	-0.824	84.1	3.605	1.547	84.1
120813*	0.590	0.027	100.0	1.218	-0.159	100.0
120814	1.096	0.013	53.9	2.749	0.239	57.7
120815	1.054	0.520	53.6	2.908	-1.357	53.6

(c) Cover responses using surface fit from 12/08/13.

surf 14	veg response			soil response		
day	std C	bias C	%	std C	bias C	%
120811	0.523	0.077	100.0	1.378	0.146	100.0
120812	0.585	-0.782	66.7	1.387	1.503	68.9
120813	0.549	-0.281	88.8	1.399	0.649	88.8
120814*	0.615	0.488	67.3	1.524	-0.970	82.7
120815	0.886	-0.207	67.9	2.203	0.568	67.9

(d) Cover responses using surface fit from 12/08/14.

surf 15	veg response			soil response		
day	std C	bias C	%	std C	bias C	%
120811	0.595	0.743	82.1	1.668	-1.673	92.9
120812	0.519	-0.615	73.3	1.454	1.067	77.8
120813	0.702	0.481	72.2	1.628	-1.379	80.6
120814	0.845	0.906	48.1	2.195	-2.111	55.8
120815*	0.242	0.101	100.0	0.509	-0.203	100.0

(e) Cover responses using surface fit from 120813 with averaged fraction.

Table 40: Unmixing results using estimated differential coefficients, $\frac{dT_v}{df_\theta}$ and $\frac{dT_s}{df_\theta}$, from individual day surface fits as predictors on other dates. Used with averaged cover fractions.

13 14 15	veg response			soil response		
day	std C	bias C	%	std C	bias C	%
120811	0.425	0.168	100.0	1.121	-0.095	100.0
120812	0.591	-0.740	66.7	1.292	1.400	68.9

(a) Cover responses using surface fit from averaged 12/08/13, 12/08/14, 12/08/15.

12 13 14	veg response			soil response		
day	std C	bias C	%	std C	bias C	%
120811	0.595	-0.075	100.0	1.557	0.548	100.0
120815	0.444	0.217	85.7	1.234	-0.511	82.1

(b) Cover responses using surface fit from averaged 12/08/12, 12/08/13, 12/08/14.

11 12 13	veg response			soil response		
day	std C	bias C	%	std C	bias C	%
120814	0.789	0.343	61.5	1.936	-0.594	73.1
120815	0.562	0.309	75.0	1.563	-0.761	75.0

(c) Cover responses using surface fit from averaged 12/08/11, 12/08/12, 12/08/13.

12 13 15	veg response			soil response		
day	std C	bias C	%	std C	bias C	%
120811	0.475	0.150	96.4	1.255	-0.051	100.0
120814	0.795	0.411	61.5	1.962	-0.777	61.5

(d) Cover responses using surface fit from averaged 12/08/12, 12/08/13, 12/08/15.

12 14 15	veg response			soil response		
day	std C	bias C	%	std C	bias C	%
120811	0.371	0.284	96.4	0.999	-0.407	100.0
120813	0.571	0.121	100.0	1.263	-0.408	91.7

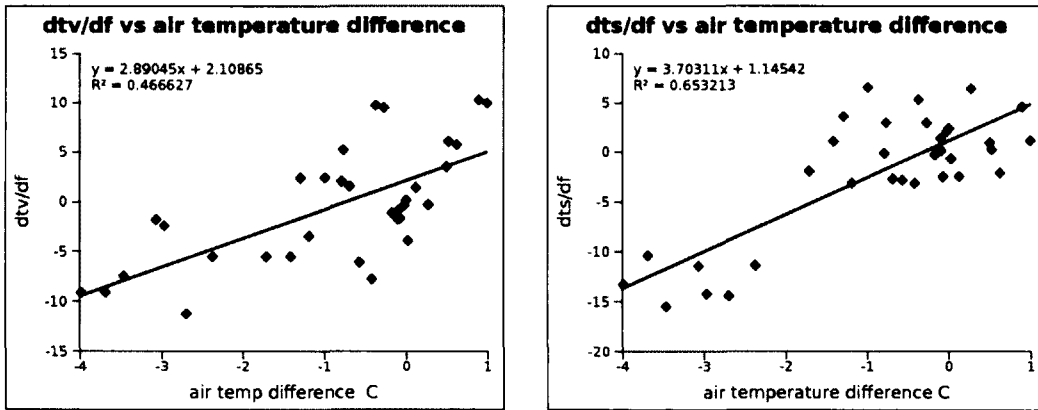
(e) Cover responses using surface fit from averaged 12/08/12, 12/08/14, 12/08/15.

Table 41: Unmixing results using estimated differential coefficients, $\frac{dT_v}{df_\theta}$ and $\frac{dT_s}{df_\theta}$, from an averaged fit of three other days as predictor on the remainder days. Used with averaged cover fractions.

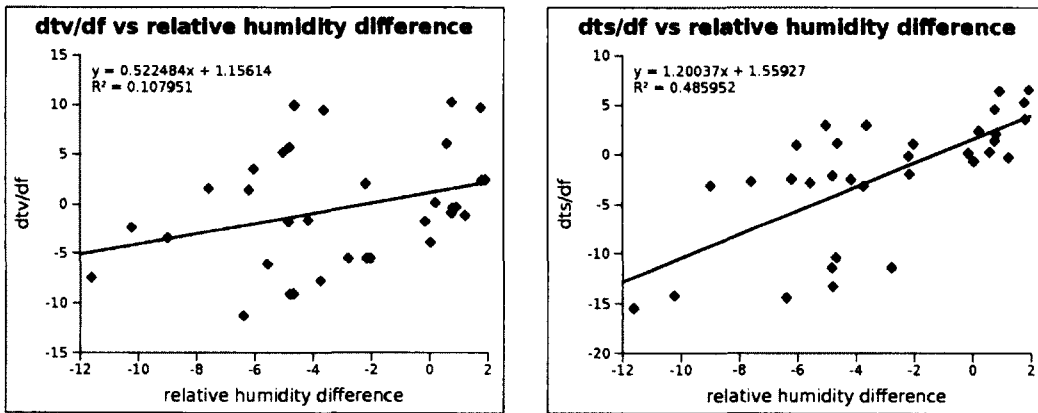
day	veg response			soil response		
	std C	bias C	%	std C	bias C	%
120811	0.434	0.132	96.4	1.144	-0.000	100.0
120812	0.534	-0.720	84.4	1.142	1.349	75.6
120813	0.558	0.085	88.9	1.246	-0.3114	94.4
120814	0.747	0.489	59.6	1.837	-0.980	73.1
120815	0.562	0.309	75.0	1.563	-0.761	75.0

Table 42: Unmixing results using estimated differential coefficients, $\frac{dT_v}{df_\theta}$ and $\frac{dT_s}{df_\theta}$, from an averaged fit of four other days as predictor. Used with averaged cover fractions.

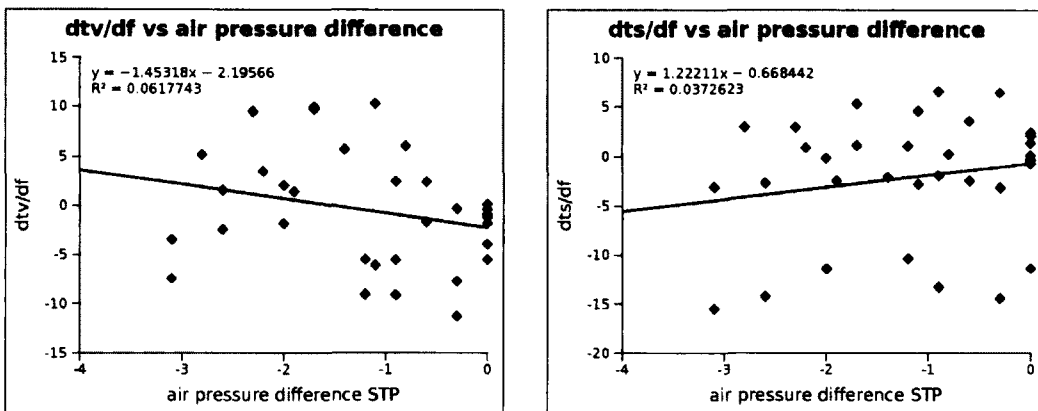
H Environmental correlation graphs of $\frac{dT_o}{df_o}$ for 12cm bed.



(a) $\frac{dT_v}{df_o}, \frac{dT_s}{df_o}$ correlation with air temperature differences.

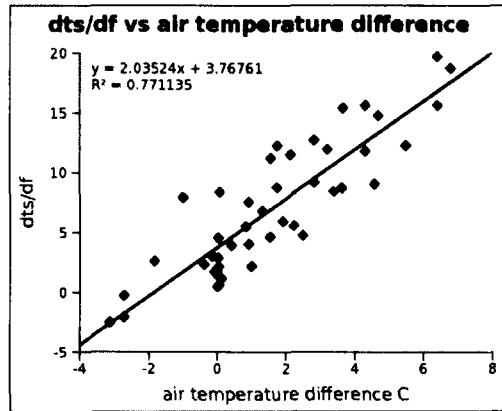
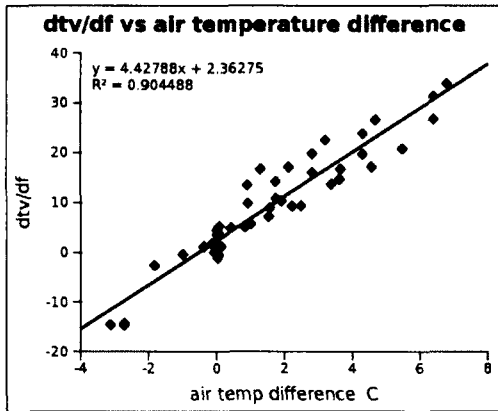


(b) $\frac{dT_v}{df_o}, \frac{dT_s}{df_o}$ correlation with relative humidity differences.

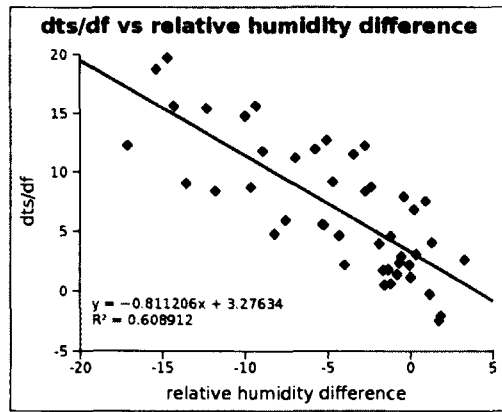
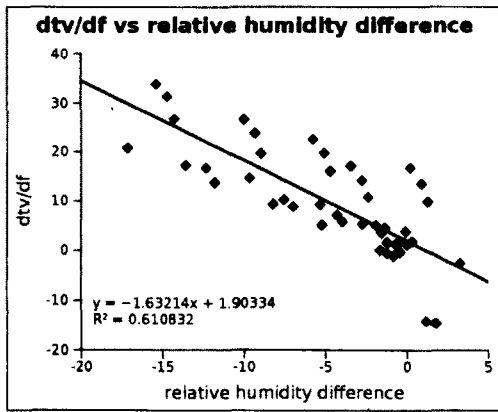


(c) $\frac{dT_v}{df_o}, \frac{dT_s}{df_o}$ correlation with air pressure differences.

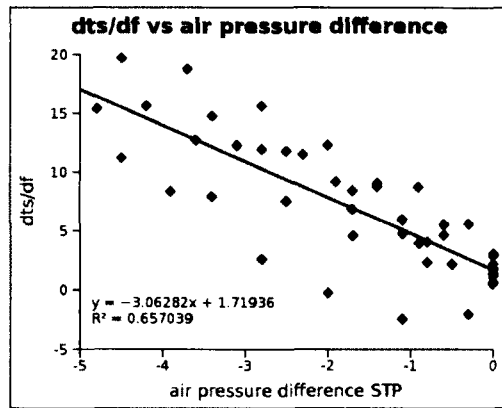
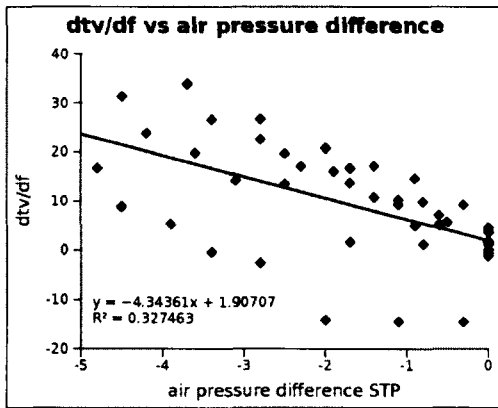
Figure 14: Environmental correlation graphs for 12/08/08 and 12cm bed.



(a) $\frac{dT_v}{df_\theta}, \frac{dT_s}{df_\theta}$ correlation with air temperature differences.

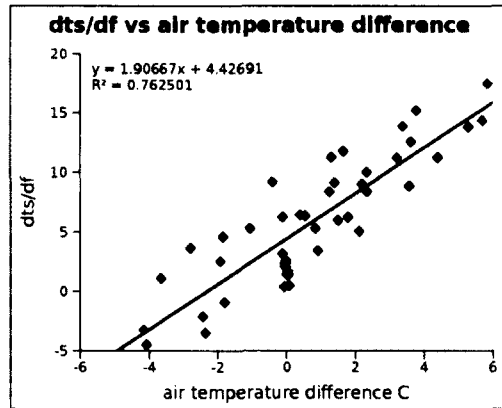
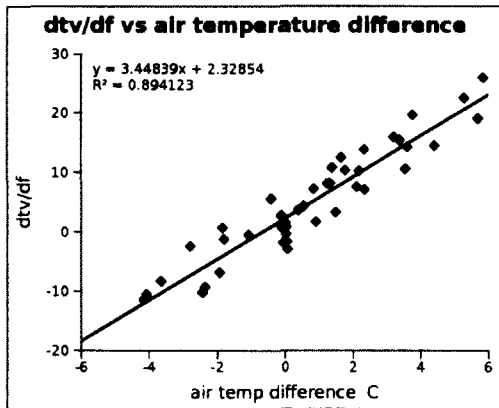


(b) $\frac{dT_v}{df_\theta}, \frac{dT_s}{df_\theta}$ correlation with relative humidity differences.

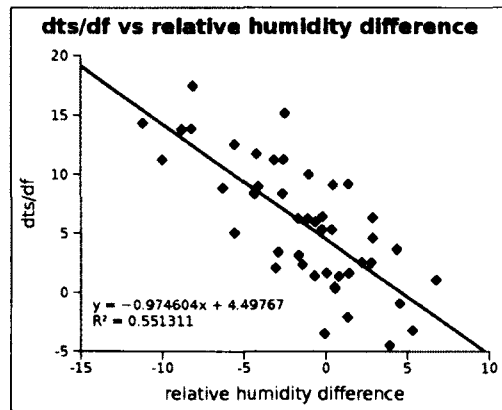
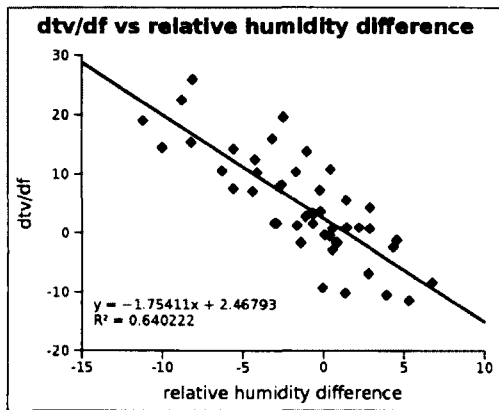


(c) $\frac{dT_v}{df_\theta}, \frac{dT_s}{df_\theta}$ correlation with air pressure differences.

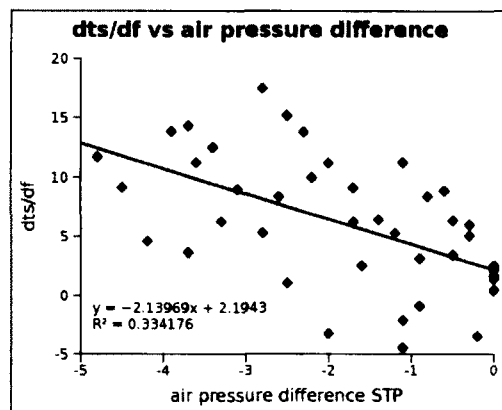
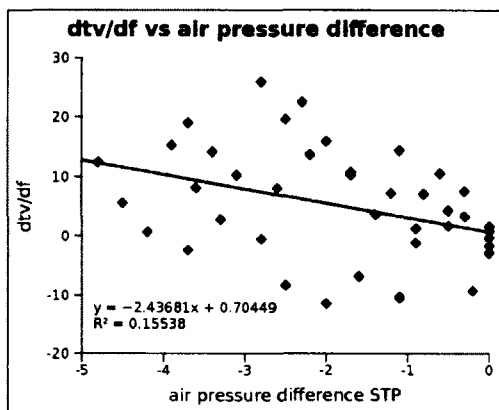
Figure 15: Environmental correlation graphs for 12/08/09 and 12cm bed.



(a) $\frac{dT_v}{df_\theta}, \frac{dT_s}{df_\theta}$ correlation with air temperature differences.

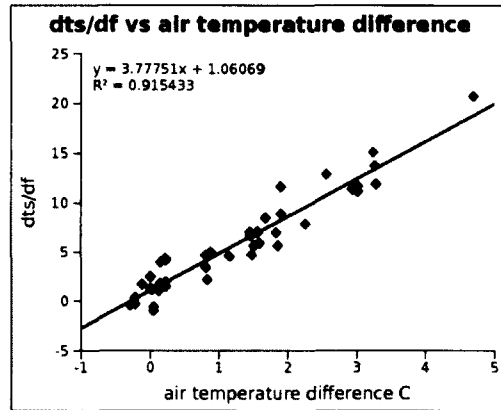
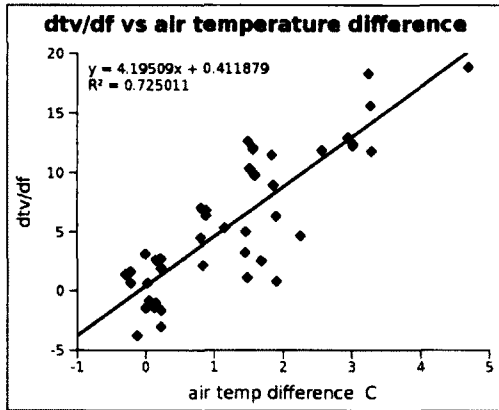


(b) $\frac{dT_v}{df_\theta}, \frac{dT_s}{df_\theta}$ correlation with relative humidity differences.

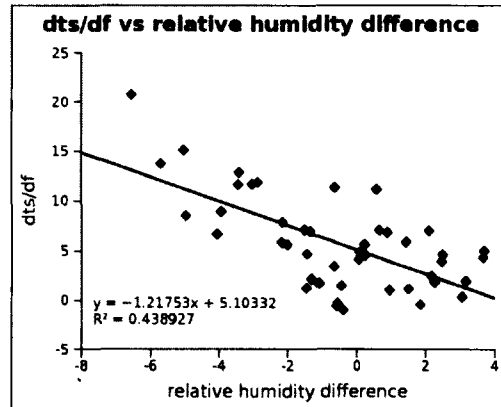
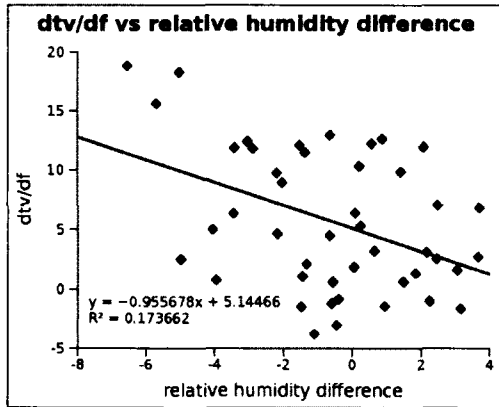


(c) $\frac{dT_v}{df_\theta}, \frac{dT_s}{df_\theta}$ correlation with air pressure differences.

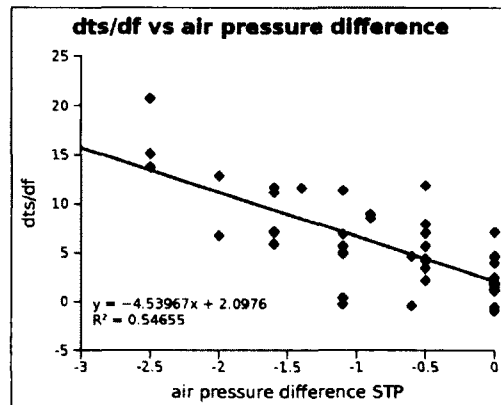
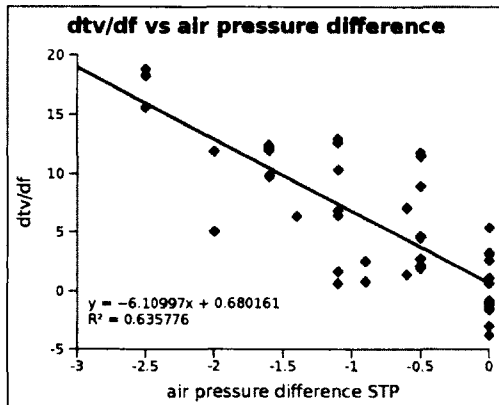
Figure 16: Environmental correlation graphs for 12/08/10 and 12cm bed.



(a) $\frac{dT_v}{df_\theta}, \frac{dT_s}{df_\theta}$ correlation with air temperature differences.

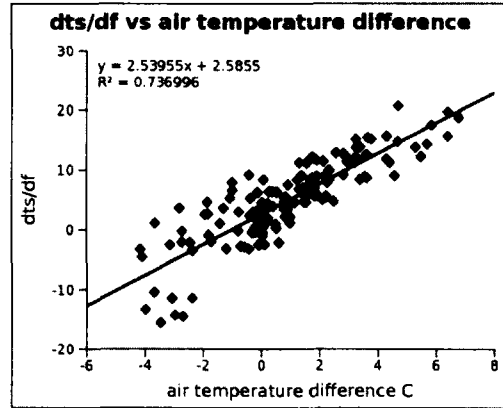
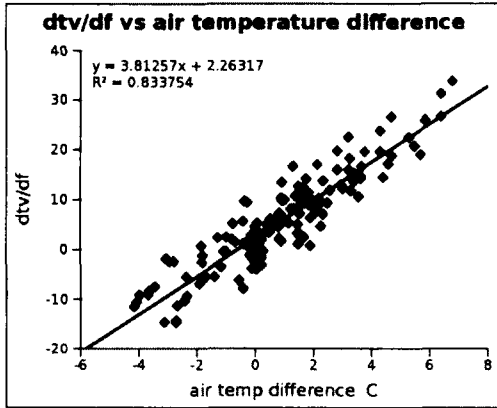


(b) $\frac{dT_v}{df_\theta}, \frac{dT_s}{df_\theta}$ correlation with relative humidity differences.

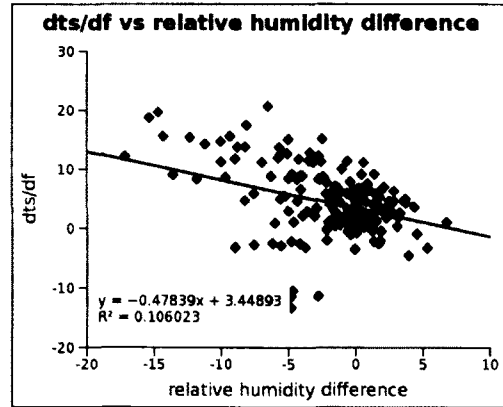
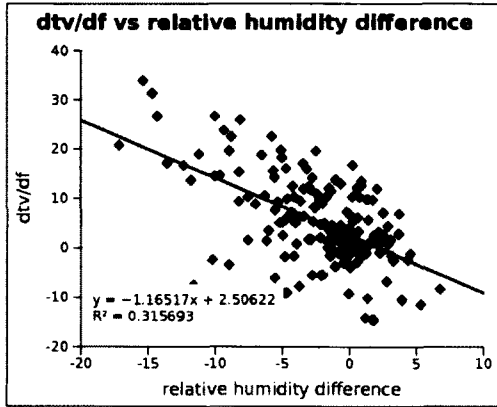


(c) $\frac{dT_v}{df_\theta}, \frac{dT_s}{df_\theta}$ correlation with air pressure differences.

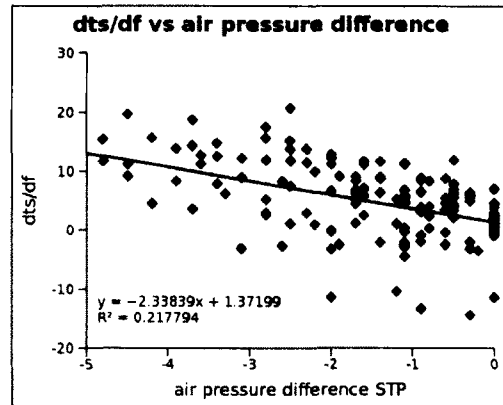
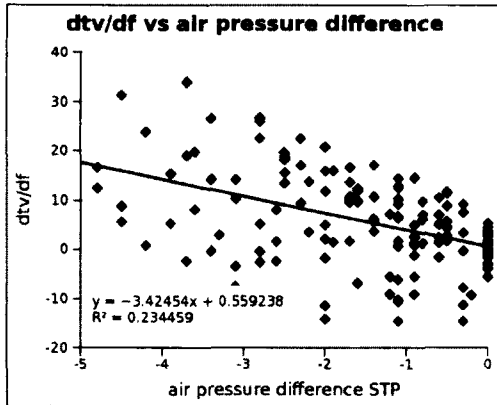
Figure 17: Environmental correlation graphs for 12/08/16 and 12cm bed.



(a) $\frac{dT_v}{df_\theta}, \frac{dT_s}{df_\theta}$ correlation with air temperature differences.



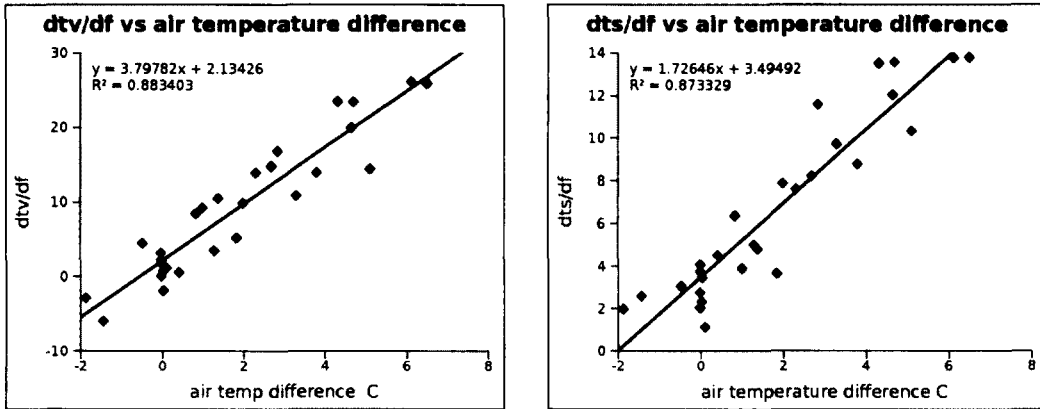
(b) $\frac{dT_v}{df_\theta}, \frac{dT_s}{df_\theta}$ correlation with relative humidity differences.



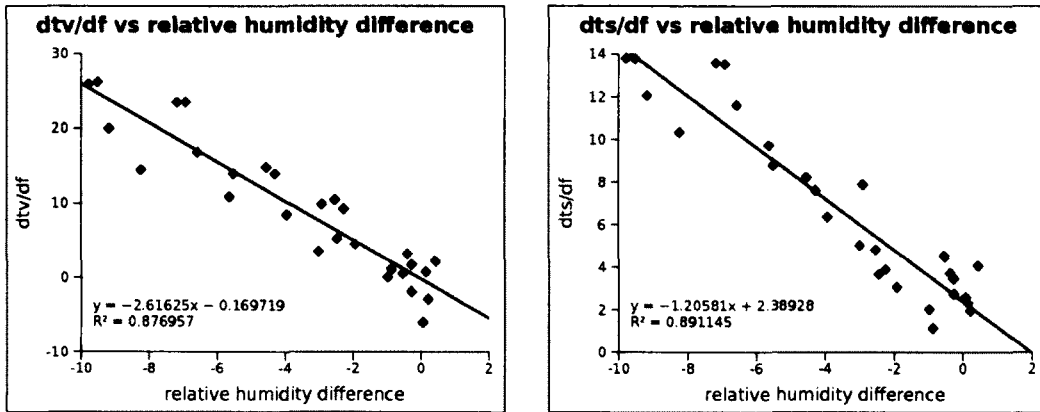
(c) $\frac{dT_v}{df_\theta}, \frac{dT_s}{df_\theta}$ correlation with air pressure differences.

Figure 18: Environmental correlation graphs for all sample days and 12cm bed.

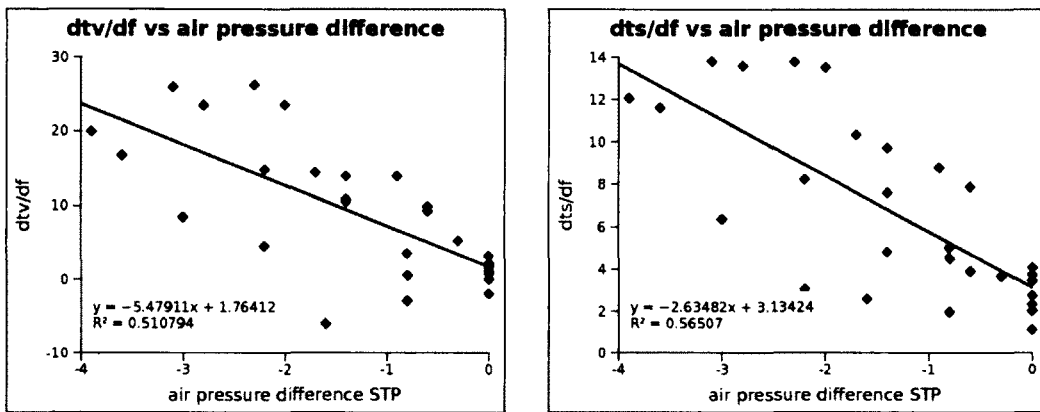
I Environmental correlation graphs of $\frac{dT_o}{df_o}$ for 24cm bed.



(a) $\frac{dT_v}{df_o}, \frac{dT_s}{df_o}$ correlation with air temperature differences.

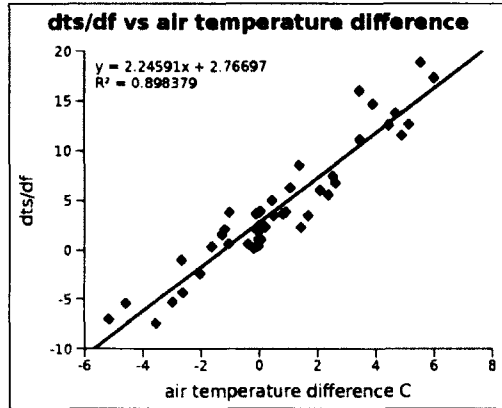
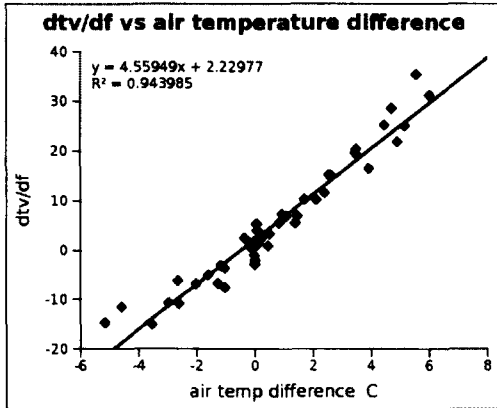


(b) $\frac{dT_v}{df_o}, \frac{dT_s}{df_o}$ correlation with relative humidity differences.

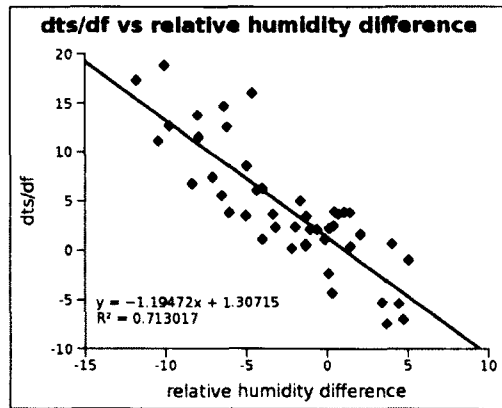
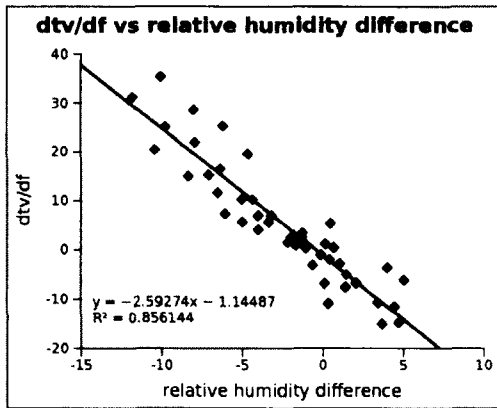


(c) $\frac{dT_v}{df_o}, \frac{dT_s}{df_o}$ correlation with air pressure differences.

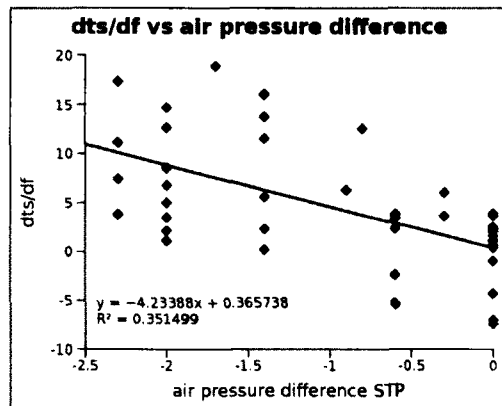
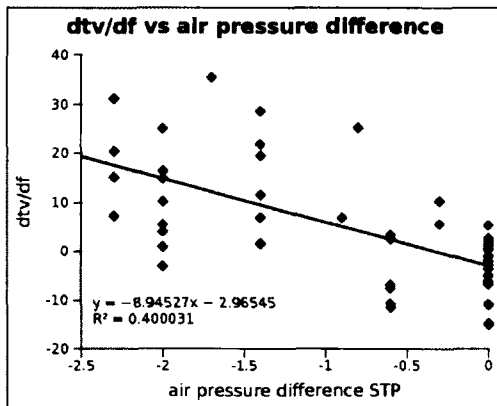
Figure 19: Environmental correlation graphs for 12/08/11 and 24cm bed.



(a) $\frac{dT_v}{df_o}, \frac{dT_s}{df_o}$ correlation with air temperature differences.

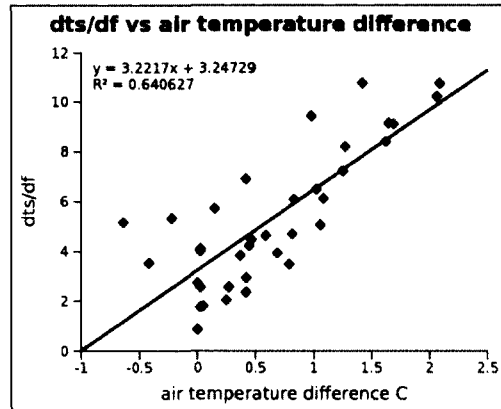
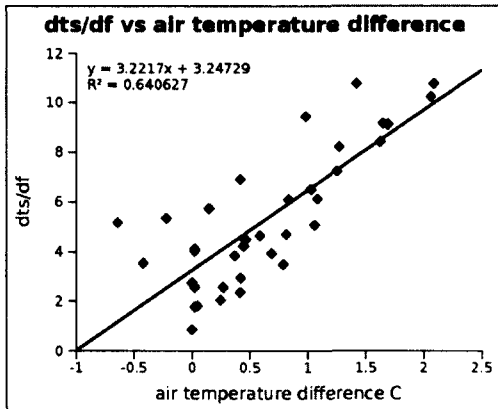


(b) $\frac{dT_v}{df_o}, \frac{dT_s}{df_o}$ correlation with relative humidity differences.

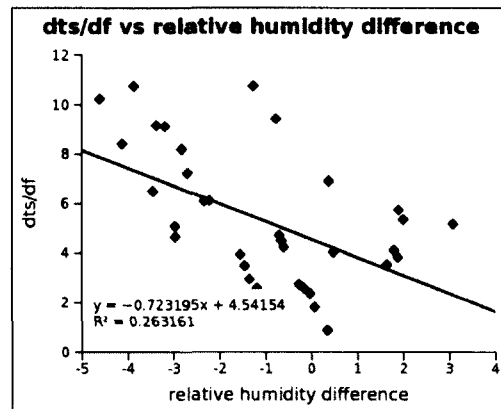
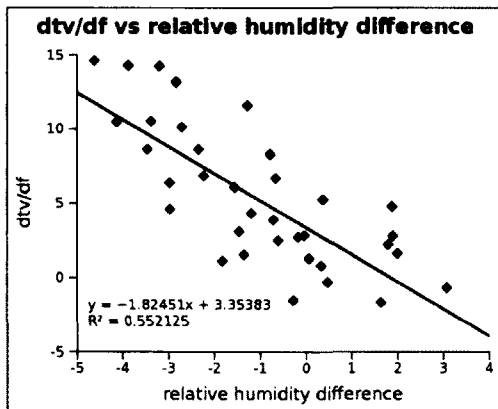


(c) $\frac{dT_v}{df_o}, \frac{dT_s}{df_o}$ correlation with air pressure differences.

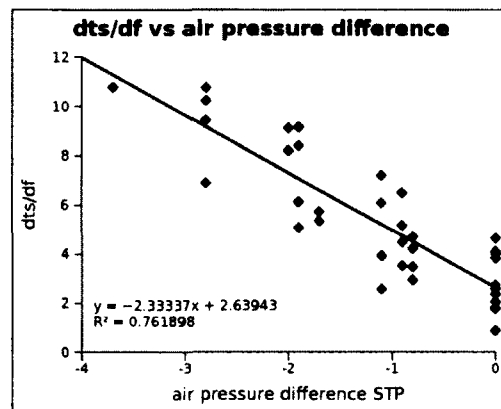
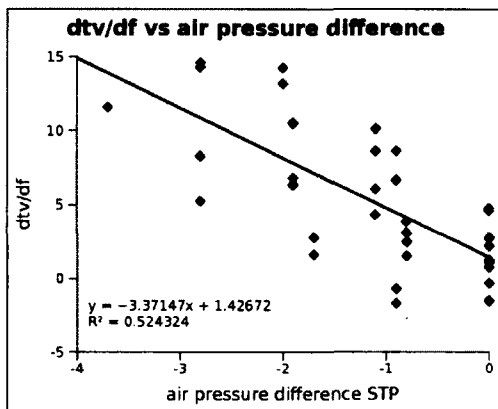
Figure 20: Environmental correlation graphs for 12/08/12 and 24cm bed.



(a) $\frac{dT_v}{df_o}, \frac{dT_s}{df_o}$ correlation with air temperature differences.

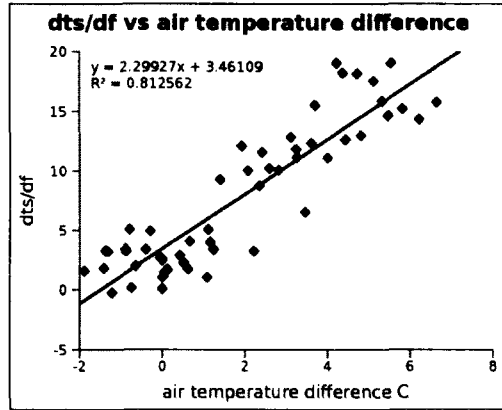
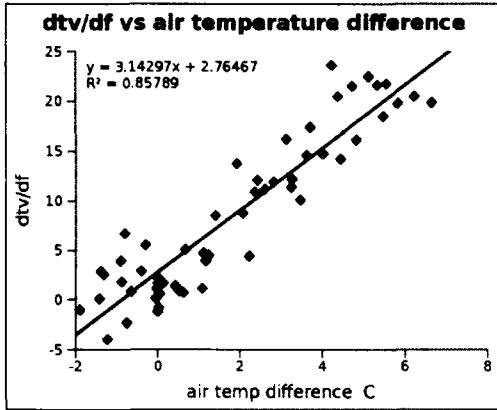


(b) $\frac{dT_v}{df_o}, \frac{dT_s}{df_o}$ correlation with relative humidity differences.

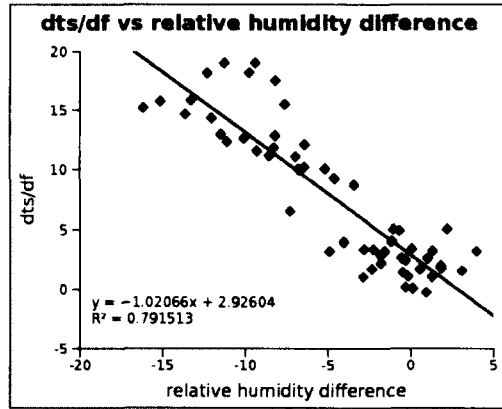
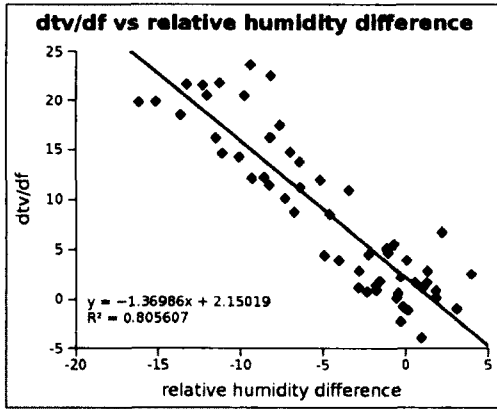


(c) $\frac{dT_v}{df_o}, \frac{dT_s}{df_o}$ correlation with air pressure differences.

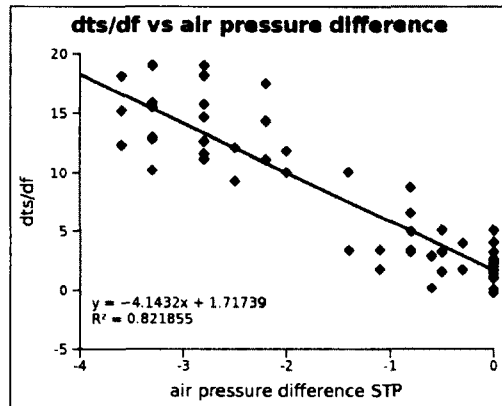
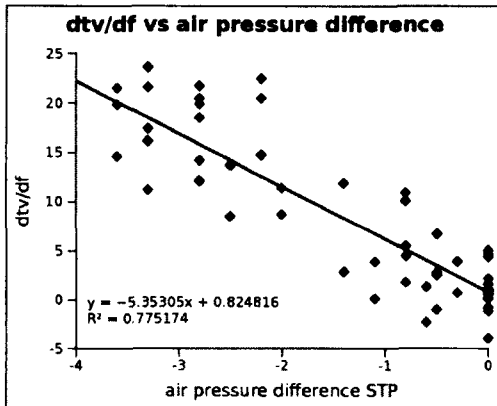
Figure 21: Environmental correlation graphs for 12/08/13 and 24cm bed.



(a) $\frac{dT_v}{df_\theta}, \frac{dT_s}{df_\theta}$ correlation with air temperature differences.

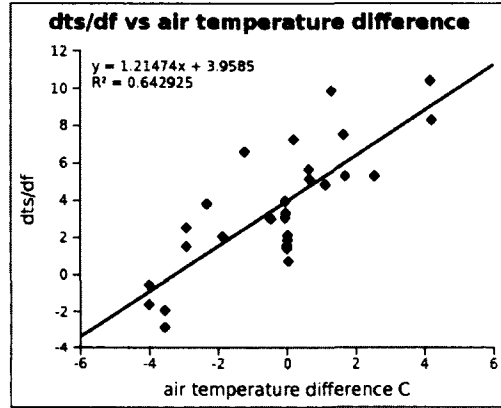
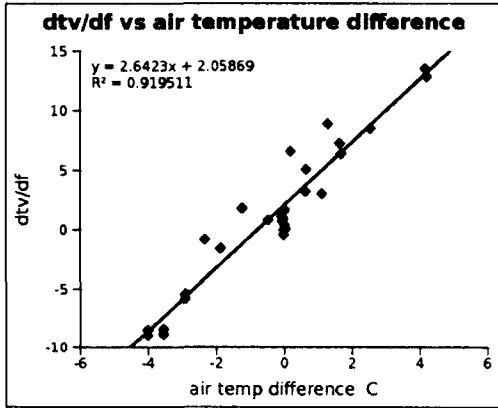


(b) $\frac{dT_v}{df_\theta}, \frac{dT_s}{df_\theta}$ correlation with relative humidity differences.

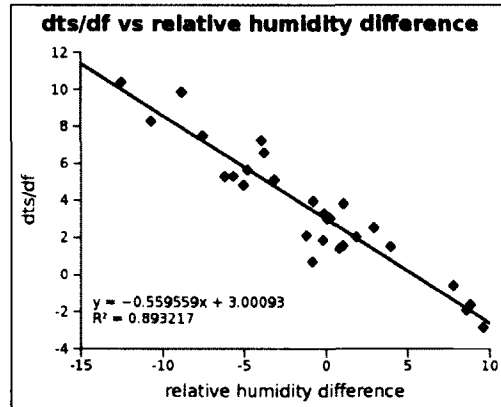
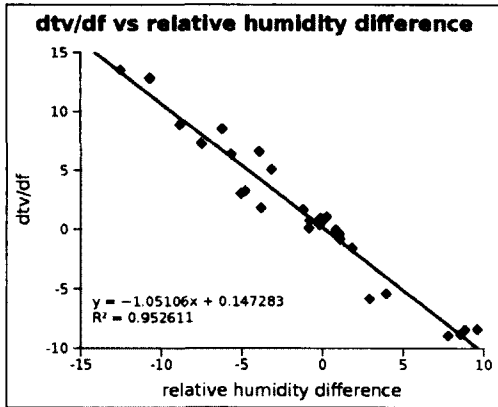


(c) $\frac{dT_v}{df_\theta}, \frac{dT_s}{df_\theta}$ correlation with air pressure differences.

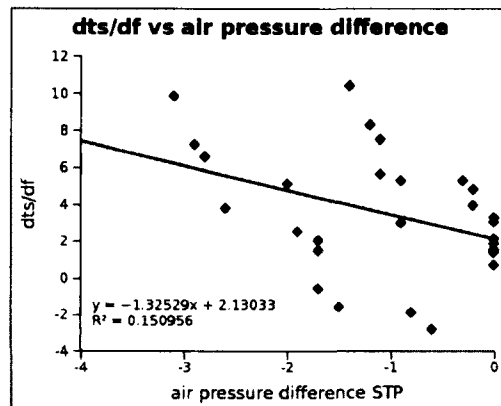
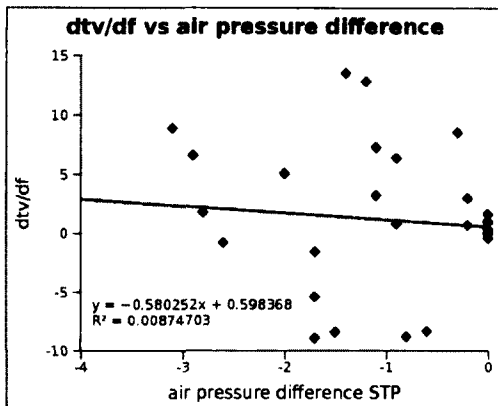
Figure 22: Environmental correlation graphs for 12/08/14 and 24cm bed.



(a) $\frac{dT_v}{df_\theta}, \frac{dT_s}{df_\theta}$ correlation with air temperature differences.

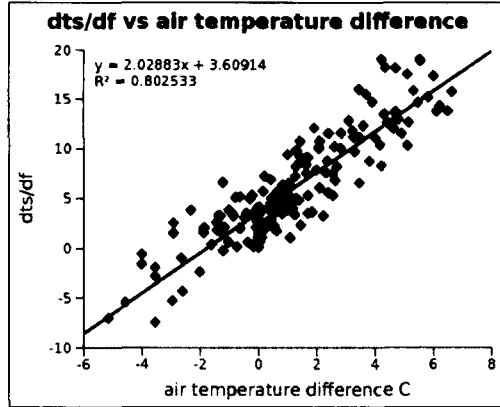
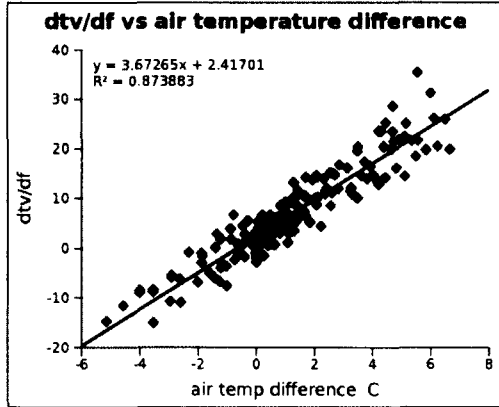


(b) $\frac{dT_v}{df_\theta}, \frac{dT_s}{df_\theta}$ correlation with relative humidity differences.

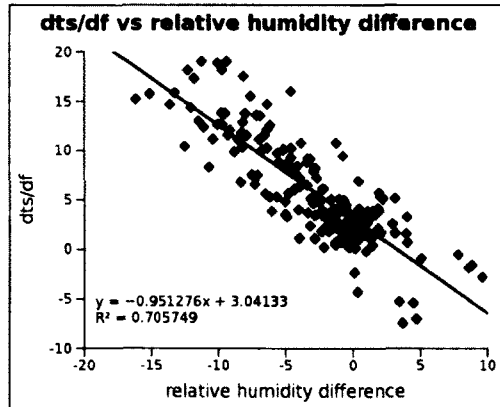
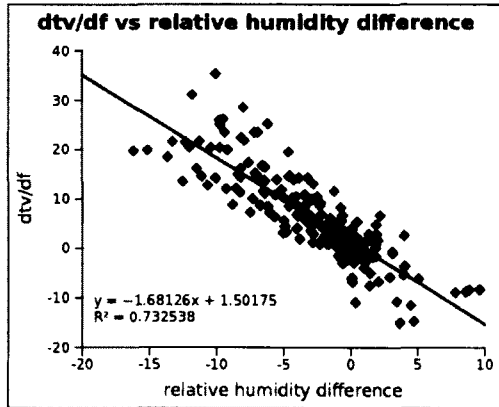


(c) $\frac{dT_v}{df_\theta}, \frac{dT_s}{df_\theta}$ correlation with air pressure differences.

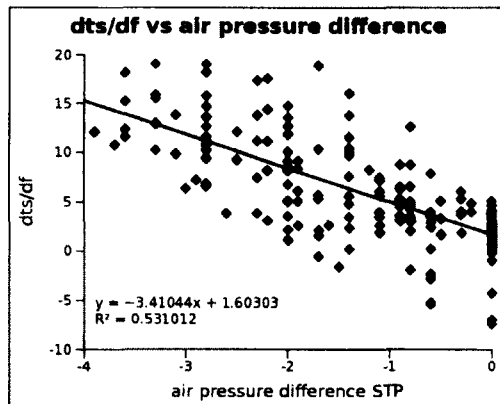
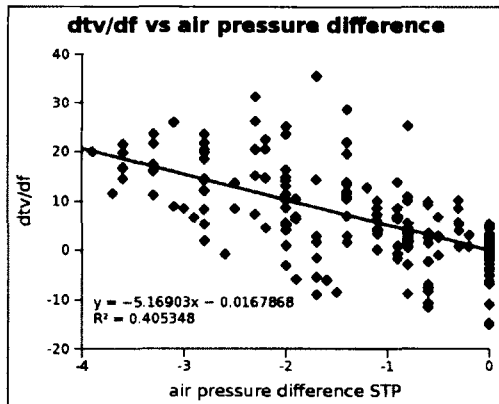
Figure 23: Environmental correlation graphs for 12/08/15 and 24cm bed.



(a) $\frac{dT_v}{df_\theta}, \frac{dT_s}{df_\theta}$ correlation with air temperature differences.



(b) $\frac{dT_v}{df_\theta}, \frac{dT_s}{df_\theta}$ correlation with relative humidity differences.



(c) $\frac{dT_v}{df_\theta}, \frac{dT_s}{df_\theta}$ correlation with air pressure differences.

Figure 24: Environmental correlation graphs for all sample days and 24cm bed.

J Correlation graphs for relative humidity and air temperature differences.

Correlation graphs of relative humidity and air temperatures for all sample days are given below.

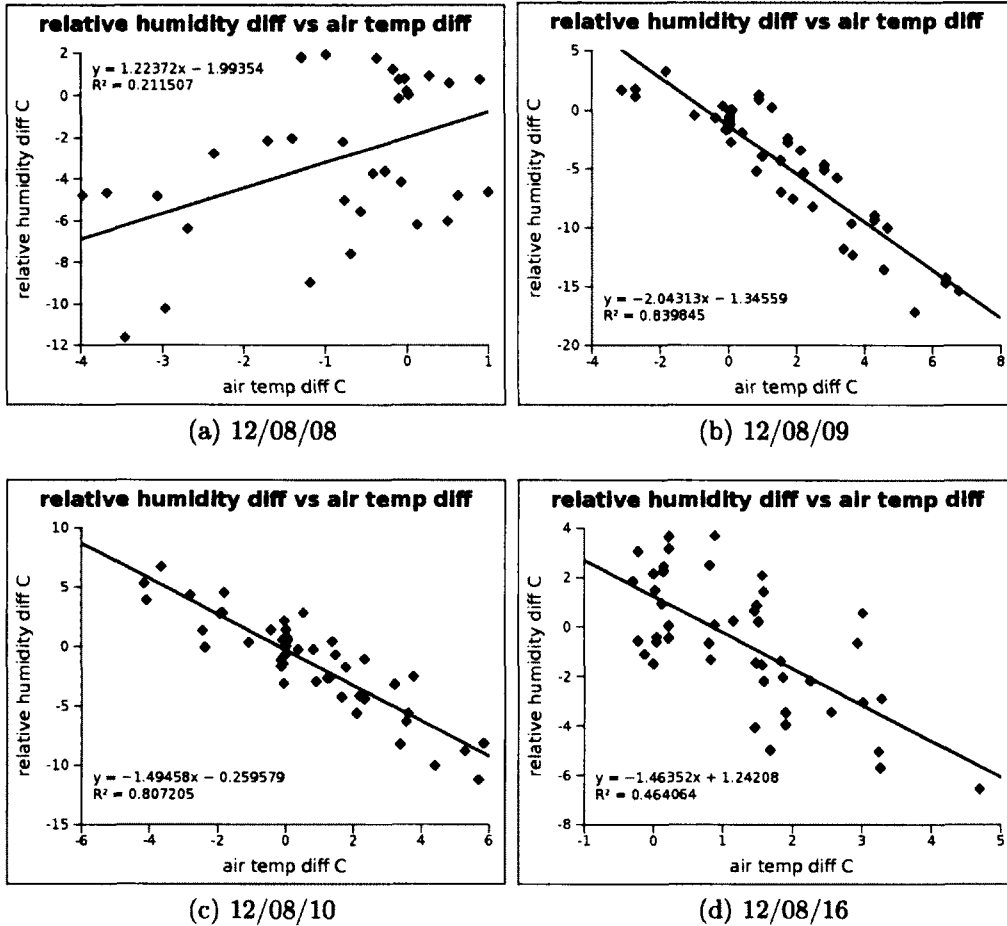
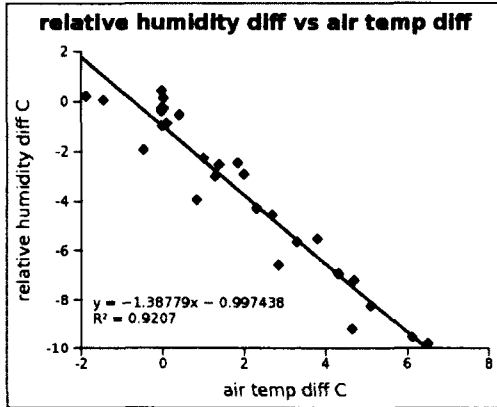
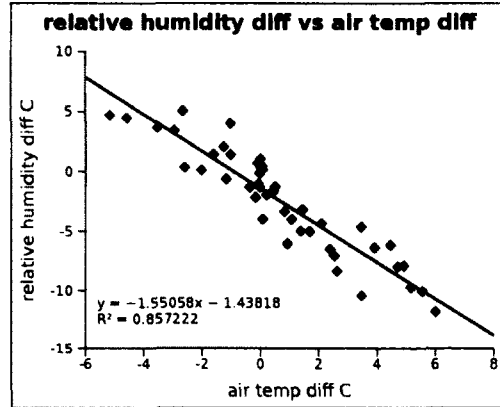


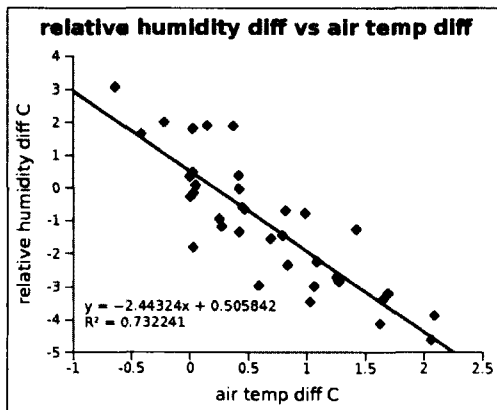
Figure 25: Relative humidity difference and air temperature difference correlation graphs for dates used 12cm bed.



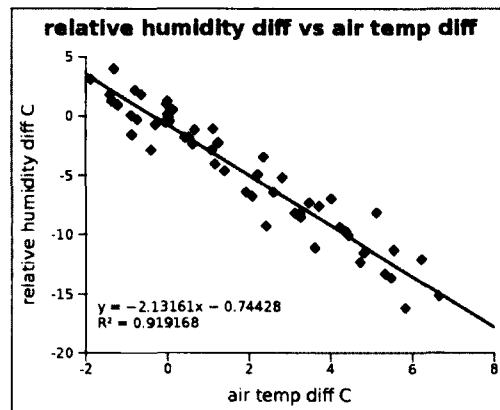
(a) 12/08/11



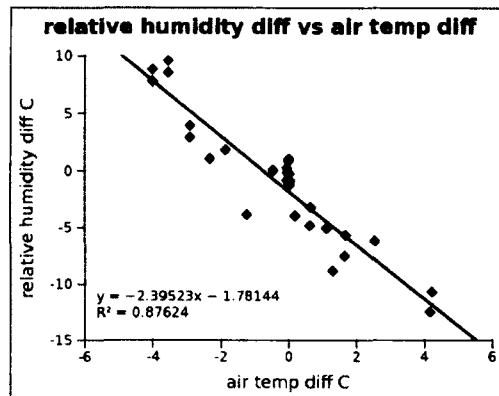
(b) 12/08/12



(c) 12/08/13



(d) 12/08/14



(e) 12/08/15

Figure 26: Relative humidity difference and air temperature difference correlation graphs for dates used for 24cm bed.

K Bi-variate correlation graphs of $\frac{dT_s}{df_\theta}$ for 12cm bed.

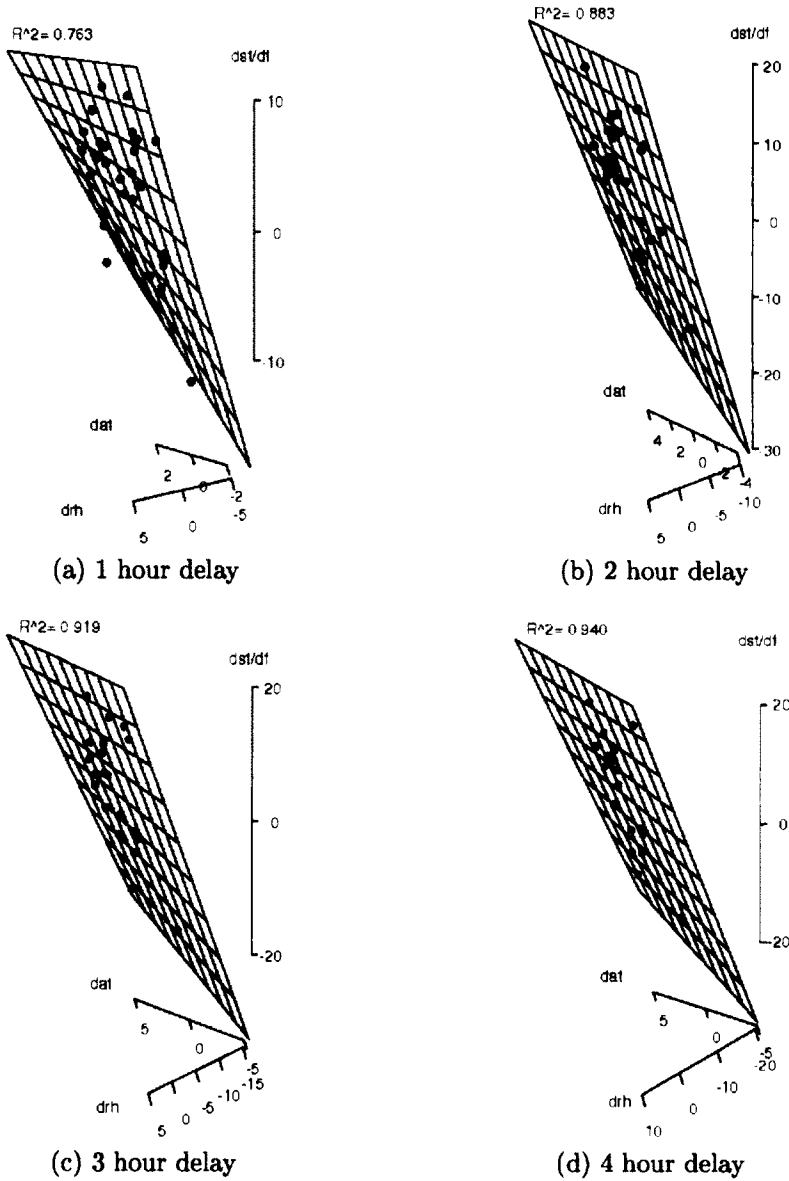
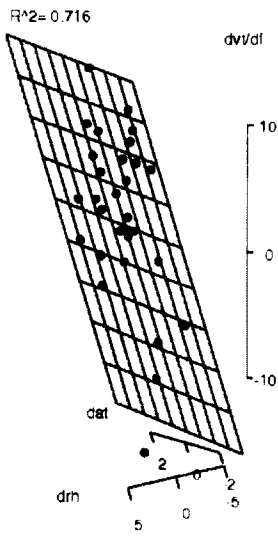
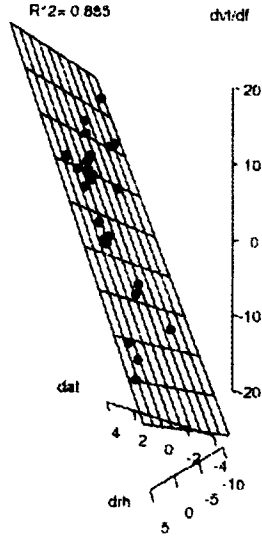


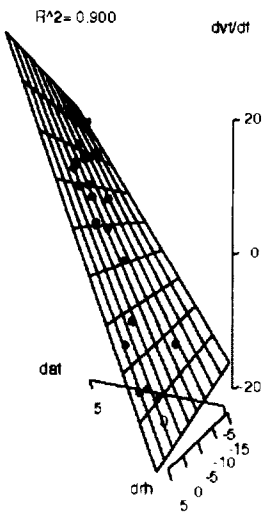
Figure 27: Delayed sampling correlations of $\frac{dT_s}{df_\theta}$.



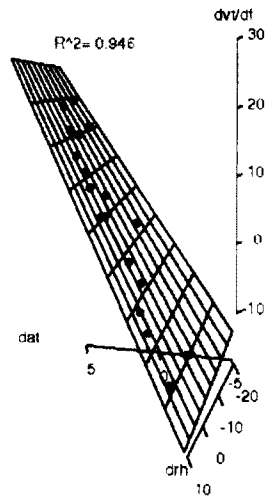
(a) 1 hour delay



(b) 2 hour delay



(c) 3 hour delay



(d) 4 hour delay

Figure 28: Delayed sampling correlations of $\frac{dT_v}{df_\theta}$.

L Principal component analysis graphs for 12cm bed.

Principal component scree and biplot graphs are given below which show the contributions of the correlated variables to an orthogonal basis. Variable vectors are scaled because units are not the same.

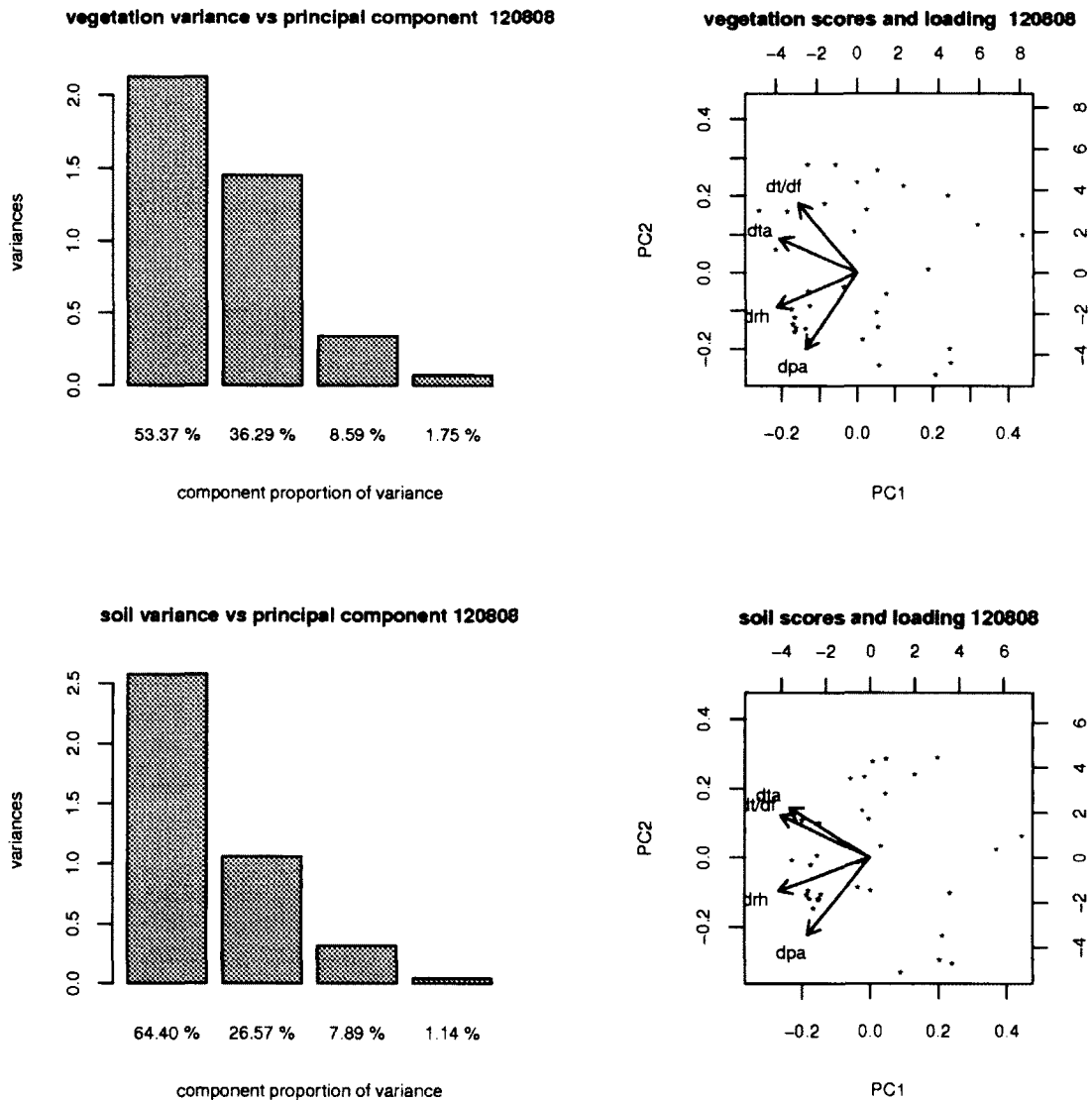


Figure 29: $\frac{dT_s}{df_\theta}$, $\frac{dT_s}{df_\theta}$ principal component graphs for 12/08/08 and 12cm bed.

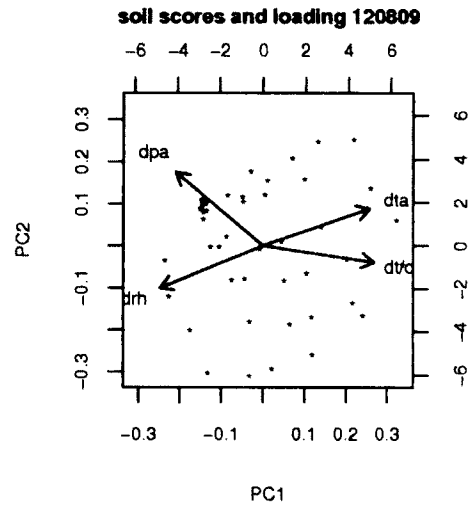
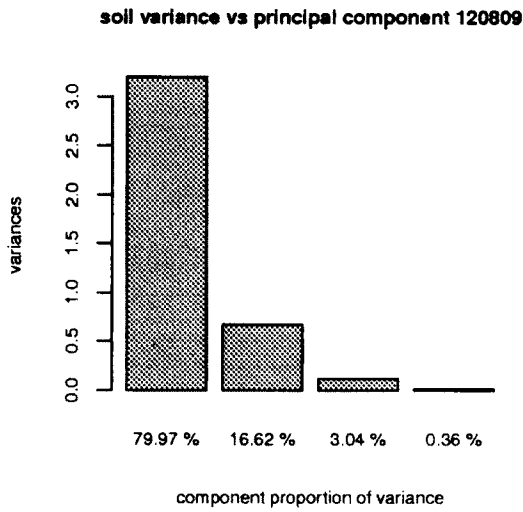
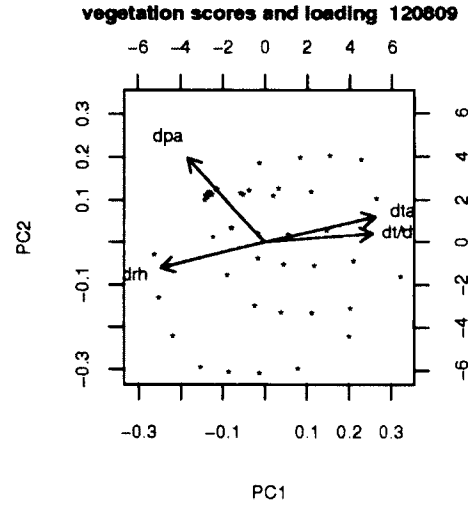
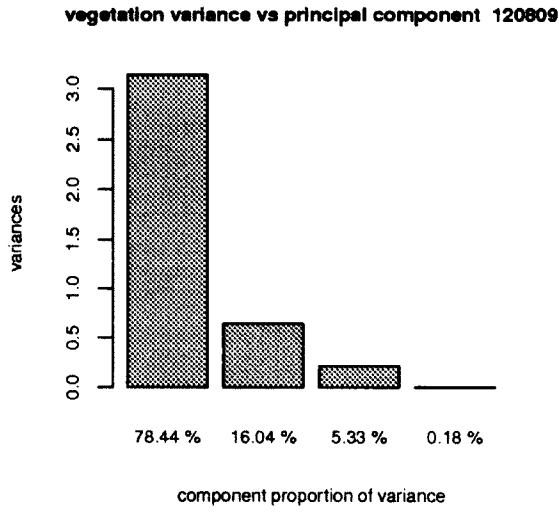


Figure 30: $\frac{dT_u}{df_\theta}$, $\frac{dT_s}{df_\theta}$ principal component graphs for 12/08/09 and 12cm bed.

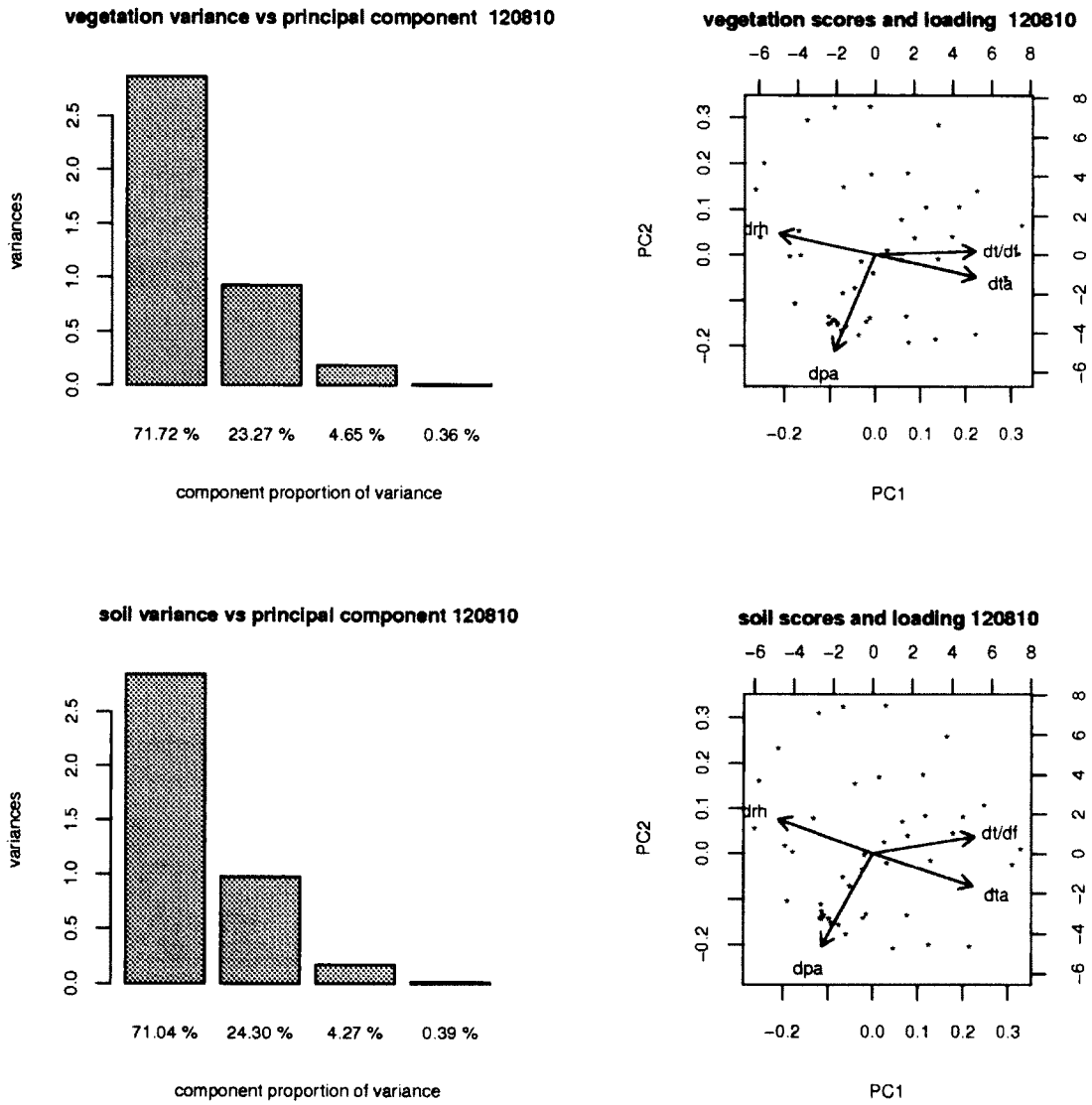


Figure 31: $\frac{dT_v}{df_\theta}$, $\frac{dT_s}{df_\theta}$ principal component graphs for 12/08/10 and 12cm bed.

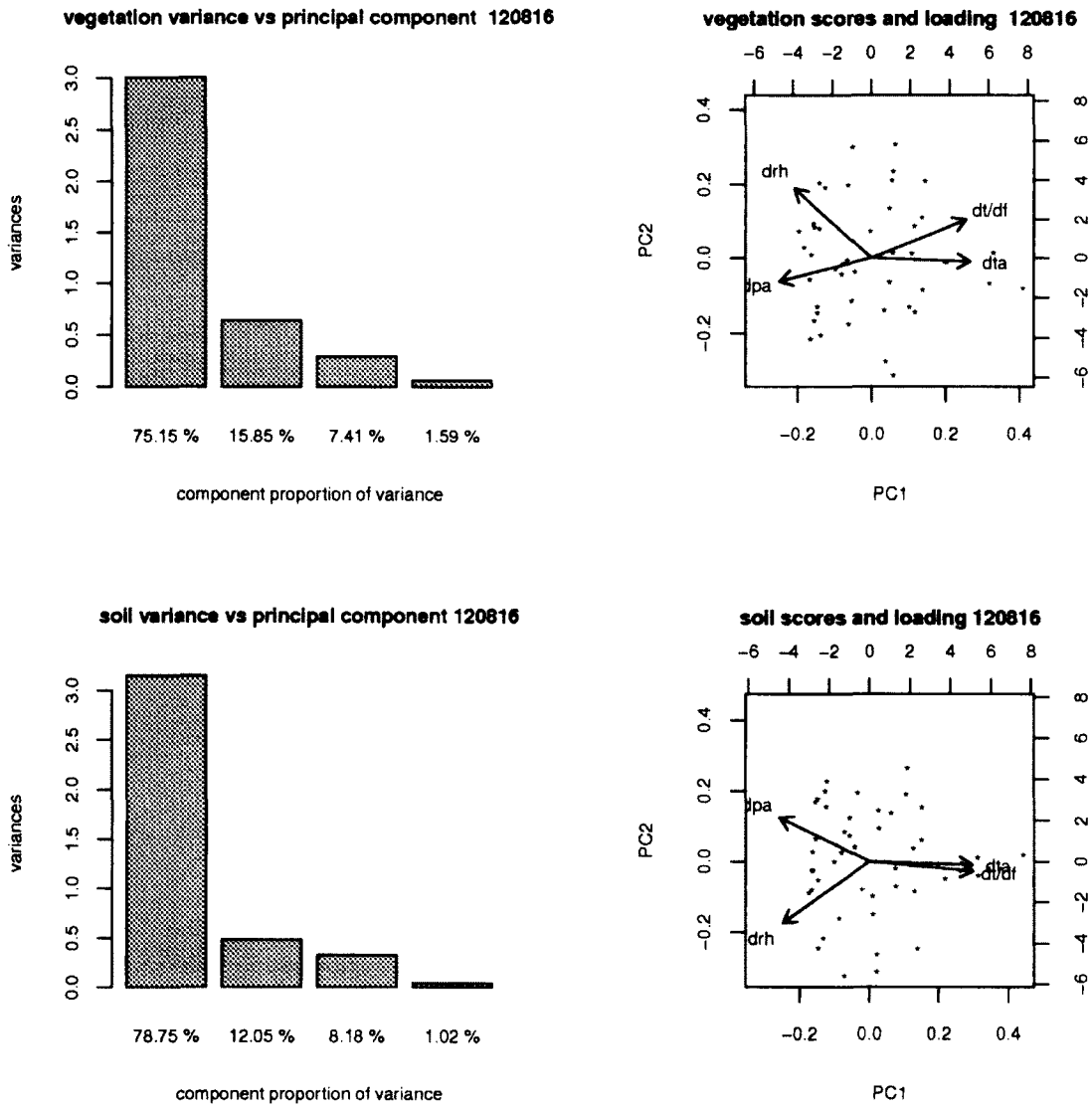


Figure 32: $\frac{dT_v}{df_\theta}$, $\frac{dT_s}{df_\theta}$ principal component graphs for 12/08/16 and 12cm bed.

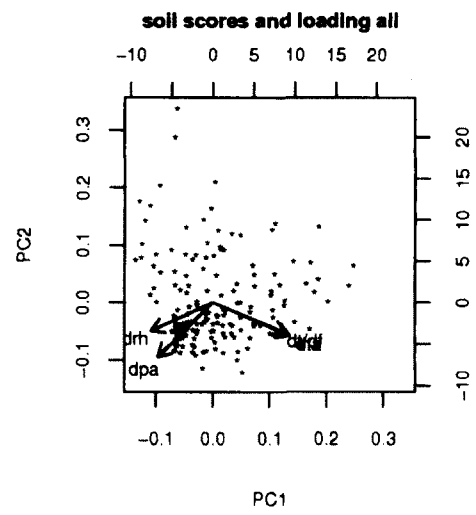
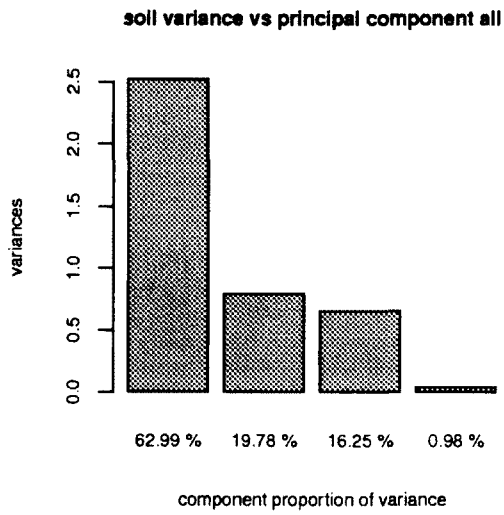
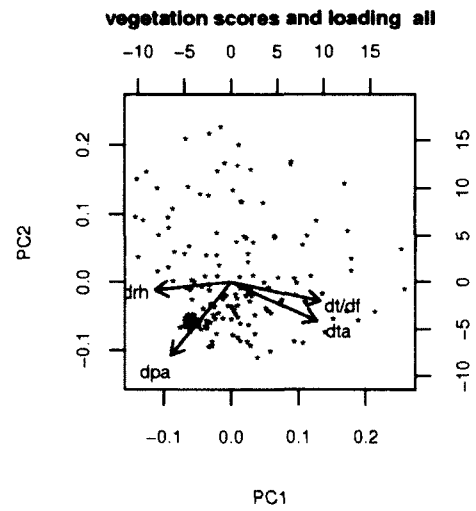
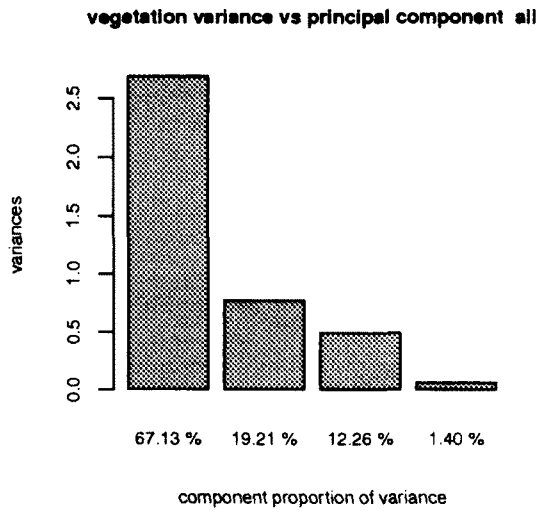


Figure 33: $\frac{dT_v}{df_\theta}$, $\frac{dT_s}{df_\theta}$ principal component graphs for all and 12 cm bed.

M Principal component analysis graphs for 24cm bed.

Principal component scree and biplot graphs are given below which show the contributions of the correlated variables to an orthogonal basis. Variable vectors are scaled because units are not the same.

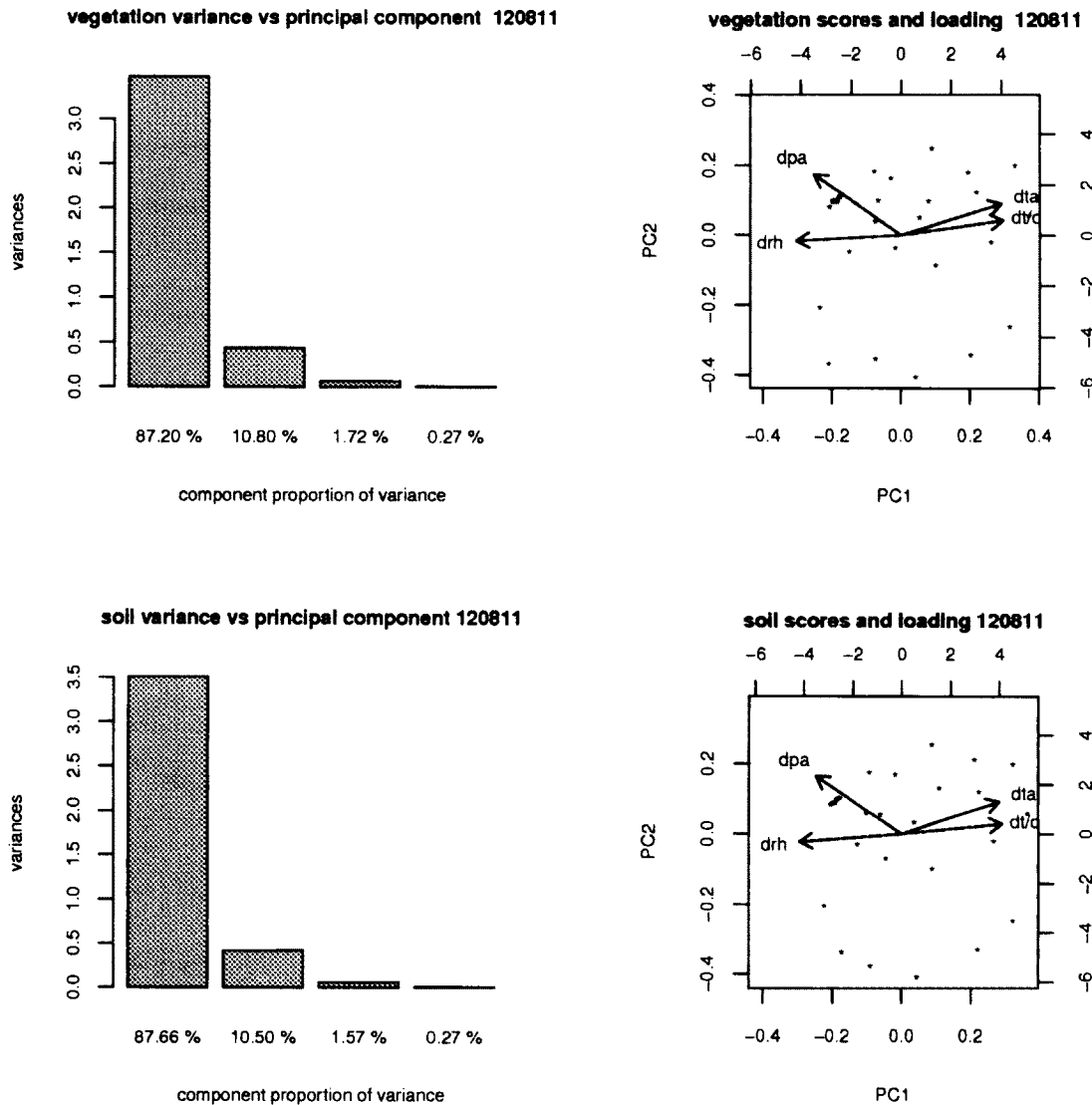


Figure 34: $\frac{dT_v}{df_\theta}$, $\frac{dT_s}{df_\theta}$ principal component graphs for 12/08/11 and 24cm bed.

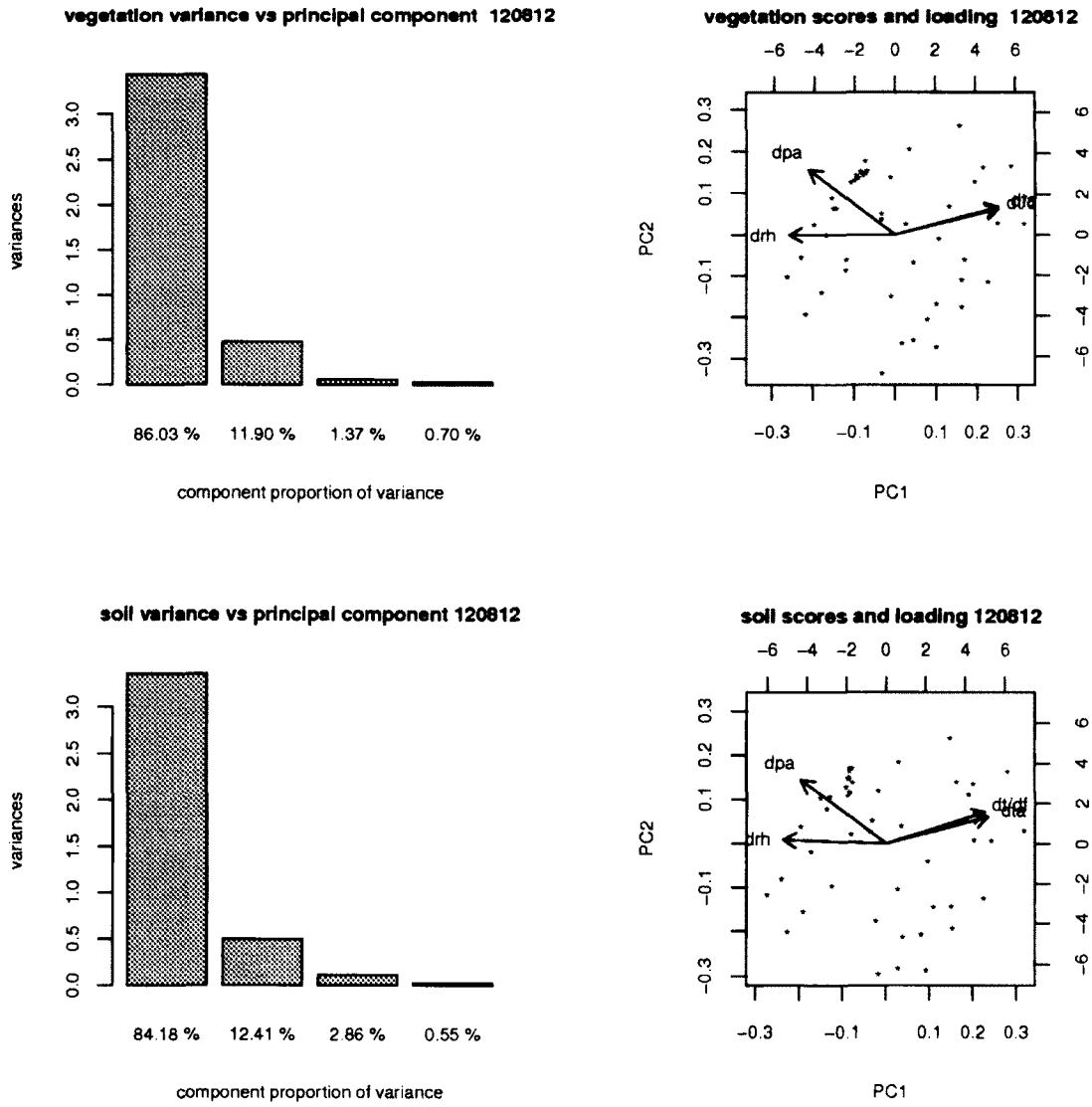


Figure 35: $\frac{dT_v}{df_\theta}$, $\frac{dT_s}{df_\theta}$ principal component graphs for 12/08/12 and 24cm bed.

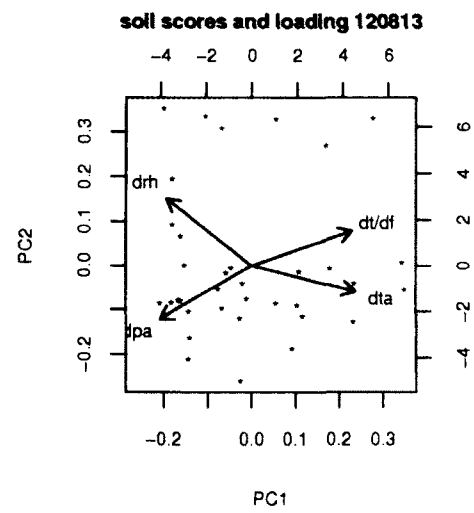
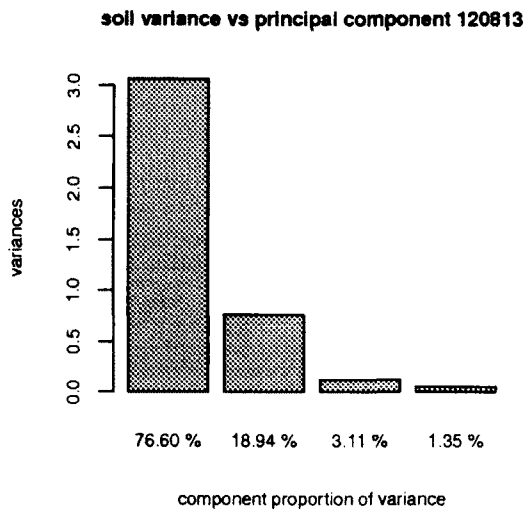
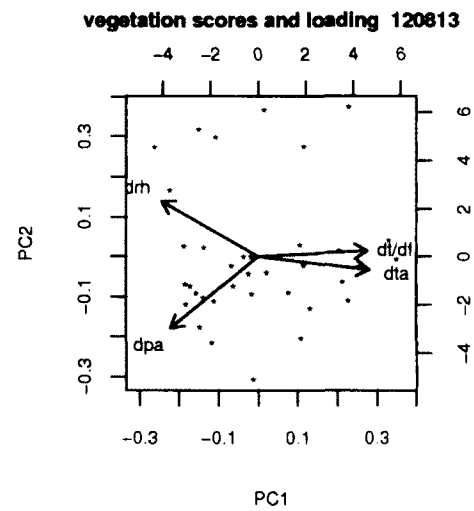
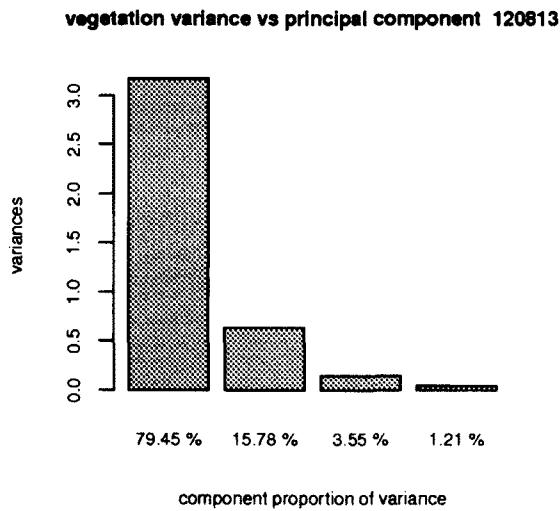


Figure 36: $\frac{dT_v}{df_0}$, $\frac{dT_s}{df_0}$ principal component graphs for 12/08/13 and 24cm bed.

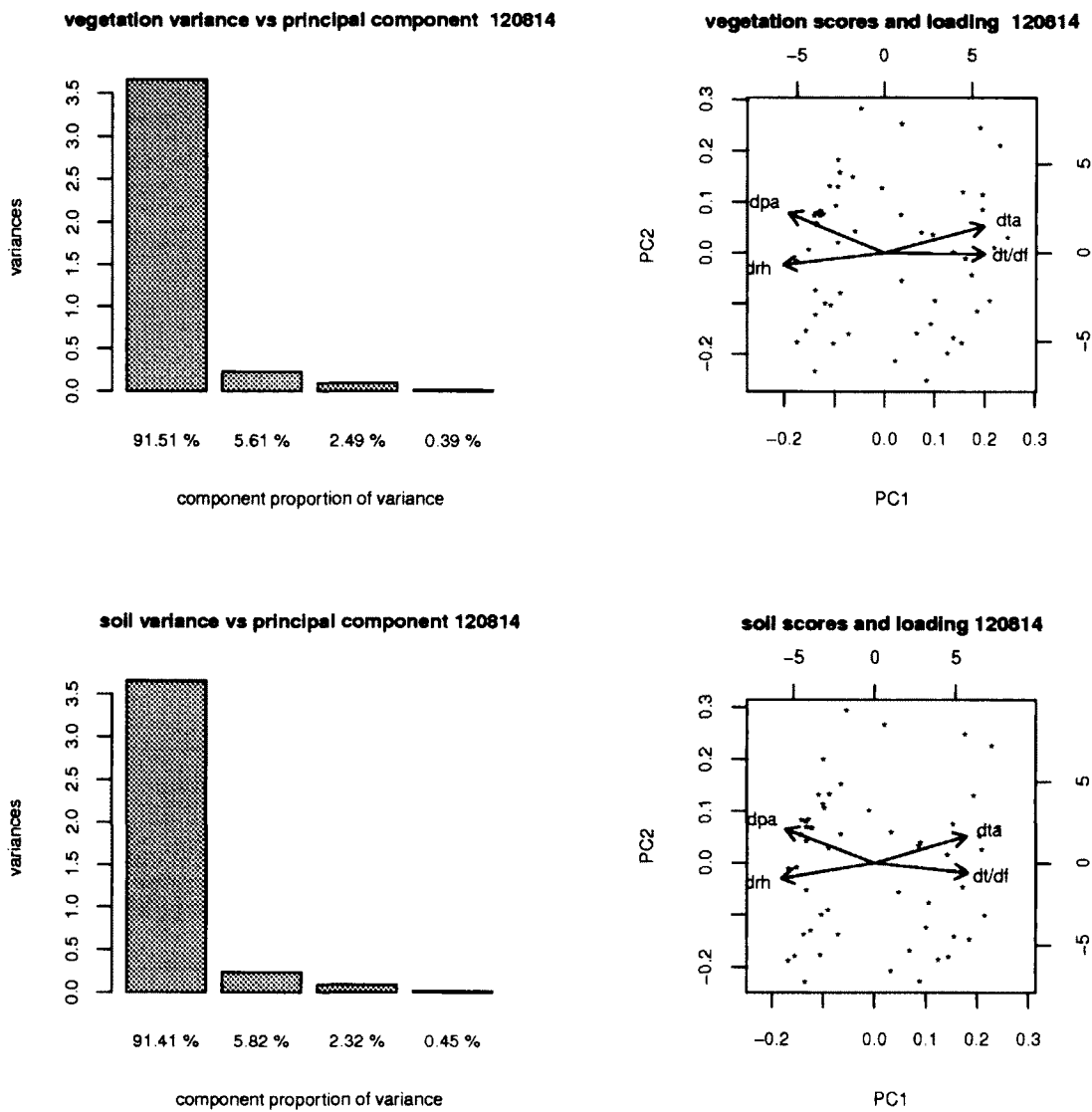


Figure 37: $\frac{dT_v}{df_\theta}$, $\frac{dT_s}{df_\theta}$ principal component graphs for 12/08/14 and 24cm bed.

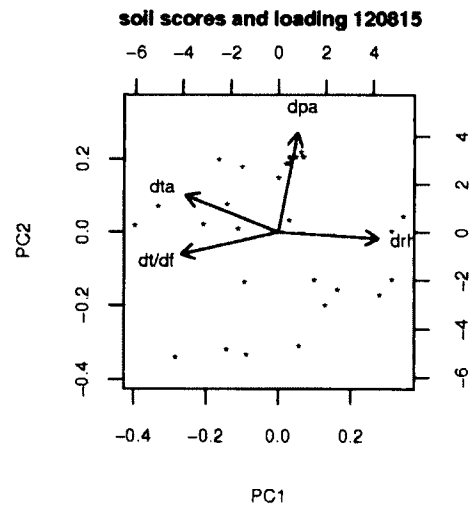
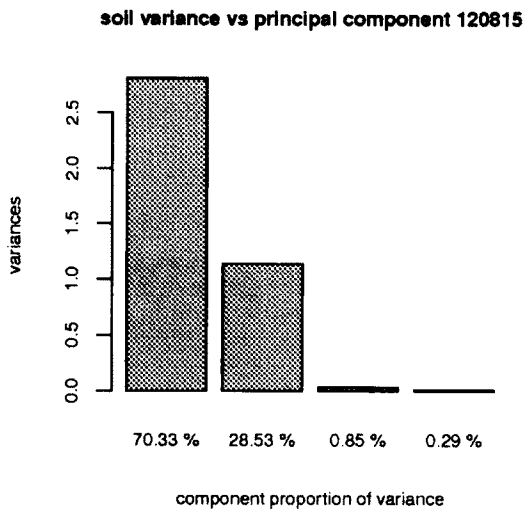
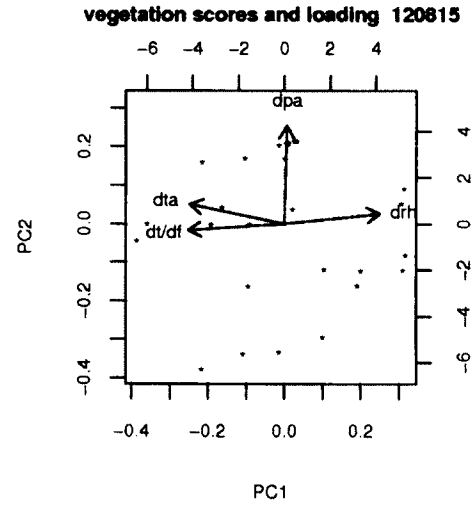
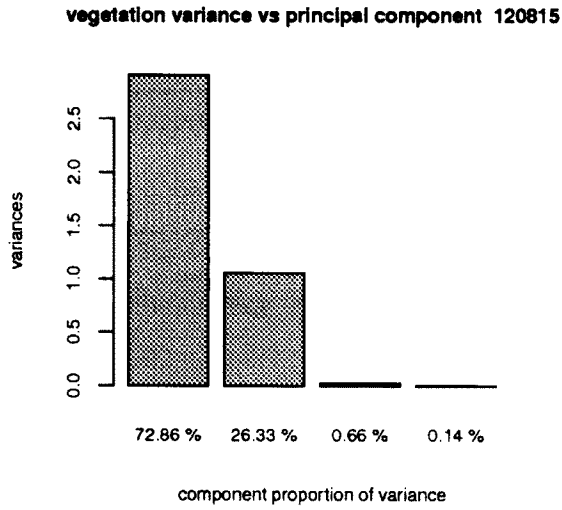


Figure 38: $\frac{dT_v}{df_\theta}$, $\frac{dT_s}{df_\theta}$ principal component graphs for 12/08/15 and 24cm bed.

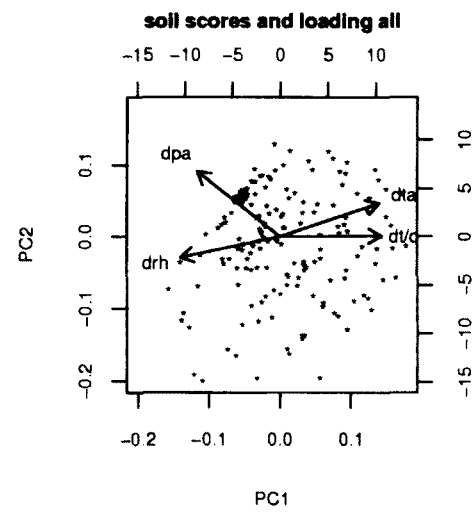
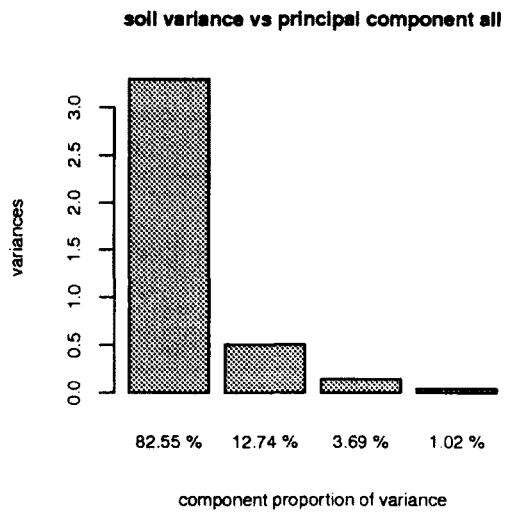
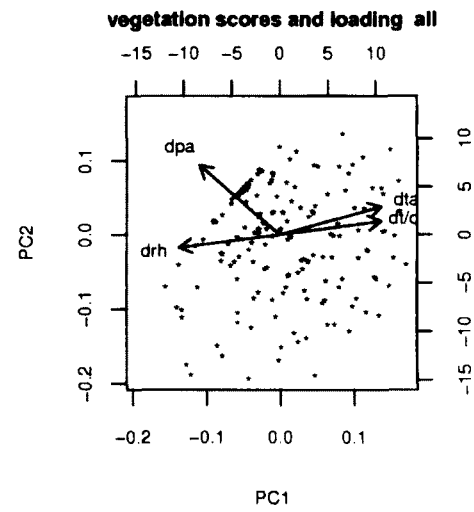
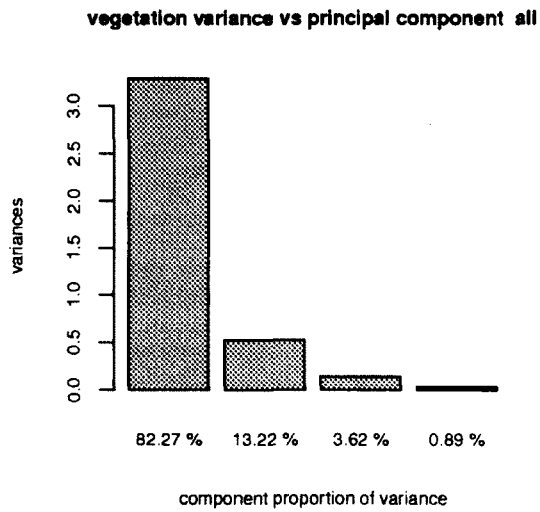


Figure 39: $\frac{dT_v}{df_\theta}$, $\frac{dT_s}{df_\theta}$ principal component graphs for all and 24cm bed.

N Differential coefficients observed over time periods.

This table shows the differential coefficients at different time delay sampling.

Near Instantaneous			1 Hour Delay			2 Hour Delay			3 Hour Delay			4 Hour Delay		
time	ds/df_{θ}	dv/df_{θ}	time	ds/df_{θ}	dv/df_{θ}	time	ds/df_{θ}	dv/df_{θ}	time	ds/df_{θ}	dv/df_{θ}	time	ds/df_{θ}	dv/df_{θ}
14:03	-0.284	-1.126	14:03	-2.544	-1.544	14:03	-2.788	-6.084	15:05	-2.426	1.224	16:03	0.873	3.116
15:05	1.405	-0.898	15:05	0.259	6.071	15:05	-2.162	6.133	16:03	1.265	10.859	17:04	3.124	10.076
16:03	2.111	-0.368	16:03	6.436	-0.306	16:03	4.599	10.282	17:04	5.305	9.731	18:02	-0.141	2.043
17:04	2.401	0.155	17:04	3.599	2.380	17:04	6.581	2.423	18:02	1.081	-5.482	19:01	-10.384	-9.069
18:02	0.146	-1.741	18:02	-3.145	-7.758	18:02	-1.946	-5.523	19:01	-13.289	-9.107			
19:01	-0.701	-3.952	19:01	-11.377	-5.505	19:01	-14.406	-11.244						
10:02	0.625	-0.554	11:02	5.572	9.258	12:04	8.719	14.641	13:01	9.048	17.172	14:02	12.266	20.784
11:02	1.154	1.167	12:04	4.642	7.173	13:01	4.770	9.352	14:02	8.410	13.716	15:02	11.784	19.677
12:04	2.189	3.822	13:01	2.194	5.756	14:02	5.935	10.286	15:02	9.187	16.031	16:03	11.938	22.558
13:01	1.742	0.044	14:02	5.517	5.078	15:02	8.764	10.811	16:03	11.494	17.106	17:04	12.257	14.207
14:02	0.511	3.594	15:02	4.051	9.852	16:03	6.823	16.707	17:03	7.541	13.512	18:00	2.627	-2.587
15:02	1.392	-1.132	16:03	3.946	4.988	17:03	4.567	1.617	18:00	-0.245	-14.207			
16:03	1.793	4.536	17:03	2.356	1.178	18:00	-2.480	-14.538						
17:03	2.889	1.488	18:00	-2.049	-14.600									
18:00	3.060	1.781												
10:03	0.489	-2.852	11:03	5.047	7.597	12:03	9.266	11.279	13:02	11.774	15.376	14:02	14.412	23.704
11:03	1.687	-0.319	12:03	5.985	3.339	13:02	8.394	7.116	14:02	11.219	15.975	15:02	15.165	19.637
12:03	1.398	-1.602	13:02	3.436	1.727	14:02	6.26	10.346	15:02	10.000	13.808	16:04	8.999	10.318
13:02	2.373	-1.668	14:02	5.300	7.269	15:02	9.135	10.8	16:04	8.378	8.155	17:03	5.303	-0.461
14:02	2.563	0.905	15:02	6.351	4.359	16:04	6.438	3.671	17:03	2.548	-6.823	18:04	1.104	-8.298
15:02	1.655	0.915	16:04	3.154	1.266	17:03	-2.115	-10.187	18:04	-3.230	-11.423			
16:04	2.094	1.704	17:03	-3.473	-9.256	18:04	-4.469	-10.522						
17:03	0.376	0.794	18:04	-0.915	-1.200									
18:04	1.424	1.560												
09:30	2.055	0.490	10:29	10.575	9.052	11:30	18.476	11.858	12:29	18.437	15.741	13:03	22.751	23.664
10:29	1.618	-0.038	11:30	7.065	0.457	12:29	9.362	6.567	15:01	8.407	14.375	14:30	12.489	15.326
11:30	-0.438	-2.782	12:29	3.339	3.893	14:00	5.919	11.377	15:47	7.287	7.751	15:01	7.076	11.845
12:01	2.930	0.918	13:03	8.300	13.597	14:30	5.627	9.349				15:47	13.007	16.279
12:29	2.200	0.202	14:00	-1.946	-0.764	15:01	0.371	1.943						
13:03	0.390	1.343	15:01	5.186	3.284	15:47	11.312	8.771						
14:00	2.794	0.615	15:47	8.757	5.753									
14:30	2.209	-0.122												
15:01	2.062	-0.352												
15:47	3.290	0.688												
avg	1.577	0.212	avg	2.952	6.113	avg	4.267	4.509	avg	5.610	7.175	avg	8.036	10.712
max	3.290	4.536	max	10.575	13.597	max	18.476	16.707	max	18.437	17.172	max	22.751	23.704
min	-0.701	-3.952	min	-11.377	-14.6	min	-14.406	-14.538	min	-13.289	-14.207	min	-10.384	-9.069

Table 43: Calculated differential coefficients from sensed covers over time.